CHARMED AND STRANGE BARYON PRODUCTION IN 29 GEV ELECTRON POSITRON ANNIHILATION*

SPENCER ROBERT KLEIN

Stanford Linear Accelerator Center
Stanford University, Stanford, California 94309

June 1988

*Ph.D. Dissertation

MASTER

Philosophers call this object *matter*, adding that our intelligence grasps its meaning only imperfectly, since imperfection is its nature, that it does not really exist and therefore cannot claim any predicate, and although it exists only virtually, its predicate is corporeal. Aristotle says that it is, so to speak, ashamed to appear naked, and therefore only shows itself in a clothed form.

- Judah Halevi, in *The Kuzari*

Wine, dear boy, and Truth.

- Alcaeus, *Fragment 66*

Abstract

Baryon production is one of the least understood areas of hadron production in electron positron collisions. Early models of hadronization predicted that very few baryons should be produced. However, experiments have shown a very substantial rate of baryon production, and many different models have been proposed to explain this. One way to test these models, and to further probe the hadronization process is to measure the production rates of different types of baryons. This dissertation presents measurements of the production rates of baryons with different strangeness and spin. The analyses presented here use data taken with the Mark II detector at the PEP storage ring, operating at a center of mass energy of 29 GeV. The Ξ^- production rate is measured to be 0.017 $\pm$ 0.004 $\pm$ 0.004 per hadronic event, Ω^- production is measured to be 0.014 $\pm$ 0.006 $\pm$ 0.004 per hadronic event, and Ξ^{*0} production is less than 0.006 per hadronic event at a 90% confidence level. These measurements place strong constraints on models of baryon production. In particular, the unexpectedly high rate of Ω^- production is difficult to explain in any diquark based model. Semileptonic Λ_c^+ decays have also been observed, with $\sigma(e^+e^- \to \Lambda_c X) * Br(\Lambda_c \to e\Lambda X) = 0.0031 \pm 0.0012 \pm 0.0010$ per hadronic event, and $\sigma(e^+e^- \to \Lambda_c X) * Br(\Lambda_c \to \mu\Lambda X) = 0.0024 \pm 0.0024 \pm 0.0007$ per hadronic event. Because neither the branching ratios nor the production rate are well known, it is difficult to interpret these results. However, they do indicate that the branching ratio for $\Lambda_c^+ \to \Lambda l\nu$ may be higher than previous experimental measurements.

iii

Acknowledgments

Any large high energy physics experiment is built on the work of many people: physicists, technicians, engineers, and secretaries. Without them, this analysis would not be possible. To all those who worked on the Mark II, past and present: Thank you. Several people deserve special thanks. My fellow 'tail end of PEP5' graduate students contributed much to making life at SLAC survivable, and the new crop of SLC students and postdocs helped remind me that life does not end at 29 GeV. In particular, I would like to thank Rene Ong and Steve Wagner for convincing me to look for semileptonic Λ_c^+ decays, Bruce LeClaire for his wonderful TeX macros and general officemateship, Alfred Petersen and Paul Dauncey for their explanations of the intricacies of the Lund and Webber Monte Carlos, and Keith Riles and Dean Karlen for frequent consultations at all hours, and all of the above for innumerable stimulating conversations. George Trilling provided many helpful comments on an early draft of this manuscript, and has generally been very helpful. Jonathan Dorfan did a tremendous job of providing the things that a physicist needs to keep working, both in terms of material and moral support. I am also extremely indebted to Martin Perl for teaching me a lot about fundamental experimental physics in general. Last, but definitely not least, I would like to thank my advisor, Tom Himel for teaching me to be a physicist.

Of course, man cannot live by physics alone. John Rick and Curtis Runnels deserve thanks for nurturing my interest in archaeology. I would like to thank everyone at Hammarskjöld House for everything: curried eggs, Boom-La-La, late night discussions on feminism in India, Yosemite trips, and moral support. My friends have done much to make my stay here more pleasant. You know who you are.

Finally, I would like to thank my parents, for absolutely everything.

iv

Table of Contents

List of Tables

List of Figures

Chapter 1. Introduction

Over the past 25 years, high energy physics has undergone a revolution. We have gone from a simple model of atoms composed of protons, neutrons, and electrons, to a more complicated (and hopefully more accurate) description of matter composed of quarks and leptons, interacting under a set of four basic forces. This picture of nature is known as "the standard model."[1]

The standard model is currently accepted by physicists as the basic theory of nature, to which other theories are compared, either as additions, or replacements. The standard model does not answer every question we could ask, but it does provide a reasonably coherent structure from which to begin. In it, matter is composed of quarks and leptons, divided into generations. So far, three almost complete generations are known,[2] although there is no known reason why there should be three generations in the standard model. There could be further generations waiting to be discovered. Each generation is composed of two quarks, a charged lepton, and a neutrino. These generations are displayed in Table 1.1, arranged in order of increasing mass. Table 1.2 shows some of the properties of these particles. The standard model provides no clues as to particle masses, and the lifetimes depend largely on apparently arbitrary couplings. In general, these properties are measured, rather than calculated.

	Quarks	Charged Lepton	Neutrino
1st	d, u	e^-	ν_e
2nd	s, c	μ^-	ν_μ
3rd	b, t	τ^-	ν_τ

Table 1.1. The three generations. Each comprises two quarks, a charged lepton, and a neutral neutrino. Each particle has a corresponding antiparticle.

Particle	Mass	Charge	Spin	Lifetime	Type
Electron	511 KeV/c^2	−1	1/2	Stable	Lepton
ν_e	<46 eV/c^2	0	1/2	Stable	Neutrino
Down	∼ 8 MeV/c^2	−1/3	1/2	Long	Quark
Up	∼ 4 MeV/c^2	+2/3	1/2	Stable	Quark
Muon	105 MeV/c^2	−1	1/2	2.2×10^{-6} s	Lepton
ν_μ	<250 KeV/c^2	0	1/2	Stable	Neutrino
Strange	150 MeV/c^2	−1/3	1/2	10^{-10} s	Quark
Charm	1.5 GeV/c^2	+2/3	1/2	4×10^{-13} s	Quark
Tau	1.784 GeV/c^2	−1	1/2	2.8×10^{-13} s	Lepton
ν_τ	<35 MeV/c^2	0	1/2	Stable	Neutrino
Bottom	5.2 GeV/c^2	−1/3	1/2	10^{-12} s	Quark
Top	>40 GeV/c^2	+2/3	1/2	?	Quark

Table 1.2. Properties of known particles. All of these particles have antiparticles with the opposite quantum numbers. Since quarks have not been observed as free particles, it is impossible to measure their masses directly. Instead, their masses are calculated from the measured meson masses[3] The masses of heavier quarks can be estimated fairly accurately, since they make up a much larger percentage of their mesons mass. The lifetimes are also very rough because quark lifetime depends on the environment; for example, down quarks in neutrons decay to up quarks. but they are stable in protons.

Not all of these particles directly correspond to those observed in nature. While all the leptons except the ν_τ have been observed[4] free quarks have never been seen directly[5] This is in keeping with most streams of the standard model; only a few variations of the standard model allow for the possibility of free quarks. Instead, we observe quark combinations, known as mesons and baryons. Mesons are bound states consisting of a quark and an antiquark, while baryons are bound states composed of three quarks. The 'fundamental' protons and neutrons of the 1950's are now thought to be composed of three quarks: two up quarks and

one down quark for the proton and one up quark and two down quarks for the neutron. By studying these quark combinations, we can get information about the underlying quarks, and the forces between them.

Besides the basic particles, the standard model describes the forces with which these particles interact: the weak force, the strong force, and electromagnetism. Gravity is part of the standard model, although it is not integrated with the other three. These forces are believed to be mediated by particles known as bosons, which carry the forces. The strength of these forces depends on the relative couplings of the bosons to the interacting quarks and leptons. The range of the forces is dependent on the mass of the bosons, as related by the Yukawa potential formula:

$$V(r) = \frac{1}{r} e^{-mcr/\hbar} \ .$$

The different bosons are listed in Table 1.3. There are eight gluons, each carrying a different combination of the three colors. The color combinations are given by SU(3) group theory.

Particle	Mass	Spin	Force	Force Range
Photon	0.	1	Electromagnetism	Infinite
W$^{\pm}$	83 GeV/c^2	1	Weak (Charged Current)	10^{-18} m
Z^0	93 GeV/c^2	1	Weak (Neutral Current)	10^{-18} m
Gluon	~ 1 GeV/c^2 ?	1	Strong	10^{-16} m
Graviton	0.	2	Gravity	Infinite

Table 1.3. The force carrying particles. These particles are called bosons, because they have integral spin and obey Bose statistics.

All of these force carrying particles have been detected, except for the graviton. Modern particle physics refers to these forces as 'SU(3) $\otimes$ SU(2) $\otimes$ U(1)', a notation for the group operators that describe the strong, weak, and

electromagnetic interactions, respectively. Further, to fully describe the weak and electromagnetic forces they must be unified into a single electroweak field theory[6]

The standard model is the result of many years of experimental and theoretical effort. A wide variety of experimental techniques has been used to collect the data on which it is based. One technique, developed over the last 30 years, is to collide electrons and positrons in a storage ring. Electrons and positrons are circulated through a storage ring, in opposite directions, and steered to collide. When an electron and positron collide, they annihilate each other to form a state known as a virtual photon. The virtual photon then immediately decays to any of a variety of final states.

Over the past 15 years, this technique has provided many of the most important discoveries in particle physics. The charmed quark was discovered at the SPEAR storage ring in this manner, first hidden, bound with its antiquark[7] then openly, bound with noncharmed quarks in mesons[8] This has special significance as it was this discovery that really led to the acceptance of quark theory. The τ lepton was also discovered in this manner[9]

There are several reasons that e^+e^- collisions have produced so many interesting results. First, in e^+e^- annihilation, all of the input energy is available to produce final state particles. In contrast, in proton collisions, the proton energy is divided among the three quarks and their associated gluons. Second, the collisions are clean; the only particles emerging are those from the reaction. In hadronic collisions, uninvolved spectator quarks will produce extra particles, obscuring signals of interest. Finally, e^+e^- collisions are democratic; they will couple to any energetically accessible, spin conserving, particle-antiparticle final state[10] with a coupling (relative probability) proportional to the square of the final state electric charge. At higher energy, weak neutral current effects enter, allowing for a probe of the weak force. In the past, this has proven to be a very effective tool for uncovering new physics, and all indications are that it will continue to be for some time to come.

This dissertation will discuss studies done using this basic tool. The data used here were collected in e^+e^- annihilation at a center of mass energy of 29 GeV. At this energy, the virtual photon can decay in many ways. It can decay into pairs of charged leptons (e^+e^-, $\mu^+\mu^-$, or $\tau^+\tau^-$) or neutrinos, or any of the five known quarks: up, down, strange, charmed, or bottom, plus the appropriate antiquark. The relative probabilities depend on the square of the quark charges, giving d:u:s:c:b of 1:4:1:4:1.

Within the next few 10^{-23} s, this quark-antiquark pair will turn into a large number of mesons and baryons, in a process known as hadronization. Although hadronization has been extensively studied, and appears to agree well with QCD, the agreement is more qualitative than quantitative. The QCD calculations are extremely difficult, and the models that we have are semiphenomenological.

One of the most puzzling parts of this hadronization process is the subprocess of baryon production. One of the more surprising discoveries of high energy e^+e^- hadronization is the high rate of baryon production. Baryon production is not easily understood in the standard hadronization picture, in which $q\bar{q}$ pairs are pulled out of the vacuum, then combine to form mesons. One concept which has been used to understand this process is the diquark, a two-quark (as distinguished from a quark-antiquark) bound or semi-bound state. We do not know if diquarks are just a useful mathematical label, or if they have some physical significance.

One way to study this question is to study the production rates of different types of baryons, to see if they fit models based on diquarks. This can also provide information on more specific aspects of the hadronization process.

Chapter 2. Theory

Baryon production in e^+e^- collisions is a complex and poorly understood process. During the initial experiments in high energy e^+e^- collisions in the 1970's, the high rate of baryon production was somewhat of a surprise. As our understanding of e^+e^- hadronization reactions has developed, a variety of theories have been developed to explain general features of hadronization. These theories handle baryon production in a variety of ways.

Most of these theories can be grouped into two general classes: string models and cluster models. The basic idea behind the string model is that there is a color string stretching between the quark and the antiquark. As the quark and the antiquark move apart, the energy density of the string (it helps to think of it as a rubber band) increases, until it becomes energetically favored to materialize another quark-antiquark pair out of the vacuum. This idea comes from QCD, which postulates that as a quark and an antiquark are pulled apart, the force between them increases asymptotically to a constant. This means that they can never escape from each other, because their potential energy increases without limit. Thus, by creating another quark-antiquark pair between the primary quark and antiquark, the string tension is lessened, an energetically favorable condition. This process repeats itself on the two remaining strings.

The creation process continues, until the string runs out of energy. At this point, the quarks and antiquarks form into mesons, producing final state hadrons. Several points are worth making. First, it is unknown whether the quark creation process occurs sequentially, as described, or simultaneously. At this point, experimenters have not even begun to consider how to explore this question. Secondly, the process whereby the quarks form into hadrons may occur simultaneously with the creation process. This process is represented schematically in Fig. 2.1.

The cluster model is an alternate description of the same process. It is illustrated in Fig. 2.2.[11] In the following description, I will try to emphasize its

5-88   6028A2
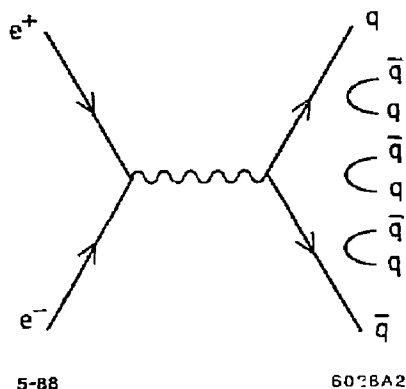
Figure 2.1. Hadronization according to the string model.

differences from the string model. Like the string model, the cluster model begins with a color string. However, it gives up its energy differently. In it, the string radiates soft gluons. (Gluons are the particles that carry the color force.) Gluons can decay into two gluons since they couple to each other. The process continues until the gluons reach a low enough energy, set arbitrarily, usually to around 1 GeV. Then, the gluons decay into objects known as clusters. These clusters then decay into hadrons.

The description neglects the possibility of baryon production. This corresponds with early ideas regarding hadronization; initially, it was expected that baryon production would be very small, since it required the creation of three quarks. However, when high rates of baryon production were observed, baryon production mechanisms were added to the theories. In most cases, this was done by introducing diquarks. A diquark is a two-quark bound or semi-bound state. At present, it is unknown to what degree diquarks are physical objects and to what degree they are useful mathematical concepts. However, most hadronization models give them a fair degree of physical significance. They do this

Clusters   Primary
                  hadrons
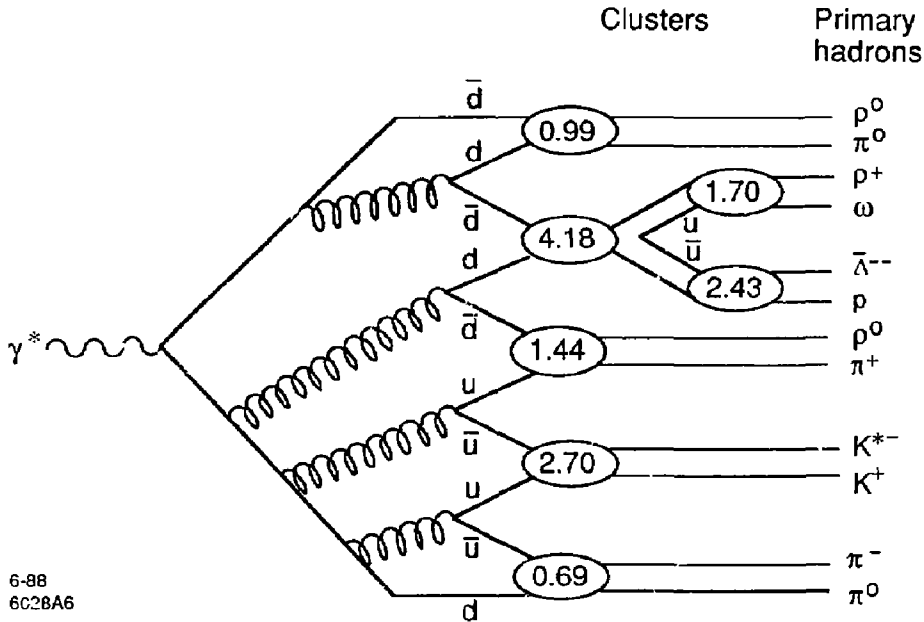
Figure 2.2. Hadronization according to the cluster model. The primary quark pair radiates gluons, shown by the spiral lines. The gluons decay into quark-antiquark pairs, which recombine to form clusters. The numbers in the clusters are their masses. A cluster with too high a mass decays into two lighter clusters before finally hadronizing.

by postulating that, occasionally, instead of materializing a quark-antiquark pair from the vacuum (or from a cluster), a diquark-antidiquark pair will be created instead. This diquark then combines with the previously created quark to produce a baryon. This is shown in Fig. 2.3(a). In some variants, it is possible to materialize a $q\bar{q}$ pair between the two quarks in the diquark. This is known as 'popcorn', as is shown in Fig. 2.3(b). A second, less accepted possibility is that diquarks may be created as leading particles, as shown in Fig. 2.3(c).

Before considering baryon production in greater detail, we must first examine the overall hadronization models more closely, beginning with string models.
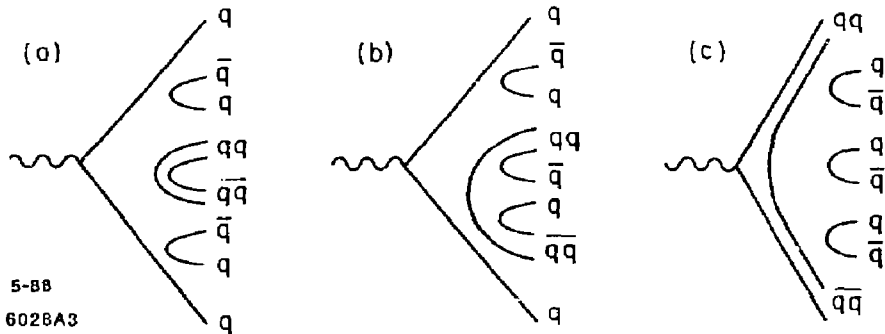
Figure 2.3. Baryon production in string models: (a) via a diquark; (b) via a diquark, with 'popcorn' creating a meson between the baryon and antibaryon; (c) via a leading diquark.

2.1 String Models

There are actually a wide variety of string models, with somewhat varying features. Although it preceded the concept of a string, the earliest stringlike e^+e^- hadronization model was the Feynman-Field (FF) model[12] Although it is now considered somewhat primitive and out-of-date, it illustrates the essential features of the string models which followed it.

When a virtual photon hadronizes, it can decay into a quark-antiquark pair via a well-understood quantum electrodynamics process. Each of the quarks then hadronizes into a jet. Simply put, a jet is a group of particles all traveling in roughly the same direction. Jets generally come from the same initial state; in e^+e^- annihilation, each quark spews off hadrons, which form a jet around it. In the original FF model, each jet hadronized independently; later variations have linked the two jets into a string. In each jet, hadronization is treated recursively. The primary quark, produced at a given momentum and direction, creates a color field

which is strong enough to create a $q\bar{q}$ pair from the vacuum. The antiquark from this pair joins the original quark to form a meson, while the new quark generates a color field which produces another $q\bar{q}$ pair. For sufficiently high momentum that mass effects are negligible, the fraction of the momentum taken by any meson pair is dependent only on a random distribution which is a function of a single variable, z, where

$$z = \frac{(E + P_l)_{hadron}}{(E + P_l)_{quark}} \ .$$

P_l is the particle momentum in the jet direction. In other words, z is the fractional longitudinal energy of the hadron compared to that of the original quark. The jet energy is recalculated after every quark emission; it is the energy remaining to be distributed. This quantity z is used in a fragmentation function, which gives the z distribution of created hadrons.

Many different fragmentation functions have been proposed, and used. The original FF function was:

$$f(z) = 1 - a + 3a^2(1 - z)^2$$

with a determined experimentally[13] to be 0.88. Others have used lower values of a. Another popular fragmentation function is:

$$f(z) = (1 - z)^\alpha$$

with $\alpha \approx 0.6$. In the original FF paper, these distributions served for all quarks; however later results have shown that heavy mesons[14] have a significantly harder momentum spectrum than light quarks. Because of this, flavor dependent fragmentation functions have been introduced. One form, suggested by quantum mechanics,[15] is:

$$f(z) = \left(z \left(1 - \frac{1}{z} - \frac{\epsilon_i}{1 - z} \right)^2 \right)^{-1}$$

where ϵ_i is approximately the squared mass ratio of the light and heavy quarks in the hadron.

In addition to their momentum in the jet direction, the mesons have some a momentum perpendicular to the quark jet, denoted by $P_\perp$. Feynman and Field gave the mesons a limited amount of transverse momentum, distributed according to a Gaussian distribution. This form is still used today, although recent work with the string model has given it some theoretical justification. Their quark perpendicular momentum distribution is given by

$$\exp(-P_\perp^2/2\sigma_{perp}^2) \ .$$

Meson $P_\perp$ is the sum of the two-quark $P_\perp$. To conserve $P_\perp$, each antiquark in the $q\bar{q}$ pair is given the momentum opposite to the quark, conserving momentum locally. Feynman and Field used 350 MeV/c for σ_{perp}, quite close to the current favorite values of around 300 MeV/c.

The other two parameters in the model determine the type of meson: its flavor and its spin. This is done with suppression factors, which give the relative production probability relative to some standard, usually taken to be up and down quarks. Up and down quarks always have equal production probabilities. Feynman and Field took the probability for strange $q\bar{q}$ production to be 0.4 of $u\bar{u}$ and $d\bar{d}$ production.

String models follow the same procedure, but have found a theoretical justification. They define a parameter called perpendicular energy, or $E_\perp$, where

$$E_\perp = \sqrt{M^2 + P_\perp^2} \ .$$

In string models, this energy comes from tension in the string. The creation of a $q\bar{q}$ pair requires that a hole in the color field appear, with lengths proportional to $E_\perp$. This hole will have to exist long enough for the quark and antiquark to join with the adjacent pairs to form colorless mesons. This is really quantum

mechanical tunneling, so the creation probability is given by

$$\exp - (E_\perp^2/2\sigma_{perp}^2) .$$

In this formulation, the only problematic parameters are the quark masses. Constituent quark masses must be used rather than current algebra ones.[16] Typical values, $m_{u,d} = 0.34$ GeV and $m_s = 0.51$,[1] give a suppression factor of $P_s = 0.63$, somewhat larger than the experimental results of 0.25 ± 0.02.[17] The difference is likely due to the difficulties inherent in attempts to calculate quark masses. In this formulation, the probability of producing charmed or bottom quarks is negligibly low. As we will see later, diquarks fit easily into this scheme.

Finally, we come to the question of quark spin, and consider how two quarks form into a meson. The original FF paper allowed mesons to form in either the pseudoscalar 0^- or the vector 1^- configuration, and arbitrarily gave these possibilities equal probability. It neglected the possibility of higher spin states.

Experiments, however, have shown that this is not very accurate.[18] Spin counting arguments suggest that the pseudoscalar to vector (P/V) ratio should be 1/3. In addition to this, the vector mesons should be suppressed because they are heavier. The HRS collaboration[18] found $P/V = 1/3(M_V/M_P)^\alpha$, with $\alpha = 0.55 \pm 0.12$.

One open question in the FF formulation concerned the ends of the quark jets. Eventually, the jet will run out of energy, and particle production must be terminated gracefully. In FF, when the jet drops below a certain energy, it is ended. Because of the differing hadronization in the two jets, this can lead to an energy momentum imbalance. Various authors have used different schemes to solve this problem. Hoyer[19] rescaled the momentum of each jet to achieve four-momentum conservation. Ali[20] boosted the hadrons to the center of mass frame, rescaled the energy and momentum, and boosted back to the lab frame. While these corrections are minor for the two-jet events described above, they become significant for events involving gluons.

The nonconsideration of gluon jets was one of the major defects of the FF model, and one of the first to be remedied by others. Both Hoyer[19] and Ali[20] were mainly interested in including gluon jets. Hoyer allowed for a single gluon to be radiated, with a separate fragmentation function and transverse momentum distribution. Ali allowed up to two gluons, as well as four-quark final states. He let the gluon decay into a $q\bar{q}$, using the Altarelli-Parisi splitting functions:[21]

$$f(z) = \frac{z^2 + (1-z)^2}{2}$$

to distribute the energy.

While the FF model was maturing, a theoretical framework was growing to accept it. This theoretical framework is based on the idea of a string which connects interacting quarks. It was originally introduced to high energy physics in 1974 when Artru and Mennessier used it to explain meson-meson scattering[22] They considered the mesons to be two quarks connected by a string. The scattering consisted of the two strings interacting.

In 1979, Andersson *et al.*, applied a semiclassical 1+1 dimensional (1 space, 1 time) string framework to quark jet hadronization[23] to form what is now known as the Lund model. Their effort was a bridge between the phenomenological descriptions of Feynman and Field, and theoretical QCD which makes few direct predictions. In e^+e^- annihilation, the string is created between the primary quark and antiquark. They are produced at a point, and travel outward, with a color field string between them. The string has a tension of about 1 GeV per fermi. $q\bar{q}$ pairs are materialized at random points along this string. In the Lund model, these points are required to be independent with a space-like separation. These requirements place constraints on the fragmentation function, which must have the form

$$f(z) \sim z^{-1} \exp(-bE_\perp^2/z)$$

where b is a free parameter. This form has several nice properties. It automatically

gives heavy quarks a harder fragmentation function. By its nature, the string
formulation is Lorentz invariant. This form has been refined further, to produce
the Symmetric Lund fragmentation function[24]

$$f(z) = (1 - z)^a z^{-1} \exp(-bE_\perp^2 / z)$$

where a and b are free parameters. Experiments[25] have shown that $a = 0.9$ and
$b = 0.7$ provide a good fit to the data, although a and b are highly correlated, and
other values also fit the data. The symmetric function comes about by requiring
that the string fragmentation turn out the same way whichever end of the string
one begins from.

Since the $q\bar{q}$ pairs are produced by tunneling from the vacuum, heavy quark
suppression is built in. Likewise, $P_\perp$ suppression is built in with the definition of
$E_\perp$.

The Lund model treats gluon jets simply as kinks on the $q\bar{q}$ string. When
the string hadronizes in its own rest frame, the kink (which can be thought of as
a partially doubled over string) naturally produces a jet.

A consequence of this is that there is much more string in the area near the
gluon. In many models, this string leads to increased particle production. In some
models, it can also lead to increased baryon production; it has been put forward as
the explanation for the increased baryon production observed in e^+e^- annihilation
on the Υ (1s).[26]

2.2   Cluster Models

While the string models had much closer ties to QCD than their predecessors,
they still lacked any provision for gluon self-coupling, to allow for QCD's non-
Abelian nature. To avoid these problems, cluster models have been developed.
They divide hadronization into several steps. The most commonly used cluster
models is the Webber model.[27] Cluster models generate the primary quark pair in
the same manner as string models. Then, instead of forming a color string, the

$q\bar{q}$ pair radiates gluons. These gluons may themselves decay into more gluons, demonstrating the non-Abelian nature of the color field. These gluons then decay into light-quark pairs, following the Altarelli-Parisi splitting function. These quarks combine with identically colored antiquarks, to form colorless clusters. The process of color matching is a bit of black magic known as preconfinement.

These clusters have varying masses; clusters with a mass above a given, arbitrary cutoff mass (around 3–4 GeV/c^2), are decayed into two lighter clusters. These clusters then decay into hadron pairs, conserving charge, flavor, and baryon number. The suppression of high mass objects occurs naturally because of the limited phase space.

The cluster model is mainly concerned with the early stages of the shower, with the hadronization treated as an afterthought. Cluster models differ from each other mainly in how they treat the initial gluon radiation. Despite the lack of attention to the final state hadrons, they do a surprisingly good job of modeling the hadron content of jets.

2.3   Other Models

There are many other models which have not attracted as much attention as the above two. The models are quite diverse; here we will discuss two. The first, known as the UCLA model, is a variant of the Lund model which has very limited theoretical justification, but which happens to fit the data very well with no free parameters[28]

The UCLA model is based on the Lund framework, but it handles hadronization very differently. Instead of first creating quarks, and then combining them into hadrons, the UCLA model produces hadrons directly, with suppression entirely dependent on hadron mass. It uses the Lund symmetric fragmentation function, except that it uses the hadron mass and hadron z directly. This eliminates all of the uncertainty inherent in quark mass calculations, spin

suppression parameters, and mixed states like the η. It also provides a very direct, simple route to incorporate higher spin hadrons.

The second model treats e^+e^- annihilation into hadrons as a simple thermodynamical process.[29] The hadronization process is treated as a fireball, with particle selection and fragmentation based solely on the partition function. It does a fairly good job of reproducing many aspects of the data. There are many other models which incorporate various thermodynamic elements into their formulation. Unfortunately space does not permit their inclusion here.

So far, I have said little about baryon production in these models. Before discussing that topic, it is worth discussing some basic ideas about baryons.

2.4 Baryons

Baryons are three-quark bound states. They include common, long-lived particles like the proton and the neutron, and rarer, short-lived ones such as the Ω^- and the Λ_c^+.

Baryon wave functions may be broken down into their constituent parts:

$$\Psi_b = \Psi_{color} * \Psi_{spin} * \Psi_{flavor} * \Psi_{space} \ .$$

Since baryons are fermions, their wave functions must be antisymmetric. QCD tells us that Ψ_{color} is totally antisymmetric, so the rest of Ψ must be symmetric. Ψ_{flavor} is determined by the flavors of the baryons constituent quarks. If we limit ourselves to up, down, and strange quarks, baryon flavor is described by SU(3) group theory, by combining three triplets:

$$(3) \otimes (3) \otimes (3) = (1)_A \oplus (8)_M \oplus (8)_M \oplus (10)_S$$

where the subscripts A, M, and S denote antisymmetric, mixed, and symmetric, respectively.

To relate these multiplets to physically observable particles, we must combine this $SU(3)_{flavor}$ with spin. Quarks are spin $1/2$, so we can combine flavor with a $SU(2)$ spin group, giving us a $SU(6)$ group:

$$(6) \otimes (6) \otimes (6) = (56)_S \oplus (70)_M \oplus (70)_M \oplus (20)_A \; .$$

These multiplets decompose back into the $SU(3)$ flavor multiplets as follows:

$$(56) =^4 (10) \oplus^2 (8)$$

$$(70) =^2 (10) \oplus^4 (8) \oplus^2 (8) \oplus^2 (1)$$

$$(20) =^2 (8) \oplus^4 (1)$$

where the superscripts give the spin multiplicities of the multiplets. The ground state octet and decuplet baryons that we are all familiar with come from the (56) representation; the (20) and (70) representations cannot be made symmetric without introducing a radial excitation not present in the ground state configurations.

The ground state is symmetric in space and antisymmetric in color, so symmetric (56) gives the allowed baryon ground states. It splits up into the four spin states for the spin $3/2$ decuplet, and the two spin states of the spin $1/2$ octet.

While group theory tells us a lot about baryon structure, it leaves us totally uninformed about baryon dynamics. Also, it gives us no clue as to how baryons are produced in e^+e^- annihilation. Most of the theoretical ideas regarding baryon production in e^+e^- annihilation are based on the idea of diquarks, which are discussed in the next section.

2.5 Diquarks

Although Gell-Mann used the term 'diquark' in a footnote to his 1963 paper,[30] the first significant treatment of diquarks did not appear until 1966.[31] Early diquark

theory treated the proton as state consisting of a two-quark boson and a single-quark fermion[32] These efforts were an attempt to solve some problems in baryon mass calculations. However, the idea never really caught on, and diquarks fell into disuse. In the late 1970's they were revived to explain baryon production in e^+e^- collisions. More recently, they have been used to explain scaling violations in deep inelastic scattering[33]

QCD supports the idea that diquarks should have some significance. Two isolated quarks should attract each other if they are in the correct spin state. The diquark wave function is given by:

$$\Psi_{diquark} = \Psi_{color} * \Psi_{spin} * \Psi_{flavor} * \Psi_{space} .$$

Ψ_{flavor} is isospin, supplemented to include the heavier quarks. Ψ_{color} is the color part of the wave function. It may be represented by an antisymmetric color triplet, denoted by (3). When two quarks are combined, they can either combine into a symmetric sextet, denoted by (6) an antisymmetric triplet, denoted by ($\bar{3}$). This can be shown as:

$$(3) \otimes (3) \rightarrow (\bar{3}) \oplus (6) .$$

QCD calculations show that (6) is unbound because the force between the two quarks is repulsive. Also, (6) cannot combine with (3) to form a color singlet. Therefore, (6) cannot be part of a baryon.

On the other hand, ($\bar{3}$) can form a baryon:

$$(3) \otimes (\bar{3}) \rightarrow (1) \oplus (8) .$$

Calculations indicate that a ($\bar{3}$) diquark is stable, because the interquark force is attractive. From this, we learn that stable diquarks are realistic in a QCD framework, and that the color part of the diquark waveform is antisymmetric.

Of course, this is an oversimplification, because it neglects the effects of quark spin. Quarks are spin 1/2, so that instead of SU(3), we should use SU(6) to include spin. If we do that, we get:

$$(6) \otimes (6) \rightarrow (21) \oplus (15)$$

The interquark force for the (15) is repulsive, and the (15) diquark should not exist.

This leads to one of the most important predictions of the diquark model. In a model where baryons are composed solely of a diquark plus a quark, the baryons made from the (15) do not exist, while in a strict three quark model they do exist.[34]

Using the (21) symmetric diquark to form baryons leads to

$$(21) \otimes (6) \rightarrow (56)_S \oplus (70)_M$$

compared with three quark, no diquark SU(6) which gives

$$(6) \otimes (6) \otimes (6) \rightarrow (20)_A \oplus (56)_S \oplus (70)_M \oplus (70)_M$$

The diquark model predicts fewer baryon states; one $(70)_M$ and the $(20)_A$ are missing from the spectrum. Unfortunately, as we saw in the last section, these extra states do not appear in the baryon ground states which is composed solely of $(56)_S$. Nor does it appear for the first orbitally excited states, which are composed solely of $(70)_M$. The states are present at higher orbital excitations, but the data available can not yet differentiate between the two spectroscopies.

However, diquarks theories can affect other areas. One can occur in diquarks made out of two same flavor quarks. In this case, Ψ_{flavor} is necessarily symmetric. However, by the Pauli exclusion principle, the complete two quark wave function must be antisymmetric. This means that the Ψ_{spin} must be

symmetric; the two-quark spins must be aligned, so that same flavor diquarks must be spin 1. Calculations indicate that this spin 1 configuration, with spins aligned, is energetically disfavored, so spin 1 diquarks such as uu, dd, and ss should be suppressed.

Experimental data from deep inelastic scattering experiments confirms this. In deep inelastic scattering, produced baryons are largely spin 1/2, indicating that the diquarks that they are formed from, whether a fragment of the original nucleon or produced in the collision, are mostly spin 0.[35]

2.6   Diquarks in e^+e^- Hadronization

As was mentioned earlier, the copious rate of baryon production was one of the big surprises in early studies of e^+e^- collisions. While baryon production has been added or included in most hadronization models, in many of the early models, its inclusion was often very much *ad hoc*.

Most baryon production models are predicated on the idea of diquarks. Instead of materializing a $q\bar{q}$ pair, a diquark-antidiquark pair is produced. This is typically suppressed to some degree, the amount depending on the model.

One of the first attempts to include baryon production was by Casher *et al.*[36] Their model treated hadronization as tunneling in a chromoelectric flux tube of uniform density. After the quarks are produced, they can combine into either mesons or baryons. The baryons are suppressed both for dynamical reasons, and because they are more complicated, requiring a three-quark configuration compared to a simpler $q\bar{q}$ meson.

Another early attempt to model baryon production was by Meyer[37] who simply allowed occasional two-quark two-antiquark sets to be pulled from the sea. He gave this an arbitrary 0.075 suppression factor. Unlike most of the models to come, Meyer allowed diquarks to be the leading particle in jets, as shown in Fig. 2.3(c). This amplitude for this process depends on the size of the diquarks. The larger the diquark, the smaller the probability for production. Meyer also set

the relative probabilities of octet to decuplet production equal to the pseudovector to vector probability.

The Lund group[38] was the first to introduce a systematic scheme for modeling baryon production that was widely accepted. They expanded their earlier string scheme to allow for the possibility of diquark-antidiquark production. This diquark would then combine with a quark from a $q\bar{q}$ tunneling to produce a baryon. They calculated the probability for diquark production using diquark masses. Unfortunately, since diquark masses are so uncertain, this gave poor results, and they then allowed diquark suppression to be a free parameter.

Diquarks introduce several additional levels of complexity in calculating suppression factors. First, there are two flavors to choose, and their combined probability is not necessarily a product of their individual probabilities. Second, diquarks could be spin 0 or spin 1, although data mentioned above[35] indicates that the former predominate. The Lund model handles these problems by calculating the various diquark masses for the various flavor and spin configurations, and using the transverse mass previously described to provide the suppression. Again, because of the uncertainties in the calculation, in their Monte Carlo program version, the Lund authors allow these various suppression factors to be free parameters.

The requirement that a baryon come from a diquark and a quark will produce some surprising effects. One occurs when one considers the possibility of charm baryon production. Since charmed quarks essentially only occur as leading quarks, in a charmed baryon, the diquark must comprise the other two quarks. Consider the four baryons made up of a charmed quark and two light quarks: Λ_c^+(cud, isospin 0), Σ_c^{++}(cuu, isospin 1), Σ_c^+(cud, isospin 1), and Σ_c^0(cdd, isospin 1). Since the charmed quark is isospin 0, the baryon isospin comes entirely from the light quarks. For diquarks composed of two light (up or down) quarks, spin equals isospin, as mentioned above, and experimental evidence indicates that spin 1 diquarks are heavily suppressed. This indicates that the $\Sigma_c : \Lambda_c$ ratio should

be small, even though both baryons are spin 1/2 and composed of similar quark combinations. Thus, measurement of the $\Sigma_c : \Lambda_c$ ratio can provide an interesting test of diquark reality.

The original Lund model contained one simplification: baryon pairs were always produced adjacent in rank on the string. Recently, the model has been expanded to allow for meson production between a baryon antibaryon pair[39] The the color fluctuations required to produce a $qq\overline{qq}$ set are large enough so that a $q\overline{q}$ pair can be produced in the middle of the $qq\overline{qq}$. One of the quarks in the $q\overline{q}$ will combine with an antiquark in the $qq\overline{qq}$, producing a meson between the two baryons. This procedure has been called 'popcorn'. Besides spreading out the two baryons in phase space, this also reduces baryon-antibaryon flavor correlations. Both of these effects are extremely difficult to study experimentally, so evidence for or against 'popcorn' may be a long way away.

Cluster models treat baryon production in a similar manner to meson production. Meson and baryons are both produced in the decays of colorless clusters, with the various suppression factors coming from mass-based phase space suppression. Likewise, in the UCLA model, baryon production rates depend solely on the baryon masses.

2.7 Experimental Links

All of these baryon production models are in at least reasonable agreement with the data. This is partly because the models tend to give similar predictions, and partly because the available data is quite limited. Also, the models have evolved with time, to keep pace with the latest data.

This thesis looks at areas which can provide tests of these models: strange and charmed baryon production rates. By comparing octet (spin 1/2) and decuplet (spin 3/2) baryon production rates, spin-1 diquark theory can be tested. In particular, the Ω^- can provide a good test of production models.

Although they are very difficult to observe, studies of cnarmed baryon production rates can further test these models.

Chapter 3.   Experimental Apparatus

The data used in this analysis were taken with the Mark II/PEP5 detector at the PEP storage ring. Only data taken after the summer of 1982, when a high precision vertex drift chamber was installed are used. The total accumulated luminosity was 207 pb^{-1}.

3.1   The PEP Storage Ring

The PEP (Positron Electron Project) storage ring is a 700 m diameter electron positron storage ring, as shown in Fig. 3.1. Three electron and three positron bunches, rotate in opposite directions, colliding at six points around the ring. Although the ring was designed to accommodate collision energies up to 36 GeV,[40] it has been run at an energy of 29 GeV. This slightly lower energy provides a higher luminosity, and thus a higher event rate. Collisions can occur every 2.4 μsec. The ring reached a maximum luminosity of 3×10^{31} cm^2 sec^{-1}, giving typical daily integrated luminosities of 1 pb^{-1}, or approximately 400 hadronic events per day. The electron and positron bunches were filled by the SLAC linac roughly once every four hours. Generally, they were dumped and refilled when the luminosity declined to a third or so of its initial value.

At the interaction points, the PEP beams were ellipsoidal, roughly 500 μm wide by 100 μm high, and a few centimeters long. The collision point moved slightly depending on the exact machine tuning. Generally, although not always, it was stable over an entire fill. This small beam size made it easy to identify tracks not coming from the primary interaction point, an important component of the analyses described here.

3.2   The Mark II Detector

The Mark II/PEP5 detector[41] was a general purpose detector designed to study the physics of e^+e^- annihilation at high energies. It had good charged particle tracking with an excellent vertex detector, good electromagnetic
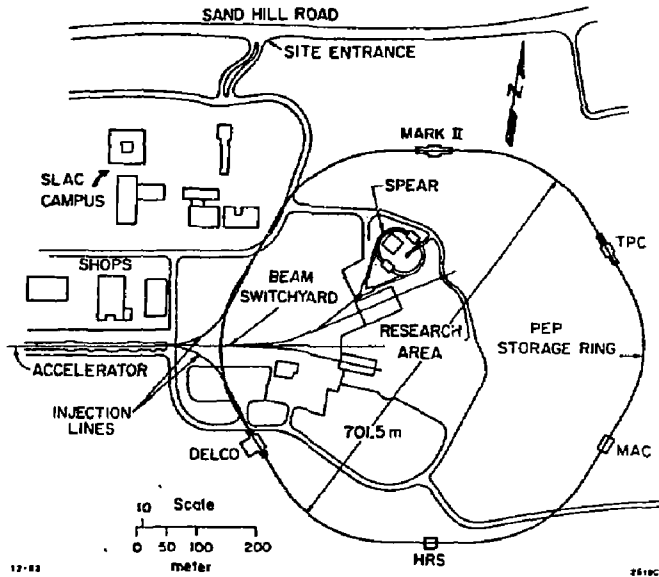
Figure 3.1. Overview of the PEP storage ring and the SLAC site.

calorimetry, and a reasonable muon detection system. It also had a time-of-flight measurement system, which was useful mainly at lower energies (before moving to PEP, the Mark II detector took data at the lower energy SPEAR storage ring), and two endcap calorimeters. It took data at PEP from the fall of 1980 to June *of 1984, although the vertex chamber was not installed until the summer of 1982.*

The Mark II Detector is shown schematically in Fig. 3.2, which reveals that the Mark II detector is composed of a large number of different subsystems. It is the synergistic effect of these different components with differing detection capabilities, that gives the Mark II detector its power.
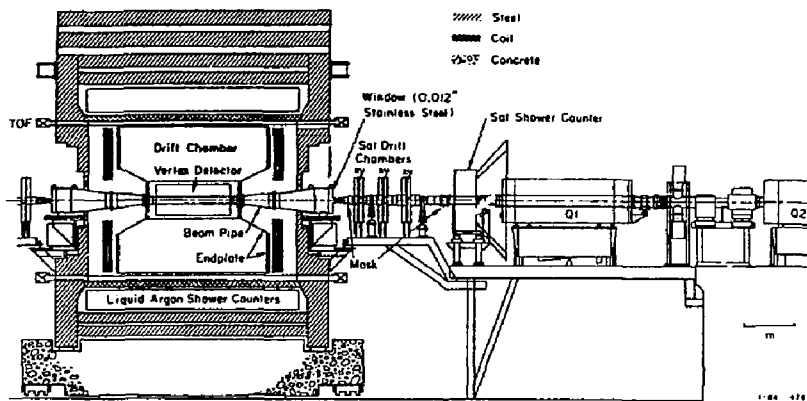
Figure 3.2. Side view of the Mark II detector. The steel serves as both a muon detector and as a flux return for the magnet coil. Q1 and Q2 are quadrupole magnets that focus the beam at the interaction point.

3.2.1 Main Drift Chamber

The analyses described here made extensive use of information from the main drift chamber. The chamber provided tracking information for charged particles, measuring the sign of their charge and their momenta. The drift chamber analysis software described each track as a helix, allowing the tracks distances of closest approach to the origin to be found.

The PEP5 drift chamber[42] is shown in Fig. 3.3. It had 16 layers, with between 144 and 264 cells per layer. There were a total of 3,204 cells. Each cell was composed of a single 38.1 μm diameter 95% copper, 5% beryllium sense wire, surrounded by six 152 μm diameter field wires composed of the same material, as shown in Fig. 3.4. The field wires shaped the field. They were designed to keep the drift velocity as uniform as possible. The inner six layers were small cells,
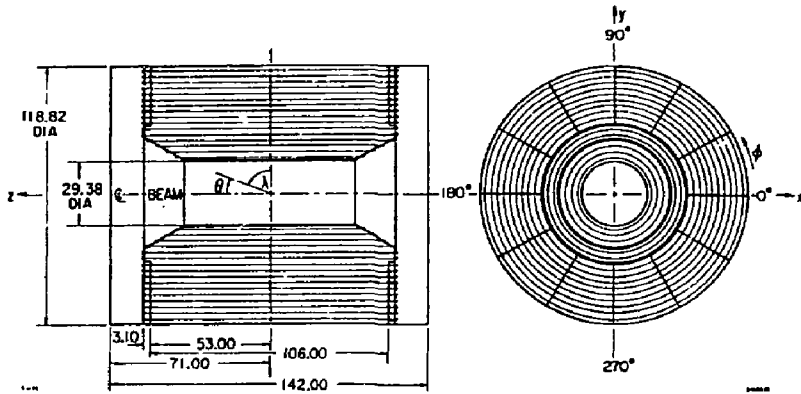
Figure 3.3. The Mark II/PEP5 drift chamber geometry. This diagram defines θ, λ, and ϕ as used in the tracking programs.

which reduced the probability of two tracks passing through a single cell, while the outer ten layers had larger cells, to simplify the construction.

The chamber gas was 50% argon and 50% ethane, by volume. Later, when the drift chamber began to draw high currents, a small amount (0.7%) of oxygen was added to improve operation.

Table 3.1 lists the parameters of the drift chamber layers. Six layers were axial, while the other 10 were offset at a roughly 3° angle. These small angle stereo views provided z information for the tracks. The wires were arranged in an axial, stereo +, stereo −, axial, stereo +, etc. pattern, with the + and − referring to the sign of the stereo angle.

For all cells, the sense wires were kept at a grounded potential. In the small cells, the voltage was initially kept at −2.95 kV, while in the large cells they were at −3.5 kV. When the drift chamber began drawing large currents, these voltages were reduced to −2.65 and −3.0 kV, respectively. This voltage reduction reduced the efficiency for some of the layers significantly. Later, when the oxygen was added to the chamber, the voltages were raised again, to −2.85 and −3.20 kV, respectively.
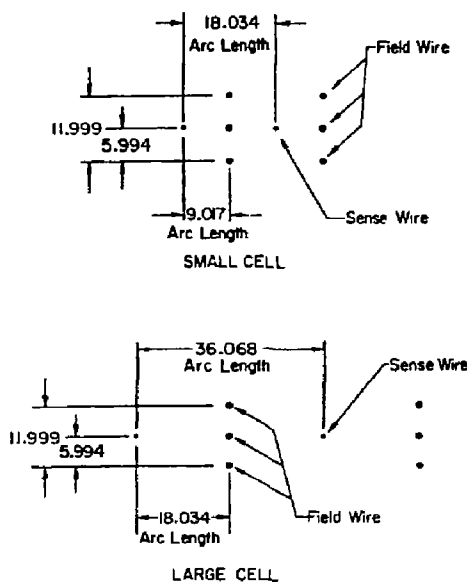
Figure 3.4. The large and small cells in the PEP5 drift chamber.

The signals from the sense wires were fed through two to four m of 50 Ω cable to a LeCroy LD604 preamplifier/discriminator. The discriminator threshold was typically 500 mV. The preamplifier output was fed through 25 m of twisted pair to a Time-to-Amplitude Converter (TAC). The TAC input started a capacitor charging. It continued to charge until it received a stop pulse. This voltage was then digitized by a BADC, as described below.

The drift chamber resolution depended on many factors. For tracks passing near the center of the cells, not too close to the sense wire or the field wires, it was about 150 μ for the large cells, and slightly worse for the small cells. For tracks in other regions, it degraded, as shown in Fig. 3.5.

Cell Size	Layer	Radius (cm)	Length (cm)	Angle (°)	Cells
Small	6	41.36	198.41	0	144
	7	48.26	222.29	+3.12	168
	8	55.15	246.17	−2.90	192
	9	62.04	270.05	0	216
	10	68.94	278.64	+2.90	240
	11	75.83	278.64	−2.90	264
Large	12	82.72	264.16	0	144
	13	89.62	264.16	+3.07	156
	14	96.51	264.16	−3.07	168
	15	103.40	264.16	0	180
	16	110.30	264.16	+3.07	192
	17	117.19	264.16	−3.07	204
	18	124.08	264.16	0	216
	19	130.98	264.16	+3.07	228
	20	137.87	264.16	−3.07	240
	21	144.77	264.16	0	252

Table 3.1. Drift chamber construction. The angle is the stereo angle. Length is the active length of the sense wires. Layers 12–21 have a shorter active length than layers 10–11 because they are mounted on an thick aluminum honeycomb endpiece, while layers 10–11 are mounted on a thin aluminum cone. The layer number also gives the number of high voltage segments.

3.2.2 Vertex Chamber

Inside the main drift chamber is a smaller, high precision drift chamber known as the vertex chamber.[43] While it also improved the detector overall momentum resolution, its main function was to measure the distance of closest approach of particles to the origin. This information was primarily useful for measuring the
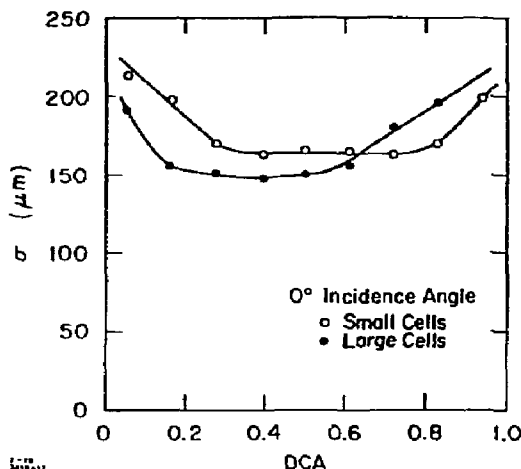
Figure 3.5. Drift chamber resolution as a function of distance from the sense wire.

lifetimes of short-lived particles, but it was also very useful in improving the purity of strange baryon samples.

Figure 3.6 shows the vertex chamber. It had seven layers, all axial, organized into an inner group of four layers, and an outer band of three layers, as shown in Table 3.2. This arrangement, with inner and outer bands, allowed particle trajectories to be projected accurately back to the origin, without requiring a prohibitively high number of wires.

All of the cells were roughly identical, and were laid out as shown in Fig. 3.7.

Many elements of the chamber were optimized to achieve the best possible resolution. The wire feedthrough positions were controlled to within 20 μm.[44] High resolution electronics were used to read out the signals. Unfortunately, these electronics also suffered from crosstalk problems between adjacent channels. This crosstalk reduced the resolution significantly in dense jets.[45]
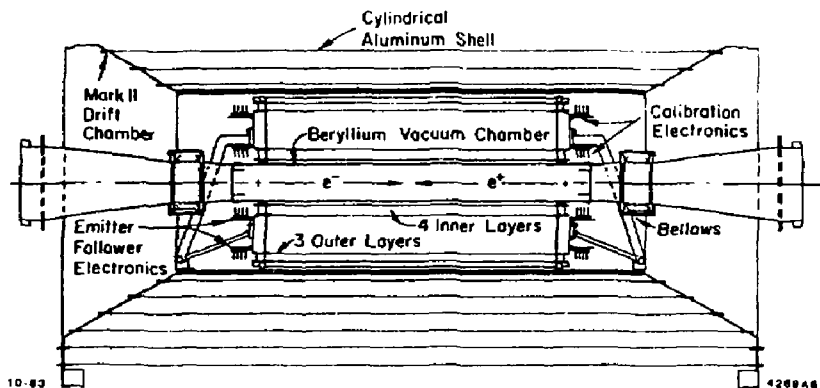
Figure 3.6. The PEP5 vertex chamber. It fits inside the main drift chamber.

Band	Layer No.	Radius (cm)	Number of Sense Wires
Inner	1	10.12	60
	2	10.97	65
	3	11.81	70
	4	12.65	75
Outer	5	30.37	180
	6	31.21	185
	7	32.05	190

Table 3.2. Vertex chamber layer arrangement. The cells were arranged in two bands. This allowed the tracks to be accurately projected back to the origin, while keeping the number of channels manageable. Since the cells were all the same size, the number of cells increased with the radius.

To maximize gas gain (and therefore optimize resolution) and efficiency, the chamber was initially run with the sense wires grounded and the field wires set to -2.25 kV. This high voltage led to the chamber drawing fairly high currents and, after several months, it was necessary to reduce the voltage.
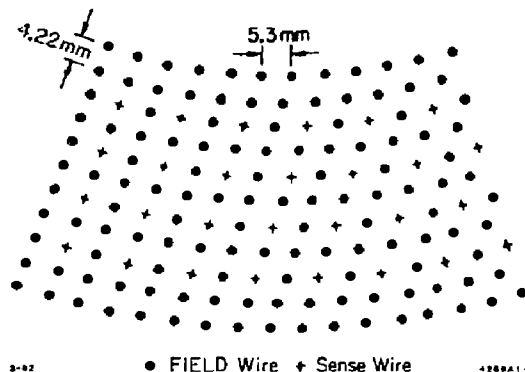
Figure 3.7. Layout of the vertex chamber cell. One tenth of the inner band is shown here.

The chamber was initially run with a fully saturated gas, 50% argon and 50% ethane. Later, the gas was bubbled through ethanol, to improve operating stability.

Also installed with the vertex chamber was a beryllium beam pipe. This pipe was designed to minimize multiple scattering. It was 1.42 mm thick beryllium coated with 50 μ thick titanium to stop the synchrotron radiation. It was only 0.6% radiation length thick.

All of these techniques led to a position resolution of 80 μm per hit for isolated tracks. This allowed tracks to be extrapolated back to the interaction region with an accuracy of $\sqrt{(85\,\mu\text{m})^2 + (95\,\mu\text{m}/p)^2}$, where p is in GeV/c. The first contribution is due to position resolution, and the second is due to multiple scattering.

Because of the crosstalk problem, the resolution for tracks in jets was up to 50% worse[45] The degree of degradation depended on how close together the wires were, and whether they shared a preamplifier card.

The main drift and vertex chamber together had a momentum resolution for charged tracks given by

$$\delta p/p = \sqrt{(0.010\,p)^2 + (0.025)^2}$$

where p is in GeV/c. The first term gives the error due to the resolution, and the second gives that due to multiple scattering. This resolution is determined from studies of Bhabha electrons and cosmic rays. Bhabha electrons give a good estimate of the resolution at the beam energy, while cosmic rays can be studied at a variety of momenta by comparing the incoming and outgoing track halves. The resolution is somewhat worse for tracks in dense jets.

3.2.3   Time-of-Flight System

Outside of the drift chamber was an array of 48 time-of-flight counters. Each counter consisted of a 2.5 mm thick slab of Pilot F scintillator, mounted at an average radius of 1.51 m from the interaction point. They were 3.43 m long, giving a solid angle coverage of 68% of the 4π solid angle. The slabs were each read out by two Amperex 2230 phototubes. The phototubes were mounted on opposite ends of the detector, allowing a measurement of mean time and z position. For a track which fired both counters, the resolution, averaged over the entire PEP run, was 380 psec. This resolution worsened over time as the scintillator suffered radiation damage.

3.2.4   Magnet

The magnet was outside of the time-of-flight system. The magnet produced a uniform, solenoidal magnetic field, parallel to the beam line, causing charged particle trajectories to curve, allowing particle momenta to be measured.

The magnet was originally designed to produce a field of 4.5 kG, and it operated that way at SPEAR and during the early PEP running. In the summer of 1982, the magnet developed a short circuit between its inner and outer layers. The

short was later found to be due to corrosion caused by the cooling water. It proved irreparable, and for the remainder of Mark II/PEP5 it was operated at roughly half field (2.35 kG). This had two effects. The reduced magnetic field degraded the momentum resolution. On the other hand, it allowed lower momentum particles to be tracked. For this second reason, the low magnetic field was important to the strange baryon analysis described here.

The steel in the muon system served as a flux return for the magnet.

3.2.5   Barrel Calorimeters

Electromagnetic calorimeters were located outside of the magnet.[46] These calorimeters were used to measure the energies of photons and electrons, and differentiate between electrons and other charged particles. The calorimeters were lead/liquid argon, divided into eight modules, arranged in an octagonal array. The eight gaps between the modules created holes in the calorimeter. After fiducial cuts to avoid these holes, the calorimeters covered 64% of the 4π solid angle.

Each module contains 18 layers of 3 mm thick liquid argon gaps, separated by 2 mm thick lead absorbers. Each gap is segmented into readout strips. In nine of the planes, the strips are parallel to the beam line. These 3.5 mm wide strips are called F (for ϕ) planes. The strips were separated by 0.3 mm gaps, giving a 3.8 mm strip to strip spacing. Six planes of 3.5 mm strips were oriented perpendicular to the beam line, and were called T (for θ) planes. The three planes at a 45° angle to the F and T planes have 5 mm wide strips, and were called U planes. The charge in the liquid argon was collected by a 1200 V/mm electric field. The total calorimeter thickness was 14.8 radiation lengths.

The 18 layers of lead shielded strips were preceded by two 8 mm thick liquid argon gaps, oriented along the F plane, and called trigger gaps. The trigger gaps allowed for an early sampling of showers that began in the magnet coil, and the original plans called for including the trigger gap in the charged particle trigger.

The fine segmentation of the liquid argon allowed for precise determination of shower position; however, it also led to a very large number of electronics channels. To reduce the amount of electronics required, toward the back of the calorimeter, some strip planes were ganged together, as shown in Fig. 3.8. In addition, in the back of the calorimeter, pairs of adjacent channels were wired together. This reduced the number of electronics channels to a manageable 3,000.

Liquid Argon Calorimeter Ganging Scheme
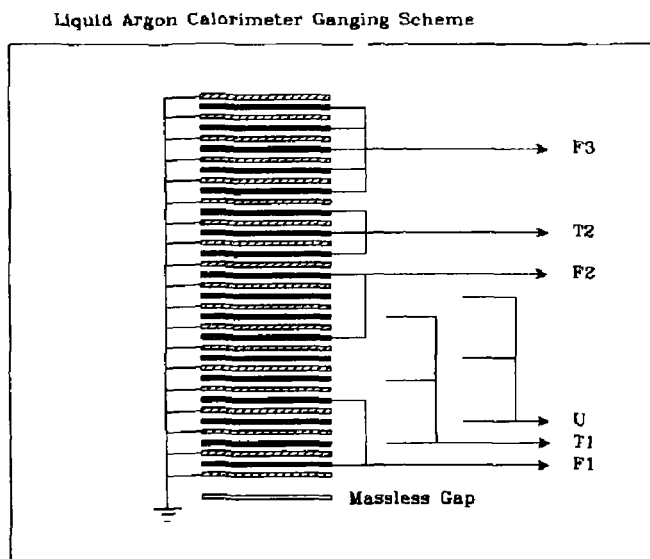
Figure 3.8. The liquid argon calorimeter ganging scheme. The F strips and the massless (trigger) gap were parallel to the beam line, the T strips were perpendicular to it, and the U strips ran at a 45° angle to it.

The high segmentation in both depth and angle gave the liquid argon the ability to effectively distinguish electrons from hadrons, and gave it a fairly good energy resolution. For photons, the energy resolution was $14.5\%/\sqrt{E}$.

Electrons were distinguished from charged hadrons on the basis of the physical size and amount of their energy deposition in the calorimeter. Electrons were expected to quickly shower and deposit most of their energy in the calorimeter, while hadrons generally passed through the calorimeter with minimal energy deposition. Those hadrons that did deposit significant energy in the calorimeter generally spread that energy over a much larger area than electrons. The electron-hadron separation depended on the particle energy and environment. For isolated tracks, the π misidentification was around 0.5% for an electron efficiency of around 90%. This will be discussed in greater detail in the following chapter.

3.2.6   Muon System

The muon system was outside of the electromagnetic calorimeters. It consisted of four walls, located above, below, and on each side of the detector, covering 45% of the 4π solid angle. Each wall consisted of iron absorber interspersed with four layers of proportional tubes.

The proportional tubes were made out of aluminum extrusion, as shown in Fig. 3.9. Particles traversing all four layers of the muon system at normal incidence traversed 7.4 interaction lengths. This thickness reduced the contamination from hadronic punchthrough to a few percent, while accepting muons down to a momentum of 2 GeV/c.

3.2.7   Endcaps

The two PEP5 endcaps consisted of lead/proportional tube calorimeters[47] Because the lead was too thin (2.3 radiation lengths), the calorimetry was of limited accuracy, and the system was not used very much.

3.2.8   Small Angle Tagging

At small angles to the beam, there was a small angle tagger (SAT) system[48] It contained a set of drift chambers which were used to detect charged particles
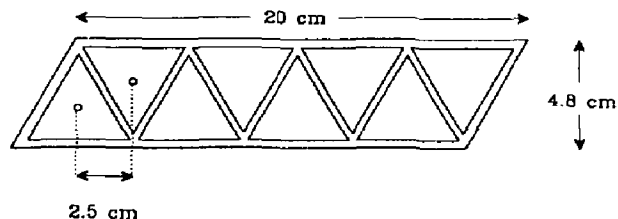
Figure 3.9. The muon system proportional chamber geometry.

coming from the origin, and a calorimeter to measure energy deposition. It was used to tag two-photon events, and as a luminosity monitor.

3.2.9 Trigger

Since the PEP beams collided every 2.3 μsec, and the Mark II data acquisition system could only collect a few events a second, some sort of a system was needed to decide which collisions were potentially interesting. The Mark II trigger did this in a two-stage process.

The Mark II trigger received inputs from most of the detector elements described above, divided into two classes. The barrel and endcap calorimeters energies were summed, and the sums compared with a threshold. Each barrel module and endcap had two different thresholds. Various combinations of the high and low thresholds could be required for a trigger.

The drift chamber, vertex chamber, and time-of-flight system were incorporated into the trigger somewhat differently, in a two-stage process. Each drift chamber layer, vertex chamber layer, and the time-of-flight system was ORed together in the first stage. Each layer OR was fed into a programmable logic unit, which produced a primary trigger pulse if enough layers were hit. This pulse was fed, along with the calorimeter triggers, into a RAM based programmable trigger unit, which made the primary trigger decision.

In the absence of a primary trigger, the detector was cleared in time for the next beam crossing. If there was a primary trigger (the PEP primary trigger rate was around 1.5 kHz), then the secondary trigger was started.

The secondary trigger[49] used information from the drift and vertex chambers and the time-of-flight system, but in a more sophisticated way than the primary trigger. The secondary trigger consisted of a fairly simple, but very powerful hardwired pattern recognition processor which searched for charged particle tracks in the drift chamber. The pattern recognition was done in parallel by 24 curvature modules, each of which searched for tracks of a given charge and momentum slice. The search started at $\phi = 0$, and progressed around the drift chamber in 252 steps, each taking 100 nsec. The progression in ϕ was achieved by connecting each chamber layer as a circular shift register, then shifting around the chamber in unison. A burped clock was used to compensate for the differing numbers of cells in each layer. This burped clock clocked each layer at a different rate, depending on the number of cells it contained. The number of hit cells required to make a track candidate was programmable, and could be varied depending on the noise level in the drift chambers.

The normal triggering requirements were that at least two good tracks be found by the curvature module setup, or that energy depositions be found in two calorimeter modules.

The track finding processor was always run with extremely loose requirements, so that its efficiency was very high. It was essentially 100% efficient for detecting the hadronic events used in the analyses presented here.

3.2.10   Data Acquisition, Monitoring, and Experimental Control

In an experiment the size of Mark II, a substantial fraction of the experimenter's effort is devoted to the problems of data collection, experimental apparatus monitoring and control. At Mark II/PEP5, these activities were done with the aid of a VAX 11/780 computer, connected to a CAMAC network,

interfaced with a VAX Camac controller[50] (VCC). To keep the VAX from being overwhelmed, the CAMAC branches contain a significant amount of distributed intelligence, in the form of microprocessor-controlled Brilliant Analog-to-Digital Converters[51] (BADC's). These BADC's served several functions. Generally, there was one BADC per CAMAC crate. When a secondary trigger was received, the VCC broadcast a general start command, and the BADC's began reading out the channels in each CAMAC crate. They digitized the voltages read out and converted them to physics quantities (drift times in 0.1 nsec units, calorimeter energies in 0.1 MeV, etc.). These conversions were performed using previously calculated calibration constants. The BADC then zero suppressed the data, compacting it to a reasonable size, and waited for the VCC to read it out. This initial processing and zero suppression greatly reduced the amount of data to be read out.

As previously mentioned, the CAMAC readout was controlled by the VCC, which is a simple bit slice processor. During data acquisition, it sequentially read out CAMAC crates, guided by a file containing a list of addresses. This system had two advantages. First, it was very easy to insert or remove detector systems from the readout by modifying the database. Second, and more importantly, it automatically formatted the input data. The formatted data was put directly into the VAX main memory via a DMA (direct memory access) controlled by the VCC. The VAX simply wrote the data to tape.

Because data collection took little VAX processing time, the VAX was able to spend a substantial portion of its time monitoring the data quality. It continuously histogrammed important quantities, such as drift chamber drift times, liquid argon occupancies, and trigger statistics. In addition, it did online event reconstruction on a fraction of the triggered events. This allowed it to monitor many additional quantities, such as tracking residuals and muon detection efficiency. Changes in these distributions could signal subtler problems, such as bad drift chamber gas.

In addition to this monitoring, every four minutes the VAX initiated a set of detector tests, known as a four minute interrupt. These tests, which took a few seconds, ensured that critical parts of the detector were functioning. At these interrupts, many voltages and currents were checked and recorded on tape. This included all of the high voltages, as well as the NIM bin and CAMAC crate voltages.

Since the parameters of many detector channels could drift with time, each system was calibrated once every eight hour shift. These calibrations varied from system to system, but generally involved injecting known charges into the system preamplifiers, and comparing the injected charge with the BADC output. The constants found from this calibration were then stored in the BADC. Besides calibrating the electronics, this procedure identified bad channels, and many other problems.

Besides the calibration, each shift also performed tests on other systems such as the trigger, and manually checked the power supply currents and voltages, detector gas supplies, liquid argon system temperatures, and many other parameters.

Chapter 4.   Offline Analysis Software

The data collected with the Mark II detector must be extensively processed before it is usable in most physics analyses. Much of the processing is common to most analyses, and it is only done once. This processing is described in this chapter, along with much of the other group software.

Because the detector is so complicated, and because our physics calculations are so difficult, it is necessary to compare the results of our analyses with 'fake' data, known as Monte Carlo data. The Monte Carlo data is useful for purposes of calculating the detector acceptance, as well as understanding of the underlying physics. In the absence of an easily calculable theory of hadronization in e^+e^- annihilation, these phenomenological models have assumed some of the role traditionally played by theory; they have become something to compare with experimental measurements.

4.1   Analysis Code Overview

Most of the Mark II data was analyzed in two stages. The first stage, Pass 1, provided a 'rough cut' of the data, allowing a quick look at both detector performance and basic physics issues. However, its main purpose was to find a set of calibration constants. These constants included parameters that could vary with time, such as gas drift velocity in the drift chamber and preamplifier gains. These changes could result from diverse reasons, ranging from changes in the drift chamber gas composition, radiation induced effects in the TOF scintillator, daily and seasonal temperature variation, and general detector aging. The constants were found by parameterizing the data, with the desired constants as free parameters.

The second stage, Pass 2, was similar to the first stage, except that the various calibration constants found were incorporated into the analysis to improve the accuracy of the found quantities. Towards the end of the run, the two stages were telescoped into one pass. The constants found from earlier data were used

in succeeding runs. This did not affect the quality of the data greatly, since the constants were drifting relatively slowly.

The Pass 1 and Pass 2 programs included subroutines to analyze the different types of data. For most of the running, the first step was a quick filter to remove background events, such as beam gas interactions. Although it affected some analyses, it had no effect on the hadronic event selection used here. For physics events the first, and most CPU intensive step, was to analyze the drift chamber data to find charged particle tracks. Next, the vertex chamber data was linked to the drift chamber data, and the tracks were fit to a helix. These processes will be discussed in detail in the next section.

Next, the time-of-flight data was added. Charged particle tracks were projected into the time-of-flight system. The counter that was expected to be hit, and the nearby counters were searched for hits. These hits were assigned to the nearest track. Timing corrections were made, adjusting the timing for expected variations depending on the phototube pulse height, track position in z, and time of flight calibration constants (which varied, depending on the temperature, etc.).

Next, the liquid argon calorimeter information was added. It was handled differently for charged particles and neutral energy clusters. All charged particle tracks were projected into the liquid argon. Those strips which the trajectory crossed, and those nearby were searched for energy deposition. The energy deposition was added, and associated with the charged track. Most charged particles passed through the liquid argon losing little energy (typically a few hundred MeV), but electrons and positrons generally produced a large electromagnetic shower, losing most or all of their energy. By comparing the momentum measured in the drift chamber with the energy deposited in the liquid argon, it was possible to differentiate between electrons and hadrons. An algorithm separated electrons and non-electrons by looking at the pattern of energy deposition. This algorithm will be described in Section 4.3.

For neutral particles, the process was somewhat different, since there was no starting trajectory. Neutral particles manifested themselves as clusters of energy, deposited in several layers. For photons hitting the fiducial volume, the efficiency was about 40% at 200 MeV, rising to almost 100% above 500 MeV. At the lower energies, there was a significant background from fake photons. Most of these fake photons were the results of hadrons interacting in the calorimeter. When a hadron interacted and showered, it deposited energy over a large area, and the edges of its shower sometimes appeared as a fake photon. Many of these were removed by eliminating photon candidates that were too near a charged track.

The muon system was searched in much the same way as the liquid argon. Charged particle trajectories were projected into the muon system. The width of the search region depended on the expected amount of multiple scattering. Usually, the particle was allowed to miss the expected trajectory by up to twice the expected multiple scattering. For most analyses, including the work presented here, candidate muons were required to register hits in all four layers of the muon system.

The endcaps were incorporated into the offline software in a similar manner to the liquid argon. Charged particles were projected into it. The situation was complicated by the fact that tracks hitting the endcaps did not traverse the entire drift chamber, and so were likely to be poorly measured. Then, energy clusters were searched for, as with the liquid argon.

The SAT system was handled somewhat differently, because of its dual function. SAT Bhabha triggers were simply counted, without being analyzed. This count was used to find the luminosity. For other triggers, the SAT system data was analyzed normally. The drift chamber was searched for tracks coming from the origin, and the calorimeters were searched for energy deposits.

All of the information from the systems was then combined into a single data structure, a linked list called the tracklist, that contained all of the quantities

necessary for most physics analysis. This integrated system made it easy to do quick searches.

The next section will consider the drift chamber information in greater detail.

4.2 Charged Particle Tracking

The first step in charged particle tracking is pattern recognition, finding the tracks. The Mark II used two different pattern recognition programs: PTRAKR and SUPTRKR.

These track finding programs searched for patterns in the drift chambers, sets of hits which lined up to form a helical track candidate. A set of hits was selected and fit to a piecewise helical arc. During the fitting hits could be dropped from the fit on the basis of a bad χ^2. New hits could also be added. Tracks with very bad overall χ^2 were also dropped, although moderately bad tracks were retained, and were generally dropped according to criteria established during the physics analysis. Tracks were fit to a six variable helix:

- ϕ, the track azimuthal angle at its closest approach to the origin.

- κ, the helix curvature, proportional to $1/p_{xy}$.

- $\tan \lambda$, the dip angle. $\lambda = \pi/2 - \theta$. θ is the angle between the track and the beampipe, as shown in Fig. 3.3.

- x, y, z, the coordinates of a point on the track.

These six variables reduce to five independent variables because a helix has one dimension of its own. In the Mark II code, x, y, and z are mapped into ξ and η, which give the track position at a given plane, say at $z = 0$.

When the vertex chamber was installed, a sixth independent variable was added to this ensemble, to account for multiple scattering in the interface between the drift and vertex chambers.

4.2.1 PTRAKR

The earliest tracking programs were PTRAKR and TLTRKR, which were used together[52] TLTRKR was a simple, fast trackfinder. It used the information from the hardware track finder in the trigger as a starting point. Taking these as initial guesses for tracks, it then added and subtracted DAZMs (drift chamber hits) to get good tracks. TLTRKR was mainly used to do initial event filtering, and make things easier for PTRAKR by sorting out some of the confusion. It was roughly 85% efficient.

PTRAKR used an algorithm similar to that used by the charged particle trigger and TLTRKR. It began by sorting unused DAZMs, classifying them by the ϕ of the hit wire. Since it could look at the drift times, the roads that it used were much narrower than those used by the hardware trigger. Left-right ambiguities were handled by preserving both solutions until one could be eliminated. Stereo wires were handled by expanding the parameter space to include stereo variables.

PTRAKR made several passes through the list of DAZMs. In normal processing, TLTRKR was the first pass. Succeeding passes use PTRAKRs algorithms, but with progressively looser χ^2 cuts to find poorer and poorer tracks. For the analyses described here, PTRAKR had one major flaw. The roads that it used were presumed to come from the origin. Tracks that did not project back to the origin will have a higher χ^2 for their track finding cuts. So, tracks coming from the origin are found preferentially and the tracking efficiency is reduced for tracks from long-lived neutral particles, such as K_s and Λ.

4.2.2 SUPTRKR

When the Mark II drift chamber began to suffer high voltage breakdown and the voltages were lowered, resulting in a loss of efficiency, it was found that the PTRAKR tracking efficiency was reduced, even for isolated tracks.

In an attempt to avoid this problem, Mike Levi wrote a tracking progrem, SUPTRKR , based on a different algorithm. SUPTRKR worked by a binary se.rch procedure.

SUPTRKR worked in a five-dimensional space of all possible tracks. The dimensions corresponded to the five tracking variables. It began by picking an initial DAZM seed to provide a starting ϕ for the search. It then looped over all of the other DAZMs, seeing if they could fit any possible track. At this stage, the only DAZMs that were eliminated were those more than 90° away in ϕ from the seed. It then counted the DAZMs found. If there were too many, SUPTRKR subdivided this five-space into subspaces. Each DAZM was tested to see which subspaces it fit. The subspace that could accommodate the most DAZMS was selected and further subdivided. This division process continued for a maximum of seven divisions. As the subspaces became smaller, the number of DAZMs that could fit possible tracks contained in the subspace decreased. Eventually, the subspaces held few enough DAZMs that it was likely to encompass only a single track.

When the number of hits in a subspace reached this level, the hits are tested as a track. Since the drift chamber efficiency is fairly high, the hits were likely to come from a single track, although there could be some extra hits in the subspace. Individual hits which did not fit the candidate track were dropped until an acceptable track could be found.

After each track candidate was found, its DAZMs were eliminated from consideration, and the process continued using another seed.

4.2.3   Track Fitting

Once a track was found, with either PTRAKR or SUPTRKR, it had to be fitted to obtain the best possible resolution. The track was fit to a piecewise helix. The helix was fit in pieces because the radius of curvature changed as the particle moved along the trajectory. It lost energy because of dE/dx and it could scatter

from multiple scattering, both at the drift chamber/vertex chamber interface, and in the chambers themselves. Also, the magnetic field varied slightly in the chamber volume.

The fitting began near the origin and worked outward in small steps, where small is defined in reference to the curvature of the track. For poorly constrained tracks with relatively few DAZMs, the fit might be to a single piece. Each piece was fitted to its DAZMs, using a least squares fit. The pieces were combined to form a single track, taking into account expected dE/dx momentum loss, and changes in direction due to multiple scattering. The momentum at the beginning of the drift chamber was found, as was the error matrix. The track was projected back to the origin to find the point of closest approach. The errors on all of these quantities were calculated for later use in vertex finding or constrained fitting.

4.3   Electron Identification

Because the Mark II liquid argon was finely segmented, electrons were identified with high efficiency while hadrons were rejected[53] The identification algorithm began by projecting each charged track through the liquid argon. In each layer, the energy deposited on strips near the target track was measured. The width of the search region was given by

$$W_{tot} = W_{Shower} + W_{gang} * |\tan(\delta)|$$

where W_{Shower} is the width of a typical electromagnetic shower, taken to be 2.9 cm. W_{gang} is the geometric width of the shower due to the geometry and the ganging scheme used, while δ is the angle between the extrapolated track and the normal to the module. W_{gang} was 2.9 cm for the F1 and F2 layers, 5.7 cm for the T1 layer, and 8.1 cm for the U layer.

The total energy on strips located within the search region (within W_{tot} of the projected track) are added. For each track, a cut variable called TEST1 is

calculated. TEST1 represents the minimum energy deposition at any layer in the front part of the liquid argon. Mathematically, it is the minimum of:

$$\frac{E_{F1} + E_{F2}}{\alpha_F \cdot p}, \quad \frac{E_{T1}}{\alpha_T \cdot p}, \quad \frac{E_U}{\alpha_U \cdot p}, \quad \frac{E_{F1} + E_{F2} + E_{T1} + E_U}{\alpha_{Fr} \cdot p}.$$

The α parameters are chosen by studying the expected energy deposition in each layer for an electron. They are selected so that most electrons will satisfy these requirements. They are 0.14 for the F layers, 0.10 for the T1 and U layers. α_{Fr}, the expected deposition in the front part of the calorimeter is 0.5 for $p<$ 4 GeV/c and 0.4 for $p>$ 4 GeV/c.

As TEST1 increases, the probability that the particle is an electron increases. *The exact cut value used depends on the desired purity of the sample.* For this work, if TEST1 was greater than 1.1, the particle was considered an electron. The electron acceptance and hadron rejection depend on this cut and the general track .nvironment. In a dense jet, where hadronic showers may overlap many tracks, the hadron misidentification may increase. For isolated tracks with a few GeV/c momentum, the electron identification efficiency for tracks in the fiducial volume was about 90%, while the pion misidentification probability was about 0.4%.

One difficulty in this analysis is obtaining a clean sample of hadrons. All of the studies of hadron misidentification have used pions, either from K_s or τ decays. In particular, no studies have been done of the probability of antiproton annihilation mimicking an electron. This was a special worry in the measurement of Λ_c^+ background, since baryons are produced in pairs with antibaryons. This effect is a systematic error for the Λ_c^+ semileptonic decay analysis.

4.4 Monte Carlo Programs

Modern high energy physics detectors and analysis software are so complicated that it is virtually impossible to understand their performance analytically. Instead, to gain an understanding of detector acceptance, 'fake data', known as Monte Carlo data, is generated. This data is then analyzed

using standard analysis programs. The results of this analysis are compared with the input to the Monte Carlo program, providing a good understanding of the detector and analysis efficiency.

Monte Carlo programs divide easily into two parts: the event generator and the detector simulation. Most Monte Carlo generator programs have grown so complex that they are now considered a research interest in their own right, and several good packages are available. Several different programs were used in this work, and they will be described here. The detector simulation, however, is detector specific, and usually written by the physicists responsible for the particular subsystems.[54]

4.4.1 BQCD

One early Monte Carlo generator used by the Mark II collaboration was known as BQCD. It followed the lines of the Feynman-Field parameterization with the Ali prescription for gluon jets and energy-momentum conservation. In this form, it was known as QCDJET. Later, it was modified to allow light (uds) spin 1/2 baryons, to be produced via spin 0 diquarks. It used the standard five quark flavors, but handled heavy mesons in a somewhat simple manner. The standard parameters adopted for this model and used unless otherwise specified are given in Table 4.1.

4.4.2 The Lund Model

A computer program version of the Lund model, described in the theory section is also available. It is essentially[55] a Fortran version of the model described in the theory section. The main difference is that the computationally intractable noniterative process described in the model is replaced by a mathematically equivalent but easily computable iterative procedure. The standard parameters used are found in Table 4.2.

One difficulty with Monte Carlo methods is handling particle decays. For well-understood particles, it is easy to include routines to decay the particles according

Parameter	Value	Description
Λ_{QCD}	0.35 GeV	QCD Scale parameter
P_s	0.20	Probability to pull a strange quark from the sea
σ_{perp}	0.30 GeV/c	RMS perpendicular momentum for quarks and diquarks
P_{qq}	0.11	Probability to pull a diquark from the sea
P_V	0.33	Light quark vector:pseudoscalar meson ratio
N	2.00	Light quark, diquark splitting function N
A	0.70	Light quark, diquark splitting function A
ϵ_H	0.50	Heavy quark fragmentation exponent
$\sin^2(\theta_W)$	0.23	Weinberg angle parameter

Table 4.1. Parameters for the BQCD Monte Carlo.

to the measured branching ratios. However, for particles with unknown or poorly measured branching ratios, this cannot be done. Instead, the Lund model handles these particles by decaying them into two strings. For example, a Ξ_c^+ can decay to a u jet connected to a $\bar{d}$ jet and an s jet connected to a su diquark jet. For a baryon to fragment completely into jets, at least one of the jets must be a diquark jet. This scheme is not very accurate; it has been tried with the D^0, for example, and does not work well. Still, it is the best that can be done.

4.4.3   The Webber Model

The third event generator used here is an implementation of the Webber cluster model described earlier. It is not quite a transcription of the model into Fortran; there are still a few loose ends. One major one is the question of heavy quarks. Bottom quarks are heavier than the heaviest allowable cluster, causing problems for the decay routines. In the Webber code, bottom quarks decay *before*

Parameter	Value	Description
Λ_{QCD}	0.50 GeV	QCD scale parameter
P_s	0.30	Probability to pull a strange quark from the sea
σ_{perp}	0.30 GeV/c	RMS perpendicular momentum
		for quarks and diquarks
P_{qq}	0.09	Probability to pull a diquark from the sea
P_{qs}	0.35	Extra suppression factor for s containing diquarks
P_{qq}^1	0.05	Extra suppression factor for spin 1 diquarks
$P_{3/2}^1$	1.00	Extra suppression factor for spin 3/2 baryons
Popcorn	0.50	Probability to produce a meson inside
		a baryon antibaryon pair
P_V	0.50	u, d quark vector:pseudoscalar meson ratio
P_{sV}	0.50	s quark vector:pseudoscalar meson ratio
P_{hV}	0.75	b, c quark vector:pseudoscalar meson ratio
A	1.00	Fragmentation function A
B	0.70	Fragmentation function B
$\sin^2(\theta_W)$	0.23	Weinberg angle parameter

Table 4.2. Parameters used in the Lund Monte Carlo.

clustering; the decay products are then used in the clusters. Since bottom quarks have a fairly long (1 psec) lifetime, this is a definite drawback to the model.

Otherwise, the cluster model was followed as faithfully as possible. Although the program has options for suppressing certain types of production (strange quark, diquark) more than that given by the clustering formulation, these options were not used. The parameters used in the model are given in Table 4.3.

In the latest version (4.1) of the Webber Monte Carlo, the light quark masses listed here are not r   'ree parameters; they are calculated from current

Parameter	Value	Description
Λ_{QCD}	350 MeV	QCD scale parameter
P_{perp}	350 MeV/c	Quark, diquark RMS perpendicular momentum
CLMAX	110 MeV/c^2	Maximum cluster mass
QG	750 MeV/c^2	Gluon virtual mass cutoff
M_u	4 MeV/c^2	Up quark mass
M_d	8 MeV/c^2	Down quark mass
M_s	150 MeV/c^2	Strange quark mass
M_Z	94.0 GeV/c^2	Z^0 mass
Γ_Z	2.9 GeV/c^2	Z^0 width
M_W	83.0 GeV/c^2	W$^\pm$ mass

Table 4.3. Parameters used in the Webber Monte Carlo.

algebra. Before being used, they are converted to constituent masses by adding an interaction mass, taken to be the same as the gluon virtual mass cutoff[56] This gluon virtual mass is a free parameter in the model. This procedure is considerably changed from earlier versions of the Monte Carlo, and may change in the future.

4.4.4 Detector Simulation

The output of all of these event generators is similar: a list of particle descriptions. These lists give the particle types, charges, four vectors, and describe their decays. One difficult problem is the question of long-lived particles. These particles may live long enough to interact with the detector before decaying. This was handled by saving the distance that the particle traveled before decaying. When the tracks were fed into the detector simulation, they were bent as appropriate for the magnetic field, and projected the appropriate distance into the detector, before being allowed to decay.

The detector simulation handled tracks one at a time. The tracks were followed from their origin outward, detector subsystem by subsystem. At each step, their effect on the detector was recorded. After all of the particles were passed through the detector, their effects were added, and conflicts were resolved. For example, since the drift chamber lacked multihit electronics, only the hit with the shortest drift time for a given wire was saved.

The process begins with the vertex that created the particle. Tracks are projected outward in steps. At each step, the track is randomly multiple scattered, by an amount depending on the material traversed. Electrons are given a probability to bremsstrahlung. Hadrons may undergo nuclear interactions and be absorbed.

In the drift chamber, the particles distance of closest approach to each wire is calculated, and a drift time generated with a random error depending on the measured resolution. For the work presented here, the resolution used was representative of the times when the drift chamber was working well; later, corrections were made for the reduced voltage period.

When tracks reached the time of flight counters, their flight times and pulse height distributions were calculated. Errors, generated randomly according to the measured distributions, were added to produce the final data.

For the liquid argon calorimeter, different methods were used for electrons and photons, and for hadrons. Electromagnetic showers were handled one of two ways. For sensitive studies, they could be simulated in gory detail using the EGS Monte Carlo[57] However, for most applications, this was too time consuming. Instead, a library of electromagnetic showers was created. The library included a variety of energies and angles of incidence. Showers were selected from the library at random. The showers were scaled to match the energy and incidence angle of the incoming particle.

Several options were also available to simulate hadronic interactions. The simplest option was to simply treat all hadrons as minimum ionizing particles,

depositing a few hundred MeV in the calorimeter. Since hadrons were mostly considered a background in the calorimeter, this was often adequate. The second option was to use a shower library, in much the same way as was done with electromagnetic showers. Two different libraries were available, one based on test beam data, and the other on a sample of pions from τ decays. Both of these sources suffered in that they did not include examples of antiproton annihilation.

Muons that reached the muon system were treated in much the same manner as in the drift chamber. They were projected through the muon system in steps, allowing for multiple scattering and energy loss. Hits were generated for each layer reached. Hadrons were treated similarly, except that at each step, they had a probability of being absorbed. The probability depended on their energy and the material thickness, and was found by interpolation from a lookup table. The lookup tables were originally generated using HETC[58]

The simulations described here are tested by comparing various parameters with the data. For example, drift chamber resolution can be checked by comparing with a sample of Bhabha events. In many cases, the simulated detector works slightly better than the real one. For example, drift chamber tracking efficiency is slightly better in the Monte Carlo. In general, however, these effects are small, and can easily be corrected.

Chapter 5.   Strange Baryon Production

This chapter will discuss the measurement of the production rate of strange baryons. It will begin with a discussion of a previous Mark II measurement of Λ production. This is followed by new results on Ξ^-, Ξ^{*0}, and Ω^- production. In these chapters, every time that a particle or reaction is mentioned, it should be assumed to include the antiparticle or conjugate reaction as well, unless otherwise specified.

Because most of the theories of baryon production include a number of adjustable parameters, to adequately test them, it is necessary to study a variety of different baryons to adequately test the models. Single particle production rates merely pin down the Monte Carlo parameters and provide mild tests of reasonableness. The three measurements presented here test these models for highly strange baryons. Combined with an earlier Mark II result on Λ production, and results from other experiments, they can provide a fairly comprehensive test of the various baryon production models.

This chapter begins by discussing some factors common to all of the analyses: data and event selection, and track selection. It then moves on to consider the three individual analyses.

5.1   Data Selection, Event Selection, and Luminosity

Since relatively clean Ξ^- and Ω^- can be found via geometric cuts, and since they are both fairly rare, it is important to use the largest data sample possible, even if the momentum resolution is less than optimal. For these measurements, the entire Mark II/PEP5 data set with vertex chamber data was used.

The luminosity was measured with small angle Bhabha scattering, and checked with large angle Bhabha scattering[59] The two luminosity measurements track each other within 1%. The absolute value from the wide angle Bhabhas was used as a scale[60] At this accuracy level, one must be careful about occasional

missing runs, etc. Therefore, the luminosity uncertainty will be taken to be 2% here.

The analyses were done on the entire 207 pb^{-1} of data taken after the vertex chamber was installed. SUPTRKR was used exclusively, because it had a higher efficiency for tracks that do not come from the origin. For the Ξ^- analysis described below, it had a 50% higher efficiency than PTRAKR.

From this data, hadronic events were selected with a very simple set of cuts. Because strange baryon production from nonhadronic sources is expected to be very limited, a very loose set of cuts can be used without excessive contamination.

The cuts used for hadronic event selection were those used to make the Mark II data summary tapes (DST's). Events were required to have:

1. At least four tracks.

2. At least 4 GeV of total momentum in the charged tracks.

3. At least 8 GeV of total (charged plus neutral) energy.

After all cuts, the Ξ^- and Ω^- candidate events and background events were hand-scanned, and no evidence for contamination from sources other than $e^+e^- \rightarrow$ hadrons was seen.

5.2   Track Selection

Charged particle tracks used in strange baryon reconstruction were required to pass certain track quality cuts. These cuts were designed to insure that selected tracks were real, and not artifacts of the trackfinding programs, and that they were well measured.

The tracks used were required to have:

1. A polar angle with respect to the beam, θ, that satisfies $|\cos(\theta)| < 0.8$. This insures that the track is within the drift chamber volume.

2. At least nine drift chamber hits (DAZMs) used in the fit. This compares with 23 possible DAZMS from a track which hit every layer in the drift and vertex chambers.

Since a track has five free parameters, this is a minimum of four constraints.

3. A χ^2 per degree of freedom less than 12.

4. A momentum transverse to the beam, $p_{xy} > 70$ MeV/c. This cut is somewhat lower than is conventional because of the kinematics of Ξ^- and Ω^- decay, as will be discussed below.

Finally, e^+e^- pairs from converted photons and Dalitz π^0 decays ($\pi^0 \to e^+e^-\gamma$) were eliminated, using an algorithm developed by Mark Nelson[a]nd described below. All oppositely charged track pairs were subjected to this analysis. Tracks pairs which met the following criteria were considered to be e^+e^- pairs. Members of these pairs were not used in the analyses. Figure 5.1 shows the geometry used in the cuts. Pairs which met the following criteria were removed.

1. The absolute value of Δ_{xy}, the gap between the tracks in the x-y plane, at the point where the tracks are tangential, is less than 5 mm. This quantity can be either positive or negative.

2. RCOS, the cosine of the angle formed by the line between the tangency point and the interaction region, and the pair momentum vector, must be greater than -0.1. e^+e^- pairs should point away from the origin; this cut saves track pairs that point toward the origin.

3. For well-measured tracks, there is an additional cut which uses the available z information. If the difference in z coordinates of the two tracks at their closest approach to the origin, Δz_0, is less than 10 cm (indicating that the z information is likely to be good), then the difference between the two track dip angles, $\Delta\theta$, must be less than 0.12 radians.

This electron-positron pair removal is especially important to this analysis because tracks from γ conversions will miss the origin, and easily mimic tracks from strange baryon decay.
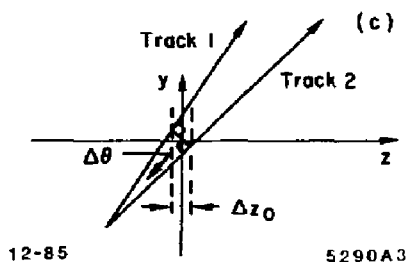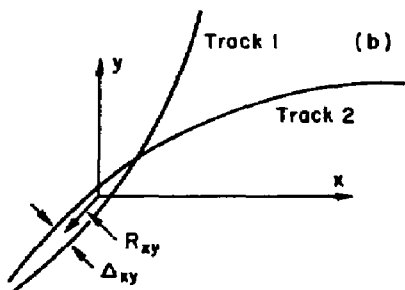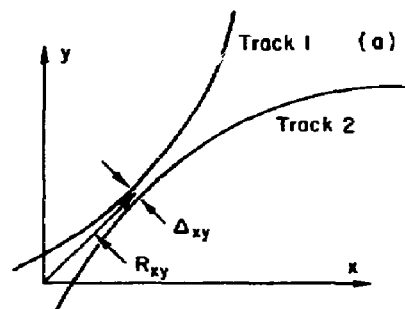
Figure 5.1. Pair finding algorithm geometry. RCOS is the cosine of the angle between R_{xy} and P_{xy} of the pair.

5.3 Λ Production

Although a measurement of Λ production is not part of this thesis, the Λ production rate is a convenient, well-measured, value to compare with other strange baryon production rates. Therefore, I will briefly describe an earlier Mark II measurement of Λ production[61]

Λ are the easiest strange baryon to detect, because of their simple decay topology, large branching ratio to pπ, and high production rate. Λ are easily detectable because their long lifetime (.26 nsec) allows them to travel a significant distance before they decay ($c\tau = 7.9$ cm). So, they can be found simply by searching for two oppositely charged tracks which both miss the origin by at least a few mm. By assigning the higher momentum track a proton mass, and the slower a pion mass, it is easy to test the hypothesis that they both came from a Λ decay that occurred at a single point.

The Λ analysis was done on the entire PEP5 vertex chamber sample. Because of the copious Λ production, systematic errors are larger than statistical errors; therefore many cuts can be chosen for the ease of understanding systematics or for background rejection, rather than to maximize efficiency. To maximize the Λ cleanliness, a complicated probability cut was used.

The final Λ signal was extremely clean, consisting of 1616 $\pm$ 46 over a background of 145 $\pm$ 16. This led to a production rate of 0.213 $\pm$ 0.012 $\pm$ 0.018 Λ per hadronic event. The Λ spectrum was consistent with the Lund model prediction.

5.4 Ξ^- Production

The Ξ^- was searched for through the reaction $\Xi^- \to \Lambda \pi^-$, $\Lambda \to p\pi^-$. Because the Ξ^- is relatively long lived (164 psec, $c\tau = 4.9$ cm), the use of separated vertexing techniques is important in studying Ξ^- decays. The basic geometry is illustrated in Fig. 5.2. Each potential Ξ^- decay is tested against this hypothesis.
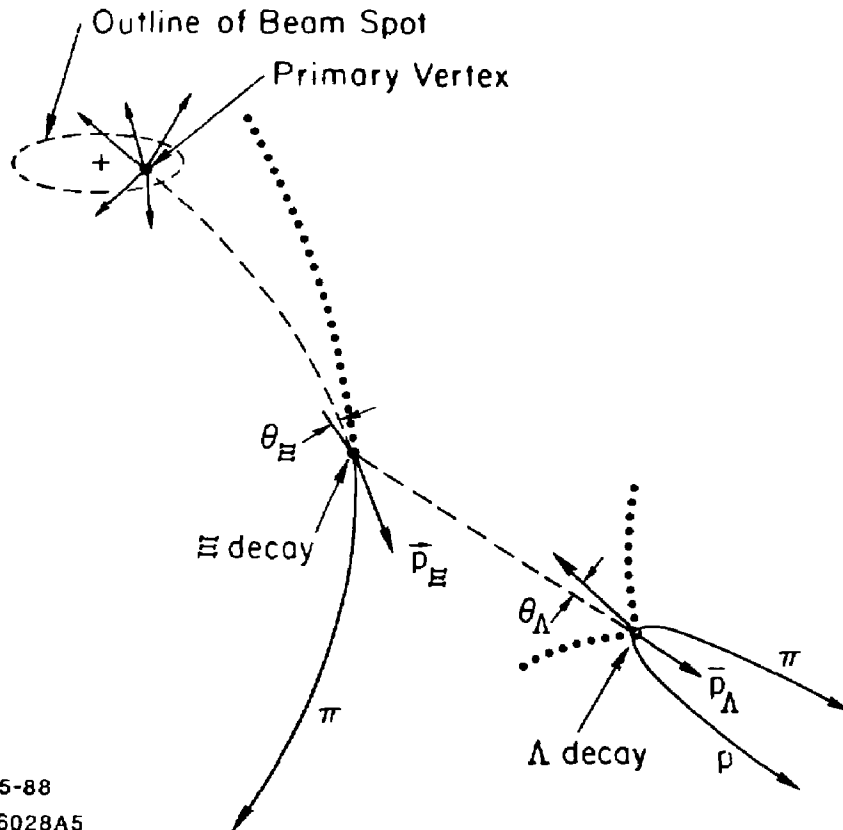
Figure 5.2. Geometry of Ξ^- decays. θ_Ξ and θ_Λ are the angles between the particle momentum vectors and the lines between the decay point and the center of the beam spot; they indicate how well the particles point back to the interaction region. The dotted lines are the projections of the charged tracks, showing that they miss the beam spot. The dashed lines are the reconstructed Λ and Ξ^- paths.

Besides the geometry, there is one additional aspect of Ξ^- decays which requires careful consideration: their low Q value and high mass differentials. In both Λ and Ξ^- decays, one particle carries off most of the mass because the Λ is much heavier than the π and the proton is much heavier than the π. Since

the mass difference between the Ξ^- and its decay daughters is small, little energy is released in the decay. This means that most of the daughter momentum will come from the original Ξ^- momentum, which will be divided up based on the daughter's mass. Therefore, the Λ will carry off most of the momentum, leaving the pion moving very slowly. For this reason, it is important to make the pion momenta cuts as low as possible. The cut chosen, $p_{xy} > 70$ MeV/c was set at the point where the tracking efficiency begins to fall significantly.

Because of its low magnetic field, the Mark II was very well suited to study Ξ^- decays. As was mentioned in the detector chapter, early in its running at PEP, the Mark II magnet coil developed a short circuit, which necessitated its running at half of its design field, or 2.25 kG. This field is far lower than fields found in similar detectors. For example, of the other detectors to present data on Ξ^- production in this energy range, the TPC detector had a 4 kG (later raised to 13.25 kG) field, TASSO had a 5 kG field, and HRS had a 17 kG field. The low Mark II magnetic field was significant because it allowed the Mark II to efficiently detect charged particles down to low momenta. At higher magnetic fields, low momentum charged particles curl up into spirals, creating multiple hits on drift chamber wires, and making tracking very difficult.

5.4.1   Ξ⁻ Selection

All of the appropriate sign combinations of tracks that passed the track quality cuts described above were tried in the Ξ^- analysis. First, the Λ from the Ξ^- decay was reconstructed. Because the Ξ^- is long lived, the Λ decay will not point back to the origin, so the cuts used in the above Λ analysis were not appropriate. Therefore, a separate set of cuts was developed.

The two charged particle tracks are treated as helices, then projected into circles in the x-y plane. The two intersections of the circles are found. Usually, only one of the intersections is inside the drift chamber; in other cases a simple arbitration scheme is used. The chosen intersection is considered the Λ vertex, and

the particle momenta at this point are calculated. The higher momentum particle in each pair is assumed to be the proton. This assignment is always correct for Λ with momenta over 250 MeV/c. Pairs which meet the following requirements are considered to be Λ candidates:

1. The distance from the reconstructed vertex to the interaction region in the x-y plane must be greater than 15 mm.

2. The π must have a distance of closest approach to the interaction region of greater than 2 mm.

3. At the x-y vertex, the two tracks must have a z difference of less than 6 cm.

4. The angle between the Λ momentum vector and the line between the reconstructed Λ decay point and the interaction region in the x-y plane must be less than 6°. For secondary Λ from Ξ^- decays, this angle is a few degrees, because the primary decay effectively puts a kink in the track.

5. Λ candidates with momenta less than 400 MeV/c are eliminated. Kinematics requires that all Λ from Ξ^- decays above 750 MeV/c (as required below) must have momenta above 400 MeV/c.

6. If good quality time-of-flight information is available for the proton track, the measured flight time is required to be within 720 psec (roughly 2 σ) of the predicted proton flight time.

These requirements are loose, and designed to maximize the yield of detected Λ from Ξ^- decay. The proton and π momenta are adjusted to compensate for dE/dx loss in the beam pipe. The two tracks are constrained in a full three-dimensional vertex fit. The χ^2 of the fit is required to be less than 15 for 1 degree of freedom. These cuts lead to the histogram shown in Fig. 5.3.

For Λ candidates with momenta p_Λ less than 2 GeV/c, the calculated mass is required to be within 5 MeV/c^2 of the actual Λ mass. For candidates with momenta more than 2 GeV/c, the calculated mass is required to satisfy

$$|M_\Lambda - 1115.6 \text{ MeV/c}^2| < 4 \text{ MeV/c}^2 + 0.5 * p_\Lambda(\text{GeV/c}) .$$
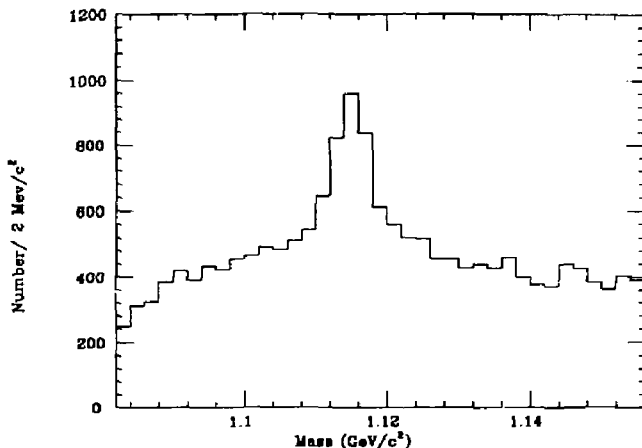
Figure 5.3. Λ mass peak for Ξ⁻ analysis.

The resulting signal is 1688 ± 76 Λ over a background of 2059 ± 45. The peak is centered at the Λ mass and has a full width at half maximum of 8 MeV/c².

Each Λ candidate is paired with every negatively charged track to make a Ξ⁻ candidate. A two-dimensional line-circle intersection is made (the uncharged Λ travels in a straight line) in the x-y plane. For each Ξ⁻ candidate, the distance in the x-y plane from the reconstructed decay point to the interaction region must be greater than 8 mm. At the x-y intersection point, the Λ and the π z coordinates must agree within 5 cm. Ξ⁻ candidates are required to have a momentum of at least 750 MeV/c. Θ_Ξ, the angle between the Ξ⁻ track, the line between the reconstructed Ξ⁻ vertex and the interaction region, and the Ξ⁻ momentum vector as projected back to the origin must be less than 5°. This angle is adjusted to compensate for the amount that the Ξ⁻ is bent in the magnetic field.

The masses of the resulting Λ π combinations are shown in Fig. 5.4, separately for right sign ($\Lambda\pi^-$, $\overline{\Lambda}\pi^+$) and wrong sign ($\Lambda\pi^+$, $\overline{\Lambda}\pi^-$) combinations. The narrow
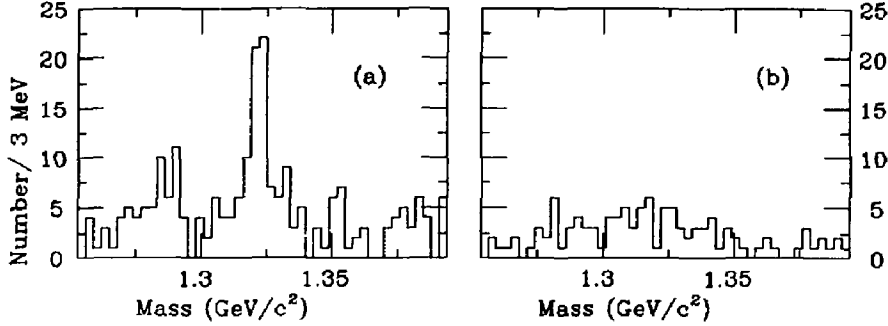
Figure 5.4. Invariant mass spectra for (a) $\Lambda\pi^-$, $\overline{\Lambda}\,\pi^+$ (b) $\Lambda\,\pi^+$, $\overline{\Lambda}\pi^-$.

peak in the right sign distribution is centered at the Ξ^- mass, with a width of roughly 6 MeV/c^2, consistent with the Monte Carlo predictions.

As with the Λ , the Ξ^- mass resolution is momentum dependent. For Ξ^- with momenta p less than 2 GeV/c, the mass is required to be within 6 MeV/c^2 of the actual Ξ^- mass. For Ξ^- with more than 2 GeV/c momenta, the mass cut is:

$$|M_\Xi - 1321.2 \text{ MeV}/c^2| < 5 \text{ MeV}/c^2 + 0.5 * p_\Xi(\text{GeV}/c) \; .$$

A typical event selected by these cuts is shown in Fig. 5.5.

For each Ξ^- candidate, two background regions are chosen with widths dependent on the momentum of the candidate. For a given Ξ^- momentum, the background regions are centered at 40 MeV/c^2 above and below the nominal Ξ^- mass and are each twice as wide as the signal region. The total background region is four times as wide as the signal region, in order to reduce the statistical error on the background.

These cuts leave a signal of 41 $\pm$ 8 Ξ^- + $\overline{\Xi}^+$ over a background of 14 $\pm$ 2 (statistical errors only). After subtraction of the roughly equal backgrounds, there are 29 Ξ^- and 12 $\overline{\Xi}^+$. We find no explanation for this apparent charge asymmetry;
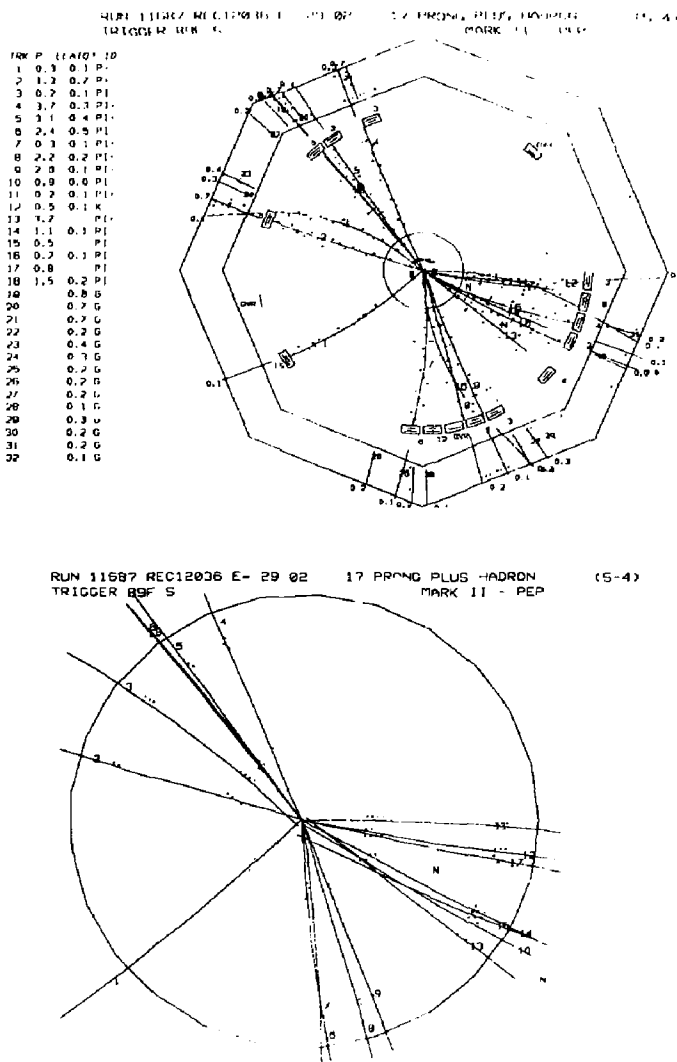
Figure 5.5. A Ξ⁻ event. Tracks 10 (proton) and 13 (pion) make up the Λ, which, together with track 11, form the Ξ⁻. The upper view shows the entire drift chamber and the liquid argon system. The tracks are the arcs, with DAZMs indicated by dots. The rectangular boxes are the time-of-flight system. The large octagonal structure is the liquid argon systems; F layer strip hits are indicated by dots. The lower figure shows a blowup of the vertex chamber.

the Λ and $\overline{\Lambda}$ signals are roughly equal. Based on a study of the positions of the primary vertices in these events, beam gas production of Ξ^- appears to be negligible. The Ξ^- and $\overline{\Xi}^+$ momentum spectra are similar. Interestingly, both TASSO[62] and HRS[63] observed the same 2:1 Ξ^- :$\overline{\Xi}^+$ ratio.

5.4.2 Detection Efficiency

The efficiency to detect Ξ^- decays was estimated using the BQCD Monte Carlo. Monte Carlo generated Ξ^- events were subjected to an identical set of cuts, including the DST cuts and e^+e^- pair rejection. Figure 5.6 shows the efficiency as a function of momentum. The efficiency is low at low momentum because the Ξ^- do not travel far enough to pass the R_{xy} cut, while at high momentum, it drops because some of the Λ travel far enough to be untrackable, and also because at high momentum the three tracks are close enough together to cause increased tracking confusion.
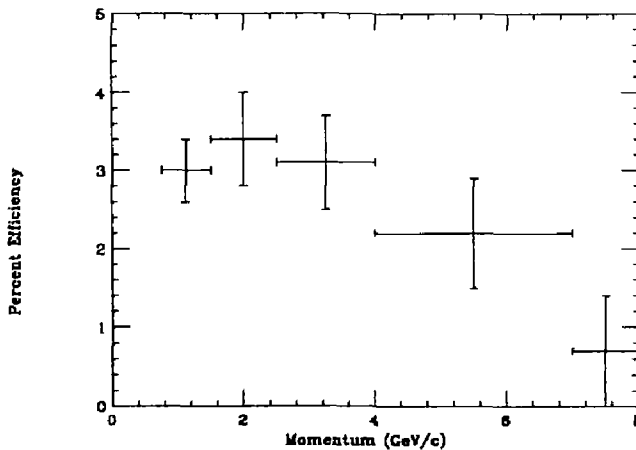
Figure 5.6. Ξ^- detection efficiency as a function of momentum.

The detector simulation accurately simulated the detector for the periods
when it was running well. In general, the quantities that were cut on (vertex
radii, distances of closest approach, momenta) seemed well reproduced by the
Monte Carlo.

Although BQCD produced twice as many Ξ^-'s as the data indicate, and
with a soft momentum spectrum (discussed below), in other respects, it was in
reasonable agreement with the data.

Table 5.1 shows the details of the efficiency and inclusive cross section
calculation. There are quarter integers in the data column because a quadruple
width, quarter weighted background region was used to increase statistics. A
similar subtraction was used for the Monte Carlo because tracking program
mistakes can cause real Ξ^- to appear in the background regions.

P(GeV/c)	N_{prod}	N_{det}	$\epsilon(\%)$	N_{data}	N_{corr}	N_{corr}/GeV/c
0–0.75	1467	0	0	0	—	—
0.75–1.5	1808	54	3.0 ± 0.4	7 ± 3.4	234 ± 116	312 ± 155
1.5–2.5	1400	48.5	3.4 ± 0.5	16.25 ± 4.8	474 ± 141	474 ± 141
2.5–4.0	930	29	3.1 ± 0.6	13.5 ± 4.2	433 ± 136	289 ± 91
4.0–7.0	578	12.75	2.2 ± 0.6	4 ± 2.3	182 ± 104	61 ± 35
0.75–7.0	4716	144.25	3.06 ± 0.25	40.75 ± 7.6	1323 ± 250	—

Table 5.1. Ξ^- detection efficiency and production. N_{prod} and N_{det} refer
to the Monte Carlo, and give ϵ, the efficiency. N_{data} is the number of
candidates in the data, while N_{corr} is the data after efficiency correction.
N_{corr}/GeV gives the number of Ξ^- per GeV/c of momentum.

As a check, the efficiency was also calculated using the Lund Monte Carlo.
In the 0.75–7.0 GeV range, the efficiency found was about 5% higher overall. The
difference was almost entirely in the 0.75–2.5 GeV range, where it is 50% higher.
However, due to the limited statistics, this is only 1.2 σ higher. One reason for the
difference may be that the Lund tapes were generated with a higher average $P_\perp$

than the BQCD tapes (400 MeV/c vs. 300 MeV/c). Here, $P_\perp$ is the momentum perpendicular to the thrust axis. For two-jet events, the thrust axis should be a good approximation to the string direction. Tracks with a high $P_\perp$ lie outside of jets, away from other tracks, where tracking efficiency is higher. Since tracking inefficiency causes a major Ξ^- signal loss, this effect can be significant even for small $P_\perp$ spectrum difference. For Λ, the $P_\perp$ spectrum agrees with BQCD better than with Lund.[64] For Ξ^-, the statistics are too limited to see a difference. To account for this, I assign a 10% systematic error for Monte Carlo uncertainties.

Figure 5.7 shows the efficiency corrected momentum spectrum, together with the BQCD and Lund predictions. The curves have been normalized to have the same area in the 0.75 to 7.0 GeV range. The Lund curve is a better fit to the data. Finding the total cross section requires an extrapolation to the regions of insensitivity, i.e., below 750 MeV and above 7 GeV. The statistics are insufficient to allow a fit to invariant phase space, forcing us to rely on the Monte Carlo. The Lund Monte Carlo was used instead of BQCD for two reasons. It fits the Ξ^- data better and does a good job of fitting Λ data. Second, it includes Ξ^- from heavier decays, which have a higher average momentum. In Lund, while only 30% of Ξ^- come from heavier baryon decays, they constitute 50 % of the Ξ^- above 4 GeV. In the Lund Monte Carlo, 8.5% of all Ξ^- are produced with P< 0.75 GeV, and 8.1% have P> 7.0 GeV, leaving 84% of them in the 0.75 to 7.0 GeV/c region, giving a correction factor of 1.166. For the error, we will take the difference between the BQCD and Lund predictions, a 21% difference, which introduces a 3.6% overall systematic error.

5.4.3   Total Cross Section

To convert this signal into a total cross section requires several corrections. The first correction concerns tracking efficiency. This correction is done in two steps. The first step matches the Monte Carlo to the period when the drift chamber was working well; the second accounts for the periods when the drift chamber was
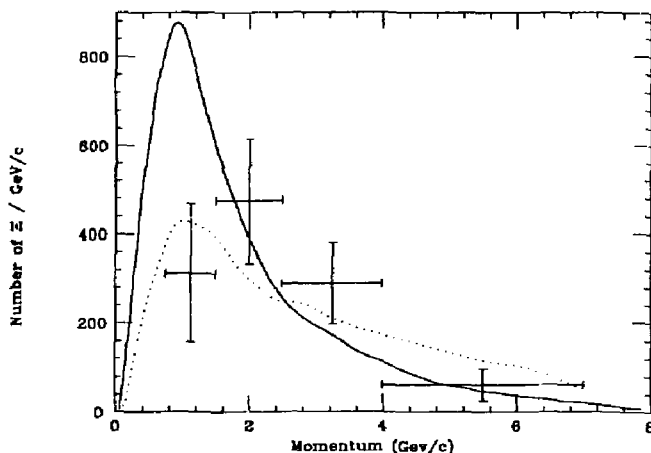
Figure 5.7. Efficiency Corrected Ξ⁻ momentum spectrum. The solid line is the BQCD Monte Carlo prediction, while the dotted line is the Lund Monte Carlo prediction.

running at reduced voltage. Heidi Schellman studied the relative tracking efficiency in the Monte Carlo and the data.[65] For the periods when the chamber was working well, she found that the Monte Carlo tracking efficiency was 1.5 % ± 1.5 % too high, with an overall tracking efficiency uncertainty of 3%. The Ξ⁻ decays into three charged tracks, so, this efficiency was cubed, giving a 5% ± 9% correction.

For the other periods, she found that the reduction in tracking efficiency was independent of momentum. She divided the running into five periods, and found that the efficiency during two of them was substantially reduced. Peter Rowson also studied the drift chamber problems and reached almost identical conclusions.[66] For the two bad periods, I cubed their per track relative efficiency to get the relative efficiency per Ξ⁻. These efficiencies are given in Table 5.2.

Including the previously mentioned spectrum extrapolation, the corrections and systematic errors are summarized in Table 5.3. The total efficiency correction is 1.33 ± 0.18. With it, there are 1760 ± 332 ± 178 Ξ⁻ in the data set. To

Period	Runs	ϵ/track	ϵ/Ξ^-	Lum (pb^{-1})	ϵ * Lum (pb^{-1})
VC82	8068–9099	1.00	1.00	21.6	21.6
BAD1	9339–10124	.89	.70	26.3	18.5
BAD2	10125–11107	.93	.80	49.2	39.3
OXYGEN + NEW	11108–13311	1.00	1.00	110.1	110.1
Total	8068–13311	—	—	207.2	189.5

Table 5.2. Drift chamber relative efficiency as a function of running period. ϵ is the relative efficiency. The different period labels refer to the different conditions. VC82 is the period just after the vertex chamber was added, when everything was working well. BAD1 and BAD2 are two periods after the deterioration started, when the drift chamber was at various lowered high voltages and efficiencies. OXYGEN refers to the period immediately after oxygen was added to the chamber and the voltages were raised. NEW refers to the final years running, when conditions were similar to that during the OXYGEN period. The numbers listed under the Runs column are used to identify specific data taking periods.

convert this number into a cross section, we must consider radiative corrections. The relevant formula is:

$$\sigma = \frac{N(\Xi_{det}) * A}{\int \mathcal{L} dt * B}$$

where Ξ_{det} includes the corrections for efficiency and spectrum extrapolation. A and B are factors which include the effects of radiative corrections. In a radiative event, some of the energy goes into the photon, so there is less energy left to create hadrons and, consequently, fewer hadrons. The factor B accounts for the increased cross section due to these radiative events. The cross section is usually quoted as R, the ratio of the hadronic event cross section to the muon pair cross section. To first order R is the sum of the squares of the quark charges, multiplied by three to account for the three colors. When QCD corrections are added, R rises to 3.9. If radiative corrections are included, R rises to 5.1. So, $B = 5.1 / 3.9$, to account for the increased cross section due to radiative events. Of course, the energy available

Item	Correction	Percent Error
Tracking	1.05	9
Monte Carlo Imperfections	1.0	10
Drift Chamber Inefficiency	1.09	5
Spectrum Extrapolation	1.166	3.6
Luminosity	1.0	5
Monte Carlo Statistics	1.0	8
Total	1.33	18

Table 5.3. Ξ^- rate corrections and systematic errors.

for hadron formation in these events is less than 29 GeV. The factor A accounts for this. It must be found by Monte Carlo. For Ξ^- at 29 GeV, it is 1.05.

Similarly,

$$N\left(\frac{\Xi}{\text{hadronic Event}}\right) = \frac{N(\Xi_{det}) * A}{\int \mathcal{L}dt * \sigma_{\mu\mu} * R_{measured}} .$$

These formulae give a total Ξ^- cross section of $3.2 \pm 1.3 \pm 0.7$ pb. This is equivalent to $0.017 \pm 0.004 \pm 0.003$ Ξ^- per hadronic event. This compares with the TPC collaboration measurement[67] of $0.020 \pm 0.008 \pm 0.004$, TASSOs[62] $0.026 \pm 0.008 \pm 0.009$ (at 36 GeV), and HRS[63] $0.016 \pm 0.004 \pm 0.004$.

This is in reasonable agreement with the Lund and UCLA models, which predict 0.014 and 0.019 Ξ^- per hadronic event, respectively. The Webber model predicts a higher rate, 0.037 Ξ^- per hadronic event.

The inclusive cross section for Ξ^- production versus x is shown in Fig. 5.8 where $x = 2E/E_{cm}$ and E is the baryon energy. The solid points show the data for Ξ^-. The solid line shows the predictions of the Lund model, and the dotted line shows the Webber model prediction, using the parameters from the previous chapter, which are in rough agreement with the data. The predictions of the

Webber cluster model are shown by the dotted lines. The Webber model predicts spectra similar to Lund and a comparable Λ production rate, but a higher Ξ^- production rate.
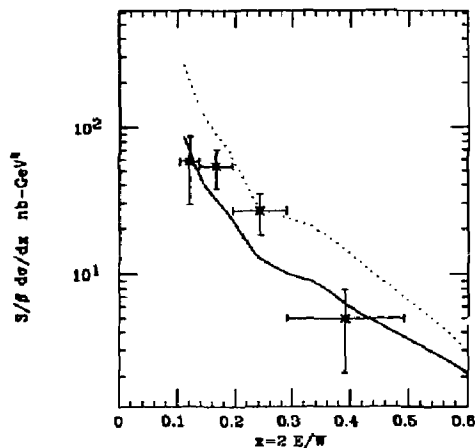
Figure 5.8. Inclusive cross section for $\Xi^- + \overline{\Xi}^+$. The solid points are the Ξ. The solid and dotted lines are the Lund string and Webber cluster model predictions, respectively.

The ratio of Ξ^- to Λ production is $0.08 \pm 0.02 \pm 0.02$. The Monte Carlo predictions are 0.07 for Lund and 0.15 for the Webber model. The measured Ξ^- to Λ ratio seems to require something more than the Webber cluster model phase space mass suppression.

5.5 Ξ^{*0} Production

An interesting application for the Ξ^- sample described in the previous section is a search for the decuplet Ξ^{*0} (1530), which decays via $\Xi^{*0} \to \Xi^- \pi^+$. The Ξ^- candidates are combined with all oppositely charged tracks (taken as π) which pass the track quality requirements. The Ξ^{*0} candidates are not required to meet

any other requirements. Figure 5.9 shows the result of the search. The histogram
is the data. The smooth curve shows the Lund Monte Carlo generated peak shape,
normalized to correspond to the 90% confidence level upper limit. The peak shape
is added to the measured background. The Monte Carlo includes the natural Ξ^{*0}
width (9 MeV/c^2 full width) and detector resolution. Based on the Monte Carlo, a
signal region from 1.522 to 1.542 GeV/c^2 is chosen. There are six candidates in the
signal region. Two background regions are chosen, one from 1.486 to 1.514 GeV/c^2
and the other from 1.550 to 1.598 GeV/c^2. They contain 21 events in a region four
times as wide as the signal region. The background regions have different widths
because the Ξ^{*0} mass is near the $\Xi^- \pi^+$ kinematic threshold.
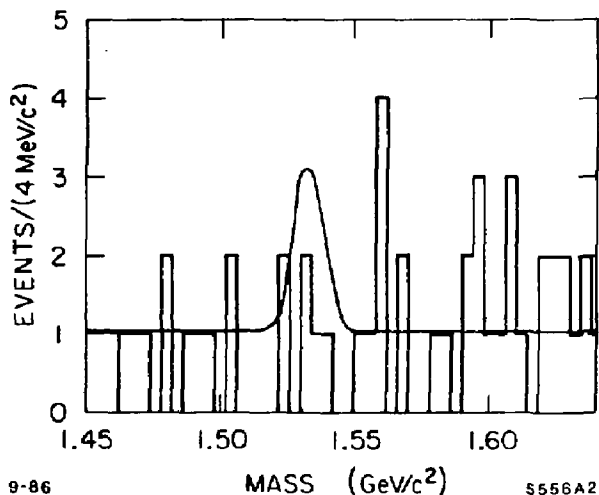
Figure 5.9. Invariant $\Xi^- \pi^+$, $\overline{\Xi}^+ \pi^-$ mass spectra. The histogram
represents the data, while the curve shows the Monte Carlo predicted
shape, normalized to 5.8 Ξ^{*0} (the 90% confidence level), added to the
measured background.

The small number of events necessitates the use of Poisson statistics for both
signal and background. To find an upper limit, the probability of the signal plus
background fluctuating to the measured signal region level times the probability

of the background fluctuating to the measured background level is calculated for a matrix of possible mean signal and background levels. The probabilities are summed over all of the background levels for each signal level, giving the relative probability of each possible mean signal level fluctuating to the observed signal level, i.e., the probability that it is the true mean signal level. From this, the 90% confidence level upper limit of less than 5.8 Ξ^{*0} detected is established.

The efficiency is found using the Lund Monte Carlo. Most of the systematic errors are similar to those encountered in the Ξ^- analysis. However, the Ξ^{*0} spectrum comes from the Monte Carlo. Since no signal is seen, there is no way to check it. Since the efficiency changes with momentum, the uncertainty in the spectrum is a major source of systematic error. From this, we find $N(\Xi^{*0})/N(\Xi^-)$ < 0.35 and $N(\Xi^{*0}) < 0.006$ Ξ^{*0} per hadronic event, both at a 90% confidence level. This agrees with the TASSO measurement of $\Xi^{*0}/\Xi^- < 0.5$ at a 95% confidence level[68] The Lund model agrees with the data, predicting 0.0028 Ξ^{*0} per hadronic event and $\Xi^{*0}/\Xi^- = 0.20$. However, the other two models predict too many Ξ^{*0}. The UCLA model comes fairly close, with 0.010 Ξ^{*0} per hadronic event, and $\Xi^{*0}/\Xi^- = 0.52$, while the cluster model predicts 0.019 Ξ^{*0} per hadronic event and $\Xi^{*0}/\Xi^- = 0.51$. Again, the Webber cluster phase space mass suppression seems inadequate to describe this data.

5.6 Ω^- Production

The search for Ω^- via the decay chain $\Omega^- \rightarrow \Lambda K^-$, $\Lambda \rightarrow p\pi^-$, in similar to the Ξ^- search. However, there decay kinematics are somewhat different, and Ω^- are expected to be rarer than Ξ^-, so the cuts are somewhat different. The Ω^- has a shorter lifetime than the Ξ^- (82 psec versus 164 psec), but a larger Q value. As with the Ξ^-, the first step is to select appropriate Λ candidates. The Λ selection for this analysis is somewhat different from the Λ selection for the Ξ^- analysis. These cuts are somewhat tighter, and lead to a somewhat cleaner Λ signal.

The initial vertex finding is the same as with the Λ from Ξ^-. All oppositely charged track pairs are vertexed. The higher momentum particle is considered to be the proton, as kinematics requires for all Λ with over 250 MeV/c momentum. The following cuts are applied:

1. The distance between the center of the interaction region and the Λ vertex must be at least 10 mm.

2. The angle between the Λ momentum vector and the line between the center of the interaction region and the Λ decay vertex must be less than 9°.

3. The π from the Λ decay must have a distance of closest approach to the center of the interaction region of at least 1 mm.

4. The proton must have a distance of closest approach to the center of the interaction region of at least .6 mm.

5. At the point of x-y intersection, the z distance between the proton and π tracks must be less than 4 cm.

6. The Λ must have a momentum of at least 500 MeV/c.

Here, a preliminary mass cut from 1.10 to 1.13 GeV/c^2 was made. Candidates passing this cut were subjected to dE/dx corrections, then constrained to come from a single point in space. For the fit, the χ^2 was required to be less than 10 for 1 degree of freedom.

These cuts left the mass histogram shown in Fig. 5.10. The momentum dependent Λ mass cut is retained from the Ξ^- analysis. It left a signal of 1460 $\pm$ 1088 over a background of 1088 $\pm$ 33. Again, the background is estimated from wings between two and three times the mass tolerance away from the nominal Λ mass.

These cuts lead to a significantly cleaner Λ signal than was used in the Ξ^- analysis. However, the signal is also smaller. The signal is cleaner because there are more cuts; the extra cleanliness is needed because it is harder to make effective cuts on Ω^-, because Ω^- have a shorter lifetime than Ξ^-.
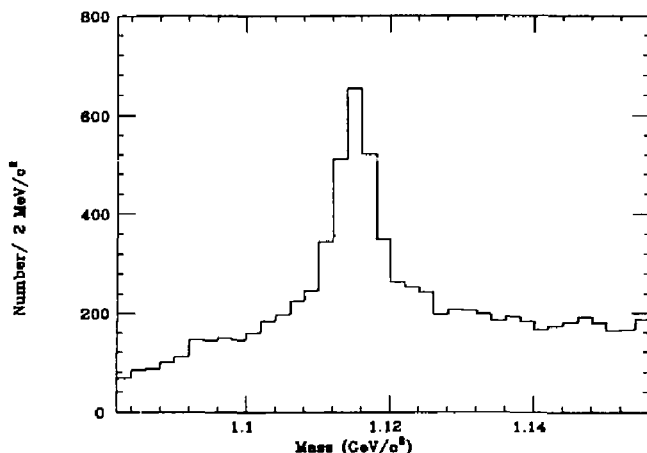
Figure 5.10. Λ with Ω^- cuts.

Next, a third particle is chosen in an attempt to make an Ω^- vertex. A line-circle vertex is made (the Λ is uncharged, and travels in a straight line). Again, if both intersection points are physically realizable, any on the far side of the interaction point are eliminated, after which the one with the better match in z is taken. Because the decay opening angles are generally small (10–20 degrees), errors in the position of the Λ vertex are multiplied in the Ω^- vertex position, making tight cuts on it costly. The cuts used are:

1. R_{xy}, the distance between the Ω^- decay point and the interaction region in the x-y plane, > 5 mm.

2. The K from the Ω^- has a distance of closest approach to the interaction point of at least 0.5 mm.

3. The Ω^- must have a momentum of at least 1 GeV/c.

4. The z distance between the Λ and the K at the point of x-y intersection is less than 2.5 cm.

5. The angle between the Ω^- momentum vector at the origin and the line between the Ω^- vertex and the origin must be less than $5°$. This angle is relatively insensitive to the errors in Ω^- vertexing. As with the Ξ^- analysis, the curvature of the Ω^- track before it decays is taken   to account.

6. Because the Ξ^- and Ω^- decays are similar kinematically, Ξ^- decays may mimic the rarer Ω^- decays. To avoid this problem, events which fit the hypothesis $\Xi^- \to \Lambda\pi^-$, with a Ξ^- mass within 10 MeV/c^2 of the nominal Ξ^- mass are rejected.

These cuts lead to the mass histograms shown in Fig. 5.11, separately for right and wrong sign combinations. There is a peak at the Ω^- mass for the right sign combinations. While there is no peak in the wrong sign combinations, the background is significantly higher. This effect is well reproduced in the Monte Carlo. Most of the difference comes from K_s decays where the two pions mimic the K^- and the π in the Ω^- decay. This can only happen for wrong sign decays. A smaller contribution comes from $\Lambda \bar{\Lambda}$ pairs where one of the Λ is reconstructed, and the other contributes a low momentum pion which is found as the K^- from the Ω^- .

Ω^- candidates are required to lie within 8 MeV/c^2 of the nominal Ω^- mass, between 1.664 and 1.680 GeV/c^2. The Ω^- FWHM from the Monte Carlo is about 8 MeV/c^2. Background regions are chosen from 1.616 to 1.648 GeV/c^2 and 1.696 to 1.728 GeV/c^2, a total of four times the width of the signal region. These cuts gave a signal of 14.0 ± 4.9 over a background of 9.0 ± 1.5. The signal is composed of 5.0 ± 3.3 Ω^- and 9.0 ± 3.7 $\overline{\Omega}^+$.

One check of the signal, and a guard against possible Ω^- - Ξ^- misidentification was to look at Manchester plots of the Ω^- and Ξ^- signals. These plots are useful for separating out different two body decays where there is no particle identification[69] and were first used to establish that Λ and K_s were two different particles. $P_\perp$, the perpendicular momentum of one decaying particle in the rest frame of the parent,
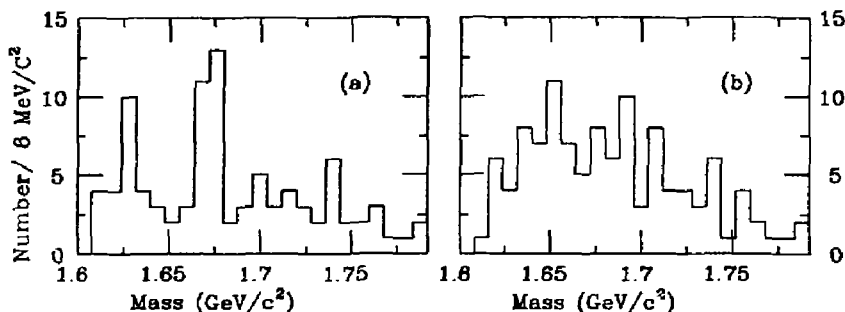
Figure 5.11. Λ K mass combinations for (a) right sign and (b) wrong sign combinations.

is plotted against α, where

$$\alpha = (p_1^2 - p_2^2)/P^2$$

where p_1 and p_2 are the momenta of the two decaying particles, while P is the momentum of the parent. For a given decay of a particle moving at a given velocity, the set of possible $P_\perp$ and α form an ellipse. The position and shape of the ellipse depend on the particle masses and the ellipse size depends on the parent velocity. For particle momenta in the range considered here, the ellipses form a narrow band. These parameters are plotted in Fig. 5.12 for the Ξ^- and Ω^- samples. For comparison, the results for Monte Carlo samples are also shown. The two types of decays are separated, except for a narrow region in the center. This region is cut from the Ω^- sample by the cut requiring that Ω^- not fit the Ξ^- hypothesis. The effects of this cut can be seen clearly in the Ω^- Monte Carlo; it is the empty spot on the ellipse around $\alpha \approx 0.6$. The two data plots match the Monte Carlo fairly well. The Ω^- data points have a larger spread than the Monte Carlo; this is because the Ω^- momentum spectrum is soft, and the Ω^- cover a
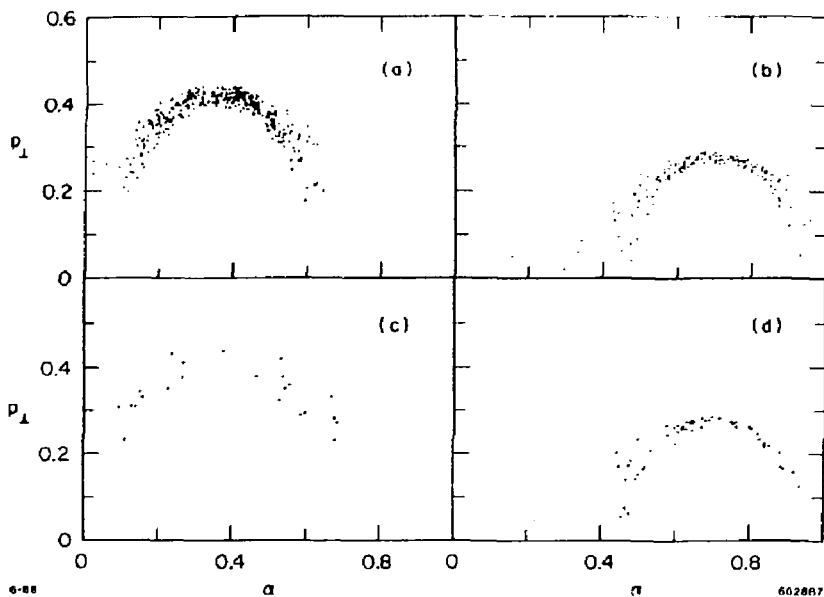
Figure 5.12. Manchester plots for Ω^- and Ξ^-. The horizontal axis is α, and the vertical is $P_\perp$. The plots show (a) Ω^- Monte Carlo, (b) Ξ^- Monte Carlo, (c) Ω^- sample, and (d) Ξ^- sample.

wider range of velocity than the data. The coverage is fairly even at larger $P_\perp$, indicating that the cuts do not squeeze the phase space.

The efficiency was estimated using Lund 6.1 Monte Carlo generated events which were then passed through a similar analysis program, including the DST cuts, SUPRTRKR, and e^+e^- pair rejection. Because Ω^- are so rare in the Lund Model, the Monte Carlo parameters were changed so that all produced diquarks were spin 1, composed of two strange quarks. This raised the Ω^- production rate to a usable level

Figure 5.13 shows the efficiency as a function of momentum, including the branching ratios. The efficiency is low at low momenta because all of the distance of closest approach and decay radius cuts discriminate against slower particles which decay closer to the origin.
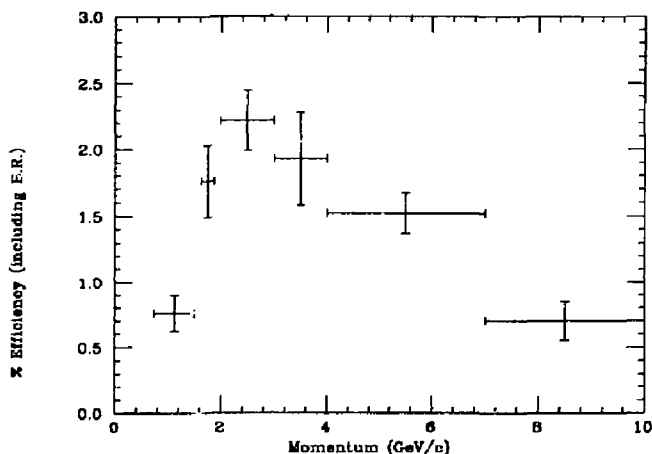
Figure 5.13. Efficiency for Ω^- detection as a function of momentum.

As with the Ξ^-, the Monte Carlo did a good job of reproducing the quantities that were cut on. Because of this, the efficiencies are very similar to those in the Ξ^- analysis, and the same uncertainties are used.

We now want to find the effici corrected momentum spectrum. One potential pitfall is if the Monte Carlo mo_.1entum spectrum does not match the data. Then, if the efficiency is changing rapidly as a function of momentum, the average efficiency in a bin, implicitly averaged over the Monte Carlo momentum spectrum, will not match the desired average point for the data. As we will see, this is a problem for the Ω^-; the Monte Carlo momentum spectrum is harder than the data. This problem is especially significant for low momentum Ω^-, where the efficiency is rising rapidly and where most of the signal occurs. To avoid biasing

the measurement, the momentum spectrum was divided into narrow bins, where the efficiency is relatively constant. This requires that a massive number of Monte Carlo Ω^- be generated to provide adequate statistics.[70] Table 5.4 shows the Monte Carlo efficiency calculation and compares it with the data.

P(GeV/c)	N_{prod}	N_{det}	$\epsilon(\%)$	N_{data}	N_{corr}	$N_{corr}/(GeV/c)$
0–0.75	1828	0	0	0	—	—
0.75–1.5	4009	30.75	$0.76 \pm .14$	6.5 ± 3.3	720 ± 429	960 ± 572
1.5–2.0	2502	44	$1.76 \pm .27$	3.0 ± 2.2	162 ± 125	324 ± 250
2.0–3.0	4046	89.75	$2.22 \pm .23$	4.25 ± 2.8	191 ± 127	191 ± 127
3.0–4.0	3027	58.5	$1.93 \pm .25$	2.75 ± 1.8	142 ± 193	142 ± 193
4.0–7.0	6272	95.5	$1.52 \pm .15$	-0.5 ± 1.6	-33 ± 105	-11 ± 35
7.0–14.5	3204	22.5	$.70 \pm .15$	0.0 ± 1.0	0 ± 142	0 ± 20
0.75–14.5	24888	341	$1.37 \pm .07$	14.75 ± 5.1	1182 ± 513	—

Table 5.4. Produced and Detected Ω^-. The column headings are the same as in Table 5.1. However, N_{corr} has been calculated using 250 MeV/c momentum bins for the efficiency, as described in the text; it is not simply N_{data}/ϵ.

Unfortunately, even with these small bins, there is a large error since so many of the Ω^- candidates fall in the 0.75 to 1.5 GeV/c momentum range. To reduce the error in this range, the efficiency was parameterized as a straight line, and the data efficiency correction was done by 250 MeV/c width bins. This approaches working on an event-by-event basis.

The efficiency corrected momentum spectrum is shown in Fig. 5.14. For comparison, the Lund (solid line) and Webber (dotted line) predictions are also shown. Both curves are normalized to the number of Ω^- in the 0.75 to 7.0 GeV region. Both Monte Carlos predict a harder spectrum than the data indicate. While the Lund model has enough adjustable parameters to produce a softer

spectrum, adjusting these parameters would lead to predictions for the spectra of other particles which would disagree with the data.
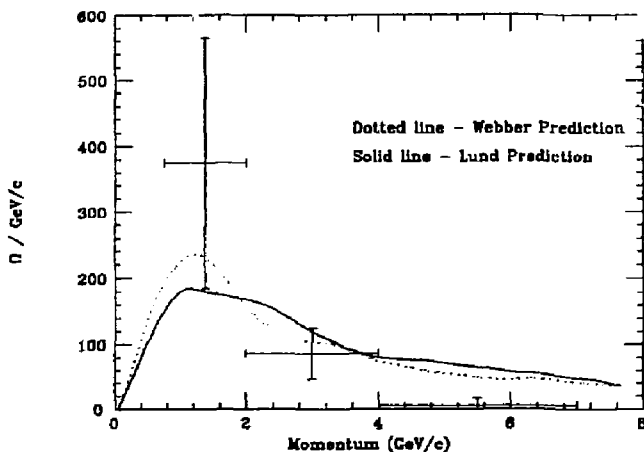
Figure 5.14. Efficiency corrected Ω^- momentum spectrum.

This analysis excluded the region below 0.75 GeV/c, since it is a region of low acceptance and high background. However, finding the total Ω^- cross section requires an extrapolation of Ω^- production into this region. Since the Monte Carlo fits the spectrum so poorly, a simple extrapolation was used. The Ω^- production rate should go to zero at zero momentum. Because the errors are so large, we can simply draw a straight line from 0 Ω^- at 0 GeV/c to 960 Ω^- per GeV/c at 1.125 GeV/c. This leads to an estimate of 215 Ω^- in the 0. to 0.75 GeV/c range. The Lund and Webber curves shown in Fig. 5.14 gave estimates of roughly 115 Ω^- and 142 Ω^- in this region, respectively. From this, we estimate that there are 179 $\pm$ 128 Ω^- in the 0 to 0.75 GeV/c region. Although this relative error is large, it contributes only 8% to the overall systematic error.

5.6.1 Ω Cross Section

Several corrections must be made to turn this into a total Ω^- cross section. Table 5.5 summarizes them. The tracking, Monte Carlo imperfections, drift chamber inefficiency, Monte Carlo statistics, and luminosity are as described in the previous section, while the spectrum extrapolation is described above.

Item	Correction	Percent Error
Tracking	1.05	9
Monte Carlo Imperfections	1.00	10
Drift Chamber Inefficiency	1.09	5
Spectrum Extrapolation	1.10	8
Luminosity	1.00	5
Monte Carlo Statistics	1.00	15
Total	1.26	21

Table 5.5. Ω^- cross section corrections and systematic errors.

The total efficiency correction is then 1.26 ± 0.21. Using this correcti_n and these systematic errors, there are $1489 \pm 636 \pm 248$ Ω^- in the data set. The radiative correction scheme described in the previous section was used. The total Ω^- cross section is then $5.8 \pm 2.5 \pm 1.4$ pb, equivalent to $0.014 \pm 0.006 \pm 0.004$ Ω^- per hadronic event.

This cross section agrees with the TPC measurement of $0.027 \pm 0.012 \pm 0.009$ Ω^- per hadronic event. However, TPC is only sensitive to the 2–10 GeV/c momentum range, while Mark II finds most of the Ω^- signal at lower momenta. In contrast, TPC says that their Ω^- signal is at a higher average momentum than their Ξ^- signal. The signal is comparable with the rough TASSO measurement[68] of 0.01 Ω^- per hadronic event.

It is, however, much higher than a measurement at lower energy. Recently, ARGUS made a high statistics measurement of Ω^- production around 10 GeV (a mixture of on and off resonance data)[71] finding 0.0012 ± 0.0005 Ω^- per hadronic event. Even considering the energy difference, this appears somewhat lower than our measurement would indicate.

It is also higher than all of the Monte Carlo predictions. The Lund model is way off, predicting 0.0004 Ω^- per hadronic event, only 3% of what the data indicate. While the Lund model has many parameters that can be changed to increase the rate, it is hard to see how they can be changed that much, and still give reasonable results elsewhere. This will be discussed more fully in the concluding chapter.

The UCLA model, freed from the Lund imposed spin 1 diquark suppression, does much better, predicting 0.002 Ω^- per hadronic event. However, it is still too low, as is the Webber prediction of 0.006 Ω^- per hadronic event.

5.7   Concluding Remarks

While a full discussion of the meaning of these results as a whole will be deferred until the concluding chapter, there are several remarks that should be made here.

The global event shapes of the Ξ^- and Ω^- candidate events were checked. The thrust, sphericity, triplicity, and charged multiplicity distributions of these events were all the same, within the large errors, of unselected hadronic events.

In this context, the softness of the Ω^- spectrum is puzzling. It may be compared with other baryons by plotting the invariant production cross section as a function of $z = E_{baryon}/E_{beam}$, as shown in Fig. 5.15. It does appear that the Ω^- spectrum is softer than the other baryons. One might expect that the same mechanism that produced soft Ω^- might affect the event shape. For example, one mechanism for increased baryon production is in gluon jets. Since this mechanism predicts that gluon jets also have a higher average multiplicity, and thus lower

average momentum, this could explain the soft Ω^- spectrum. These three-jet events should have a lower average thrust. Indeed, the Λ analysis showed that Λ containing events have a lower average thrust than average hadronic events. It is frustrating that the Ω^- sample is too small to decide this question.
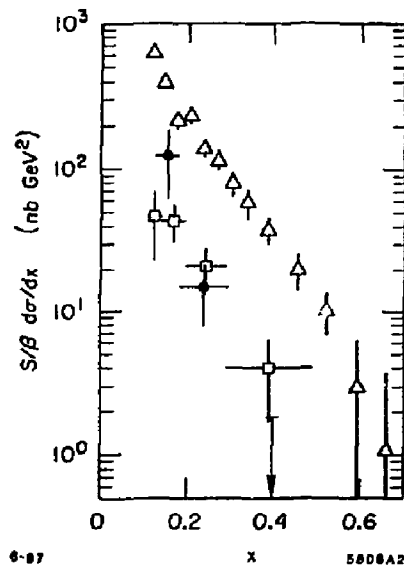
Figure 5.15. Invariant cross section for Λ, Ξ^-, and Ω^-. The triangles are Λ, the black circles are Ξ^-, and the open boxes are the Ω^- data.

A cursory search was made for signs of correlated baryon antibaryon production. No events appear twice in these samples; no examples containing more than one Ξ^- or $\overline{\Xi}^+$ or Ω^- or $\overline{\Omega}^+$ were found. This is not surprising considering the small efficiency and limited sample. A search for $\overline{\Lambda}$ associated with Ξ^- or Ω^- would be interesting, but probably fruitless for the same reason.

Chapter 6.   Charmed Baryons

In contrast to strange baryons, charmed baryons are very short lived. They cannot be found via separated vertex searches. Instead, other techniques must be used. Because charmed baryons are so rare, and because charmed baryon branching fractions into individual decay modes are only a few percent, simple kinematic cuts have not proven effective at PEP and PETRA energies[72]

The technique used here is to search for semileptonic Λ_c^+ decays. Lepton tagging has been used extensively in e^+e^- annihilation studies to tag and study heavy quark jets. It has not, however, been used in searches for specific particles.

This chapter will discuss the detection of semileptonic Λ_c^+ decays. It will then discuss the generation of upper limits for two of the more interesting all hadronic Λ_c^+ decay modes. Because so little is known about Λ_c^+ decays, the combination of these results can yield useful information about Λ_c^+ decay modes.

6.1 Λ_c Semileptonic Decays

Λ_c^+ are detected via their decays to Λ plus lepton. The general characteristic of this analysis followed the scheme used in the strange baryon searches. The data set, data selection, tracking program, hadronic event selection, and track quality cuts were identical.

Since Λ_c^+ are short lived, Λ from Λ_c^+ decays appear to point back to the origin. This property allows some of the cuts to be modified to improve the signal to noise ratio. The cuts used were:

1.   The distance from the reconstructed vertex to the interaction region in the x-y plane must be greater than 1 cm.

2.   The π track had to miss the origin by at least 1 mm.

3.   The proton track had to miss the origin by at least 0.6 mm.

4.   At the point of x-y intersection, the z coordinates of the proton and pion had to agree within 4 cm.

5. The Λ candidate had to have at least 1.5 GeV/c momentum. This cut removes slow Λ that are not likely to come from Λ_c^+ decays.

6. Finally, to improve the signal to noise ratio, a crude probability cut was applied. The probability depended on the above variables, plus the number of DAZMS found on each track inside the Λ decay radius.

These cuts led to the Λ signal shown in Fig. 6.1. The signal is small because of the tight momentum cut. This does not, however, reduce the efficiency for finding Λ_c^+. The same momentum dependent Λ mass cut used for the strange baryon analyses were used in this search. Again, all of the Λ candidates were subjected to a full three-dimensional vertex fit.
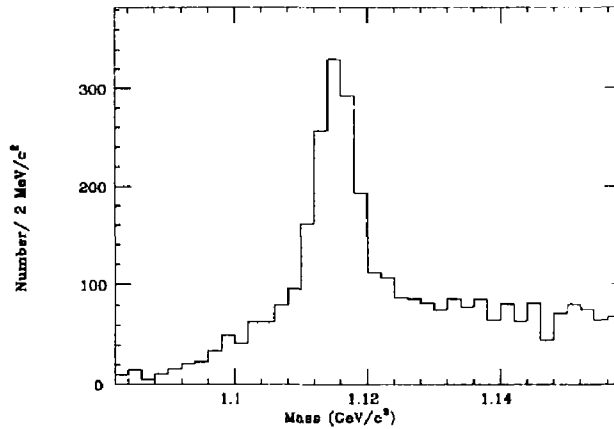
Figure 6.1. Λ signal for Λ_c^+ search.

Once a Λ was found, leptons were selected, as described in Chapter 4. The parameter TEST1 was required to be greater than 1.1. Electrons were required to have at least 1.5 GeV/c momentum. Because of the thickness of the muon system, muons were required to have at least 2 GeV/c of momentum. For each event, a thrust axis was determined[73] The thrust axis gives the direction of energy flow in the event; for two-jet events it is roughly the direction of the two primary quarks.

The thrust axis was used to divide the event into two hemispheres. The leptons were required to be in the same hemisphere as the Λ. A typical event is shown in Fig. 6.2.
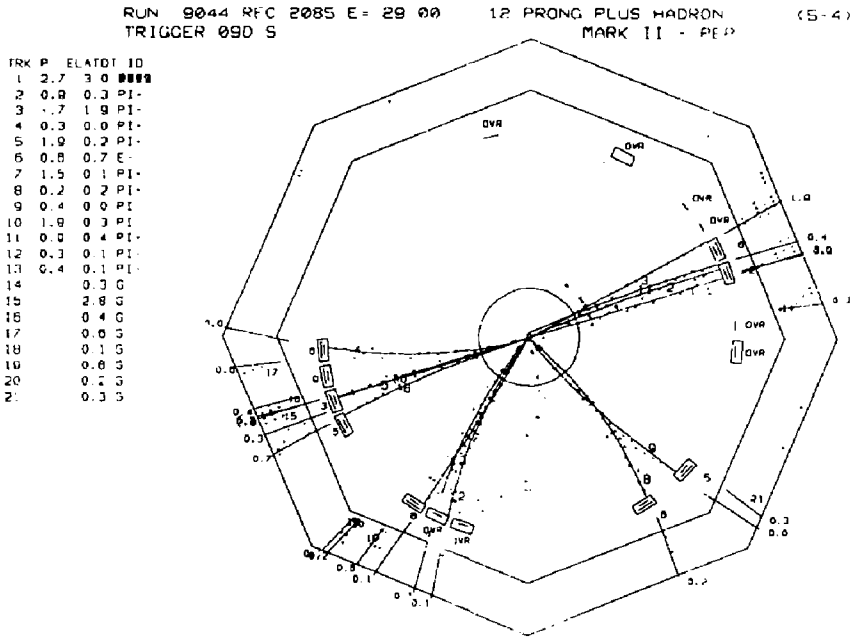
Figure 6.2. A typical Λ_c^+ semileptonic decay event. A $\overline{\Lambda}$ (tracks 3 and 11), an e^- (track 1), and one other track comprise an isolated jet.

The invariant mass distribution of combinations passing these cuts are shown in Fig. 6.3. Below the Λ_c^+ mass of 2.28 GeV/c^2, there is a clear excess of right sign events; 17 events compared to a background of five. This divides up to 11 electron and 6 muon events in the signal, versus 3 electron and 2 muon events in the background. Above the Λ_c^+ mass, there are 2 right sign and 2 wrong sign electrons, and 1 wrong sign muon event. To understand if this is a signal, we must consider the possible background sources.
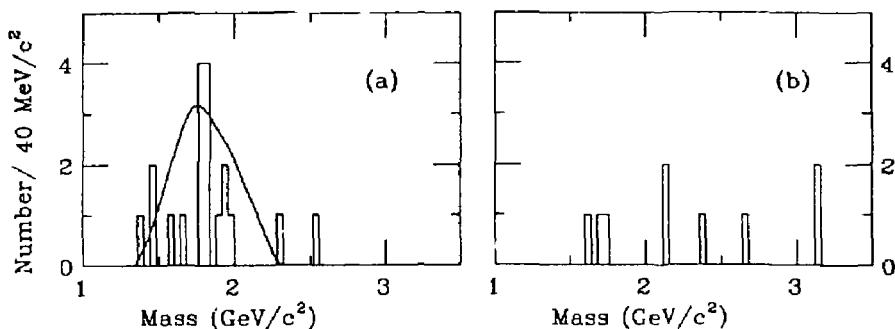
Figure 6.3. Invariant mass of Λ plus lepton combinations: (a) Right Sign; (b) Wrong Sign. The solid line is the Lund model prediction for $\Lambda_c^+ \to \Lambda l \nu$.

6.1.1 Backgrounds

There are a variety of possible background sources. The following sources were identified on the basis of hand scanning events and a study of backgrounds in Monte Carlo events. They are listed in order of decreasing importance:

1. K_s or random track combinations misidentified as Λ. Both of these sources should populate the right and wrong sign plots equally.

2. Lepton misidentification. The primary sources of fake leptons were fake electrons due to hadronic showers, fake muons from hadronic punchthrough into the muon system, and muons from in-flight pion and kaon decays.[74] In general, these misidentified leptons should populate the right and wrong sign background equally, except for a few specific decay modes. In particular, Ξ^- to $\Lambda \pi^-$ decays where the pion is identified as a lepton can populate the wrong sign plot in the region around 1.32 GeV/c^2. The decay Λ_c^+ to Λ π^+ can populate the right sign plot around the Λ_c^+ mass. To remove these decays, the regions between 1.31 and 1.33 GeV/c^2, and above 2.2 GeV/c^2 are removed from the analysis for both right and wrong sign combinations.

This does not affect the data signal or background; it does, however, affect some of the Monte Carlo events used in the efficiency calculation.

3. Combinatorics. A real Λ randomly combined with a real lepton. Naively, one might expect this background to be large. However, a study of Monte Carlo events indicates that it is relatively small, and that it does populate the right and wrong sign combinations equally. There are several qualitative reasons why it is small. First, heavy quark mesons have very hard fragmentation functions. They carry a large chunk of the energy available in that jet, leaving relatively little for other particles. Second, baryons are heavy, and they must be created in a baryon-antibaryon pair. Again, this takes a significant fraction of a jet's energy. Third, both the Λ and the lepton must have reasonably high momenta. At this momenta, the phase space to fit under the 2.28 GeV/c^2 mass cut is limited, so the background is small.

4. Bottom hadrons. *B* mesons sometimes decay to baryons. Some of the decays will be semileptonic. The decay *B* to lepton Λ_c^+, where the Λ_c^+ subsequently decays to a Λ will produce a wrong sign pair. Recent work by CLEO has shown that virtually all of the *B* meson decays to Λ go through a Λ_c^+.[75] It is also possible to have a *B* baryon decaying semileptonically to a Λ_c^+, which will also produce a wrong sign pair. However, both of these processes are suppressed because the branching ratios are quite low, and because there are only 1/4 as many *b* quark events as *c* quark events.

The relative abundance of these backgrounds was studied with Monte Carlo events. 111,000 Lund Monte Carlo events were generated and run through a complete detector simulation package. A total of 22 right sign and 21 wrong sign events were found, with an invariant mass below 3.5 GeV/c^2. Five of these had a momentum below the 4 GeV/c cut used in the analysis. The remaining 38 are classified in Table 6.1.

Mass	Right Sign		Wrong Sign	
	Low	High	Low	High
Real Λ_c^+	10	0	0	0
K_s as Λ	3	0	4	0
Combinatoric Λ	1	0	0	0
Fake leptons	6	1	2	2
Random combinations	1	1	1	1
Bottom hadrons	0	0	1	5
Total background	11	2	8	8

Table 6.1. Monte Carlo predicted backgrounds for Λ_c^+ taken from the Lund Monte Carlo. Low mass is below the Λ_c^+ mass of 2.28 GeV/c^2, while high mass is above that.

Because of imperfections in the Monte Carlo, these backgrounds cannot be taken at face value immediately. In particular, the version of the detector simulation used to generate these events used a lookup table to simulate hadronic interactions in the liquid argon. This table was known to generate too many fake electrons. To correct for this, the analysis program was also run on a separate set of Monte Carlo events generated with the BQCD event generator and a different lookup table for liquid argon hadronic interactions that generates too few fake electrons. The results of these two runs were then averaged. This procedure has been shown to produce a good estimate of the right number of fake electrons[76] Since the BQCD event generator does not generate charmed or bottom baryons, and since its bottom meson decay routines are very primitive, it was not used for the other background components. If we correct for the lepton misidentification probability, and average the non-bottom background over both signs, we get an estimated wrong sign level of 7.5, in good agreement with the data.

The shape of the background from *b* decays is also of interest. Fakes from *b* decays tend to have a much higher invariant mass than other sources; six out of the seven events from *b* decays have invariant masses above the Λ_c^+. Since there are so few high mass events in the data, we conclude that background from *b* decays is negligible.

Therefore, the wrong sign combinations will provide a good estimate of the background under the signal.

6.1.2 Λ_c decay modes

To understand the Λ_c^+ signal, we must understand the exact decay modes. Since we are only detecting part of the decaying Λ_c^+, special care must be taken in finding the detection efficiency, since it will depend on the exact decay modes. Since experimental results on Λ_c^+ decays are so sparse, we must turn to theoretical arguments.

A representative set of Λ_c^+ decay modes that one could consider are: $\Lambda l \nu$, $\Sigma^0 l \nu$, $\Sigma^{*0} l \nu$, $\Lambda \pi^0 l \nu$, and $\Lambda (\pi \pi)^0 l \nu$. There are other modes that one could consider, but these are fairly representative. Most other modes are either Cabbibo suppressed or have little phase space, or are eliminated by the arguments below.

1. The Λ_c^+ is isospin 0, while the modes $\Sigma^0 l \nu$, $\Sigma^{*0} l \nu$, and $\Lambda \pi^0 l \nu$ are all isospin 1. The isospin comes from the spectator ud diquark. Since the ud diquark is not involved in the weak charmed quark decay, isospin flip reactions should be suppressed, and therefore these channels should be suppressed.

2. A search was made for the mode $\Lambda (\pi \pi)^0 l \nu$. where the pions were charged. No candidates were found with a mass less than 2.28 GeV/c^2. Therefore, this mode should be negligible.

3. In Λ_c^+ decay, the charmed quark emits a virtual W, changing to a strange quark, as shown in Fig. 6.4. The W will give the strange quark a perpendicular momentum kick. So, if there are any $q\bar{q}$ pairs produced in the decay, they will be most likely to be created between the strange quark

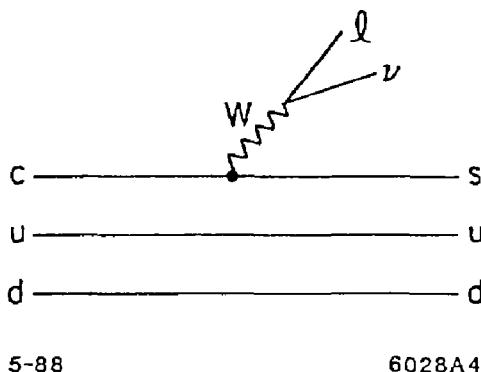and the two light quarks. If this occurs, then the final state will not include a Λ.

5-88   6028A4

Figure 6.4. Feynman diagram for Λ_c^+ semileptonic decay.

4. *D* meson decays can also provide a point of reference. The dominant *D* meson semileptonic decays are to single particle hadronic final states. These states are favored by a large margin.[77] *D* meson semileptonic decays have a higher Q^2 value than Λ_c^+ decays, so Λ_c^+ semileptonic decays should have an even lower average multiplicity. The Lund model follows this scheme; its default decay requires a single particle hadronic final state. If this default is overridden (keeping the weak matrix element decay), the branching ratio to $\Lambda \pi^0$ rises to about 15%.

5. While the statistics are limited, we can also get some hints from the data. The solid line in Fig. 6.3 is the Lund predicted Λ lepton spectrum for the mode Λ $l\nu$ only. The match is fairly good. Models with additional decay products have mass spectra that peak at somewhat lower values.

For these reasons, this analysis will treat the decay mode $\Lambda l\nu$ as the standard mode, and allow for the others in the systematic errors. The exact mode affects the efficiency and observed momentum spectrum in several ways. First, if there

are additional particles, either from the Λ_c^+ decay, or from a secondary $\Sigma \rightarrow \Lambda$ decay, mass and momentum will be carried away. The average observed Λ plus lepton invariant mass and momentum will be lower. This will affect the efficiency, as shown in Fig. 6.5 (invariant mass) and Fig. 6.6 (momentum). These figures show that these effects can be significant. To give an idea of how much these parameters depend on the exact final state, Fig. 6.7 shows the differences between two final states.
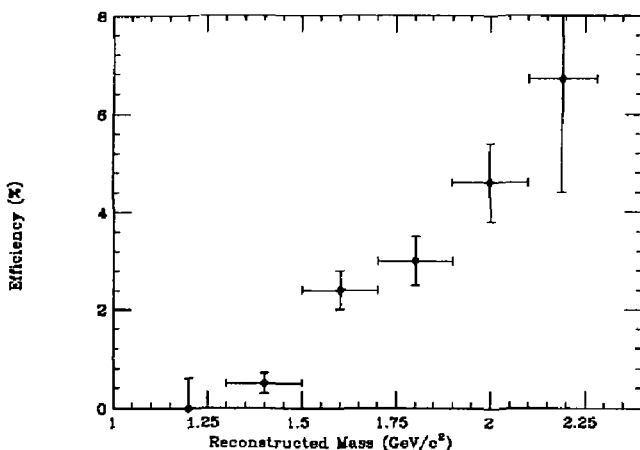
Figure 6.5. Λ_c^+ detection efficiency versus Λ plus lepton invariant mass.

One goal of this analysis is to find the Λ_c^+ cross section as a function of momentum. This would require unfolding the observed Λ_c^+ spectrum to allow for the effects of the missing particles. Unfortunately, with the limited momentum coverage available and the low statistics, it is not possible to do a meaningful job of this. Instead, we can compare the observed Λ plus lepton spectrum with the predictions of the Lund Monte Carlo, as is shown in Fig. 6.8.

The Lund model appears to give a fairly good fit to the data, although it is hard to say much given the very limited statistics. The only real conclusion that
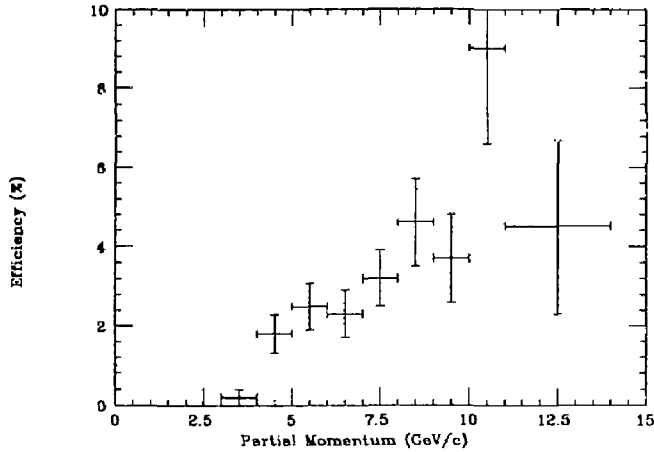
Figure 6.6. Λ_c^+ detection efficiency versus observed Λ plus lepton momentum.

can be drawn is that the Λ_c^+ spectrum is roughly similar to that of other charmed particles, rather than that of lighter baryons.

6.1.3 Λ_c Production Rate

A useful quantity to measure is $\sigma(e^+e^- \to \Lambda_c X) \times Br(\Lambda_c \to l\Lambda X)$. This requires a knowledge of the detection efficiency. Since the Monte Carlo and the data are in reasonable agreement for both the reconstructed mass and the reconstructed partial momentum, given the limited statistics, the raw (single number) efficiency provided by the Monte Carlo should be adequate. It is $3.3 \pm 0.4\%$ for electrons and $1.4 \pm 0.3\%$ for muons. Because some of the wrong sign background (from b decays) is correlated with Λ_c^+ production, the wrong sign background from the Monte Carlo is subtracted from the right sign signal before calculating the efficiency. Using these numbers, there are 273 ± 109 electronic and 214 ± 214 muonic Λ_c^+ decays. The error for the muon subsample is much
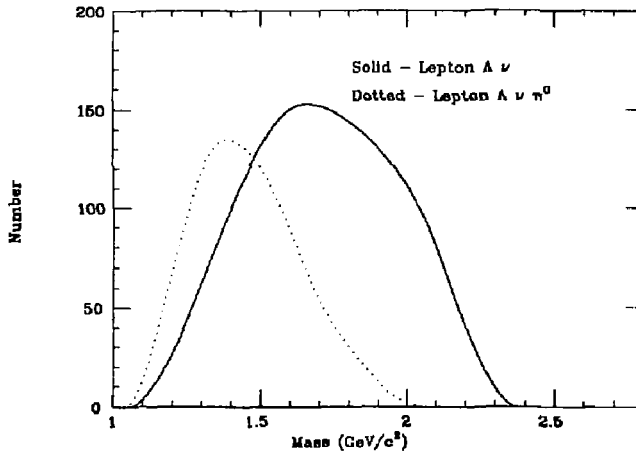
Figure 6.7. Monte Carlo predicted Λ + lepton invariant mass spectra for two different Λ_c^+ final states. The solid line is for $\Lambda l \nu$, while the dotted line includes an additional pion, assuming a standard weak matrix element decay. These curves are not detector acceptance corrected.

larger because the muon background is worse. This is a total of 487 ± 240 Λ_c^+ semileptonic decays.

Although the statistics are limited, we can also try breaking up the data set into several partial momentum bins, to remove the effects of a possible momentum spectrum mismatch between the data and the Monte Carlo. This was done, and the results were within 0.5 σ of the above result.

Many of the systematic errors in this measurement were considered in the strange baryon analysis. The systematic errors for the tracking efficiency, Monte Carlo imperfections, drift chamber inefficiency, luminosity, and Monte Carlo statistics are unchanged from the previous chapter. The corrections to and uncertainty in the lepton identification efficiency stem from the fact that the lepton finding efficiency is slightly higher in the Monte Carlo than in the data.[44] The decay
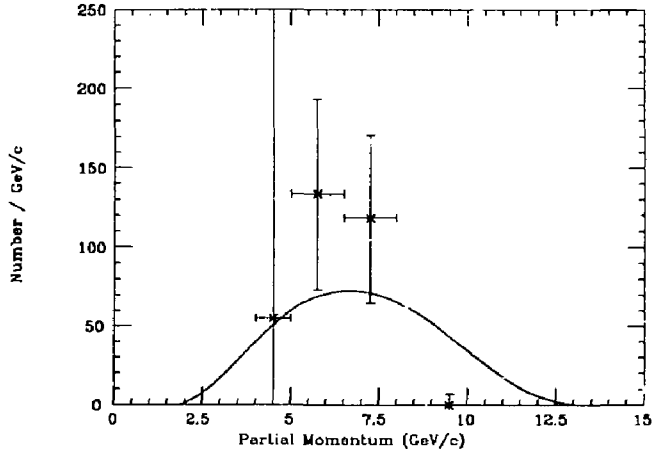
Figure 6.8. Observed momentum of Λ plus lepton combinations after background subtraction.

mode uncertainty was described in the previous section. Antiproton annihilation accounts for the fact that, by annihilating in the liquid argon, antiprotons may be more likely to produce fake electrons than other hadrons. Since baryons are produced close together in rapidity, Λ antiproton associated production has a slightly increased probability of faking a background wrong sign event. These systematic errors are summarized in Table 6.2.

With these corrections, we find $320 \pm 127 \pm 105$ electronic and $250 \pm 250 \pm 75$ muonic Λ_c^+ decays in the 207 pb^{-1} data set. With radiative corrections, using the same procedure used in the previous chapter,

$$\sigma(e^+e^- \to \Lambda_c X) * Br(\Lambda_c \to e\Lambda X) = 1.2 \pm 0.5 \pm 0.4 \text{ pb} ,$$

Item	Correction	Error (%)
Tracking	1.05	9
Lepton Identification	1.03	5
Antiproton Annihilation	1.0	0/8
Monte Carlo Imperfections	1.0	10
Drift Chamber Inefficiency	1.09	5
Decay Mode Uncertainty	1.0	25
Luminosity	1.0	2
Monte Carlo Statistics	1.0	8
Total	1.17	30/31

Table 6.2. Systematic corrections and cross sections for Λ_c^+ detections. The first number in the error column is for the muon subsample, and the latter is for the electrons.

or $0.0031 \pm 0.0012 \pm 0.0010$ per hadronic event, and

$$\sigma(e^+e^- \to \Lambda_c X) * Br(\Lambda_c \to \mu \Lambda X) = 1.0 \pm 1.0 \pm 0.3 \text{ pb} ,$$

or $0.0024 \pm 0.0024 \pm 0.0007$ per hadronic event.

6.1.4 Estimates of Branching Ratios

To put these numbers in perspective, it is useful to make some estimates of Λ_c^+ production, and use them to calculate branching ratios. Before discussing specific models, one theoretical uncertainty should be considered. None of the estimates include the possibility of primary diquark production, as was shown in Fig. 2.3(c). Since Λ_c^+ come mainly from primary charmed quarks, Λ_c^+ production is very sensitive to this possibility.

The event shown in Fig. 6.9 appears to indicate that leading diquark production may occur. It is compatible with $e^+e^- \to \Lambda_c \bar{\Lambda}_c \pi^0$. One Λ_c^+ decays

semileptonically; the other decays to $pK\pi\pi^0$. There are two photons that make a reasonable candidate for one of the π^0, and energy deposition where the other one could be. In fairness, it should also be added that there is a lot of missing energy in both jets. Either the event is radiative, or there is either a neutrino or a lot of missing neutral energy in the 'hadronic' jet. If the $\Lambda_c\bar{\Lambda}_c$ interpretation is correct, in the absence of leading diquarks, the probability of observing such an event is quite low.
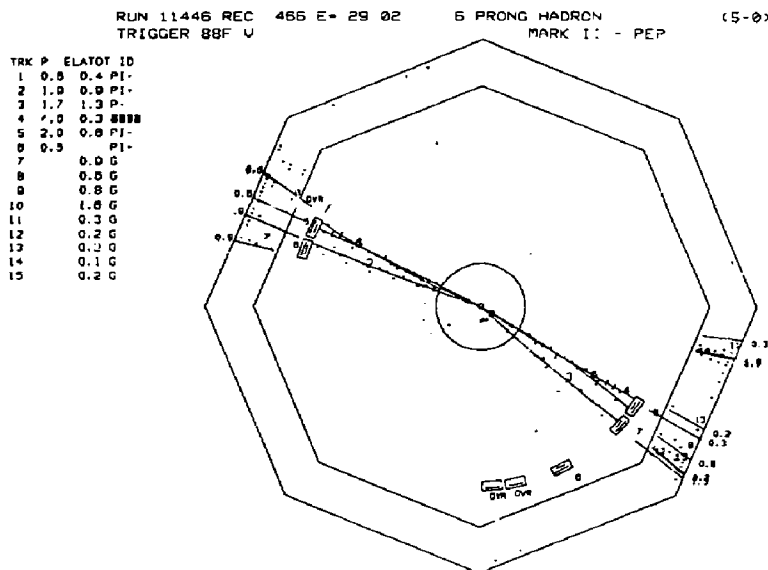
Figure 6.9. A candidate for $e^+e^- \to \Lambda_c\bar{\Lambda}_c\pi^0$. One Λ_c^+ decays semileptonically, the other decays hadronically to $pK\pi\pi^0$. This event is not otherwise included in this analysis, because the Λ only satisfied the cuts if PTRAKR tracking was used; with SUPTRKR, one of the Λ tracks came too close to the origin. Since the PTRAKR track had a much lower χ^2, 8.5 for 6 degrees of freedom, compared with 42.1 for 7 degrees of freedom for SUPTRKR, I believe that PTRAKR found the track properly, and it really is a Λ.

The Lund model, with standard parameters, predicts 0.06 Λ_c^+ per event. The Lund model is general enough, and the parameters are well enough determined,

that any string type diquark model will predict a number close to this. The largest theoretical uncertainty is that there may be some primary diquark production, which would increase the production rate. Although there are limits on leading diquark production from other sources, Λ_c^+ production rate is very sensitive to this, so the other measurements are not meaningful here. With the Lund estimates,

$$Br(\Lambda_c \rightarrow e\Lambda X) = 5.1 \pm 2.0 \pm 1.7\%$$

and

$$Br(\Lambda_c \rightarrow \mu\Lambda X) = 4.0 \pm 4.0 \pm 1.2\% \; .$$

In the UCLA model, where hadron production depends only on the mass of the final state hadron, Λ_c^+ production is much lower, 0.018 Λ_c^+ per hadronic event. This is because the Λ_c^+ is very heavy compared with the typical hadron. This gives significantly higher semileptonic branching ratios:

$$Br(\Lambda_c \rightarrow e\Lambda X) = 17 \pm 7 \pm 6\%$$

and

$$Br(\Lambda_c \rightarrow \mu\Lambda X) = 13 \pm 13 \pm 4\% \; .$$

The Webber model prediction is intermediate between the Lund and UCLA predictions, 0.026 Λ_c^+ per event. With it,

$$Br(\Lambda_c \rightarrow e\Lambda X) = 12 \pm 5 \pm 4\%$$

and

$$Br(\Lambda_c \rightarrow \mu\Lambda X) = 9 \pm 9 \pm 3\% \; .$$

These numbers can be compared with previous results and theoretical expectations. Mark II at SPEAR found[78]

$$Br(\Lambda_c \rightarrow e\Lambda X) = 1.1 \pm 0.8\% \; ,$$

and the more general

$$Br(\Lambda_c \to eX) = 4.5 \pm 1.7\% \; .$$

This measurement is based on measuring the increase in total proton and Λ production in e^+e^- annihilation as the beam energy is increased across the threshold for $\Lambda_c\overline{\Lambda}_c$ production. All of this increase was attributed to Λ_c^+ production. From this increase, the total Λ_c^+ production rate was estimated. Then, the number of electron baryon pairs was counted to estimate the semileptonic branching ratio, and the number of electron Λ pairs to estimate the ΛeX ratio. This procedure includes several assumptions, and these numbers may be systematically low. Considering the arguments made in the last section, it is surprising that the two measurements are so far apart; most of the semileptonic Λ_c^+ decays should include a Λ.

There is also a result from the Fermilab 15 foot bubble chamber.[79] The data contained neutrino induced dilepton events. A search was made for events which contained a Λ in addition to the two leptons. Only one candidate was found, and with certain assumptions about the Λ_c^+ production rate, an upper limit of

$$Br(\Lambda_c \to e\Lambda X) < 2.2\%$$

was found, at a 90% confidence level.

If these branching ratios are correct, they indicate that Λ_c^+ production in 29 GeV e^+e^- annihilation is substantially higher than predicted by any of the models. In that case, one possible fix for the models would be to allow for the possibility of direct diquark production.

Some theorists, however, think that the SPEAR measurement is too low. A recent calculation used the SPEAR branching ratios to find that $|V_{cs}|$ is much less than one,[80] in strong contradiction with results obtained from D meson decays. If the calculation is correct, a more likely explanation is that the Λ lepton branching ratio is higher than the SPEAR measurements.

We can also get an idea of the expected semileptonic branching ratio by comparing with the D meson family, as shown in Table 6.3.

Particle	Br(e X)	Lifetime (10^{-13} s)
D^+	18.2 ± 1.7	10.5 ± 0.3
D^0	7.0 ± 1.1	4.3 ± 0.1
Λ_c^+	?	1.9 ± 0.2

Table 6.3. Charmed hadron semileptonic branching ratios and lifetimes.

There is a roughly linear relationship between semileptonic branching ratio and lifetimes. The linear relationship comes from a spectator quark model; other effects such as other diagrams and hadronic form factors will destroy the linearity. Still, the agreement is very good for D mesons, and these other factors are expected to be small: 2 or 3 and not 10 or 20.

From these arguments, we can conclude that the $\Lambda_c \rightarrow \Lambda l \nu$ branching ratio should be reasonably small, probably less than 10%. The Lund model appears to do a good job of estimating Λ_c^+ production. The UCLA model appears to predict too few Λ_c^+, while the Webber model may predict too few Λ_c^+.

6.2   Hadronic Λ_c Decays

The majority of Λ_c^+ decays are to completely hadronic final states. Detecting these final states is difficult because these analyses suffer from large backgrounds due to random combinatorics. On the other hand, because the final state is completely reconstructed, there should be an observable peak, so the background should be easy to measure.

Since Λ_c^+ decay branching ratios are poorly known, it is hard to know which final states are most likely to be found. In this analysis, I searched for the final states $pK^-\pi^+$, $\Lambda 3\pi$, $\Lambda\pi$, and pK_s. None of these searches gave positive results.

All of the searches used the same hadronic event cuts, track cuts, and tracking programs used earlier. For searches requiring a Λ, the same cuts were used as for the semileptonic Λ_c^+ analysis. For searches which required a K_s, a subroutine similar to that used for Λ was used. The cuts used were:

1. The distance from the reconstructed vertex to the interaction region in the x-y plane must be between 8 mm and 70 cm. The upper limit removes K_s which are far enough out in the drift chamber that they are likely to be very poorly tracked.

2. At the point of x-y intersection, the z coordinates of the two pions had to agree within 4 cm.

3. The K_s candidate had to have at least 750 MeV c momentum.

4. Finally, to improve the signal-to-noise ratio, a crude probability cut was applied. The probability depended on the above variables, plus the number of DAZMS found on each track inside the K_s decay radius.

These cuts led to the K_s signal shown in Fig. 6.10. K_s passing these cuts were constrained to a single point, as with the Λ, and required to have a vertex fit χ^2 less than 10 for 1 degree of freedom. Accepted candidates were required to be within 20 MeV c^2 of the nominal K_s mass.

In the following sections, cuts (in particular the momentum cuts) are chosen to match the cuts used in the semileptonic analysis as closely as possible. This is done to reduce the systematic errors from spectrum extrapolation in calculating ratios of branching ratios.

6.2.1 Decays to $pK\pi$

All properly charged triplets were tested against the $pK^- \pi^+$ hypothesis. All three tracks were required to be in the same hemisphere, as determined by the thrust axis. To reduce the combinatorial background, the proton, kaon, and pion were required to have momenta of at least 2.0, 1.0, and 0.8 GeV c, respectively. The proton was required to have a larger momentum than the pion. The latter
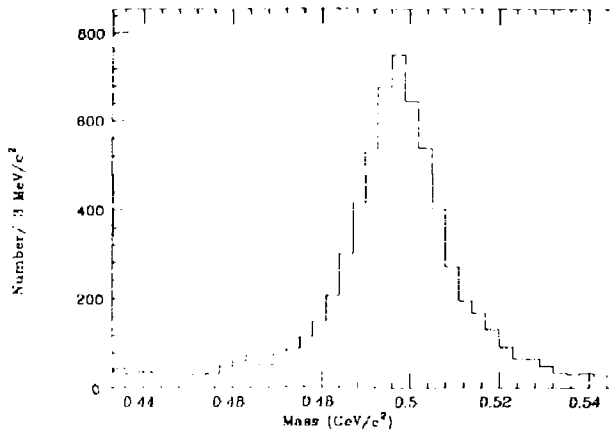
Figure 6.10. K_s signal used in Λ_c^+ searches.

cut was made to reduce the problems of $pK^-\pi^+$ combinations where the pion and proton tracks were switched. The combination was required to have at least 5.5 GeV/c. This value was chosen to match as closely as possible the requirement from the semileptonic decay analysis that the Λ plus lepton momentum be at least 4.0 GeV/c.

These cuts lead to the mass spectrum shown in Fig. 6.11. No signal is visible. The width of the expected signal was estimated from a Monte Carlo simulation to be 60 MeV/c². The mass of the Λ_c^+ is $22°2 \pm 2$ MeV/c²,[81] and the uncertainty in the detector mass scale (including the effects of the fitting procedure) was estimated to be 4 MeV/c². The data was fit with a fixed width Gaussian plus a cubic background. The Λ_c^+ mass was fixed, and the fit was done at 1 MeV/c² intervals in the region from 2278 to 2286 MeV/c². The results varied slowly over this region; the fit at 2278 MeV/c² was used since it gave the largest upper limit. The efficiency was measured to be $33.9 + 3.5$ %, including the effects of the fit. The efficiency was adjusted to account for the small remaining proton-pion reflection. The systematic errors include the pertinent ones from the Λ_c^+ semileptonic decay

analysis, plus a 10% uncertainty to account for the results of the fitting. Adding the systematic and statistical errors linearly and including radiative corrections leads to the result

$$\sigma(e^+e^- \rightarrow \Lambda_c X) * Br(\Lambda_c \rightarrow pK^+\pi^-) < 7.0 \text{ pb}$$

at a 90% confidence level. This result can be compared with the semileptonic result. Here, many of the systematic errors cancel out, giving

$$\frac{Br(\Lambda_c \rightarrow pK^+\pi^-)}{Br(\Lambda_c \rightarrow e\Lambda X)} < 8.4$$

again at a 90% confidence level. Here, the statistical errors are added in quadrature, then the systematic errors are added linearly. Because of the much larger statistical errors, the upper limit for the muon case is larger.
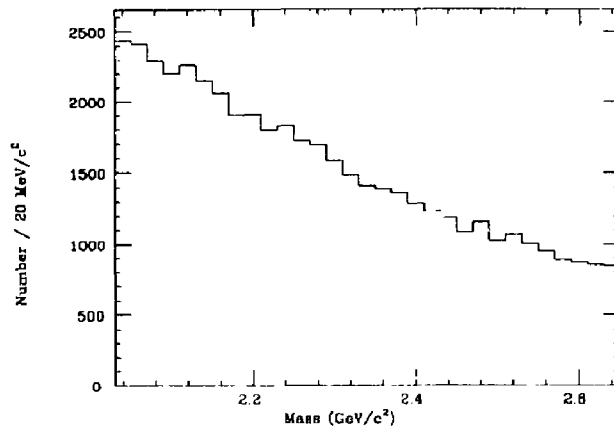

Figure 6.11. Invariant mass of $pK^-\pi^+$ combinations. No signal is visible; a fit led to a result of 281 ± 204.

Neither case is especially interesting, since $Br(\Lambda_c \rightarrow pK^+\pi^-)$ has been measured by Mark II/SPEAR to be $2.2 \pm 1.0\%$.[52]

6.2.2   Decay to $\Lambda\pi\pi\pi$

For this search, all Λ were paired with all properly charged pion triplets in the same hemisphere. The pions were required to have a momentum of at least 400 MeV/c, while the Λ was required to have a momentum of at least 2.0 GeV/c. As with the $pK^-\pi^+$ search, the combination was required to have a momentum of at least 5.5 GeV/c.

These cuts lead to the mass spectrum shown in Fig. 6.12.
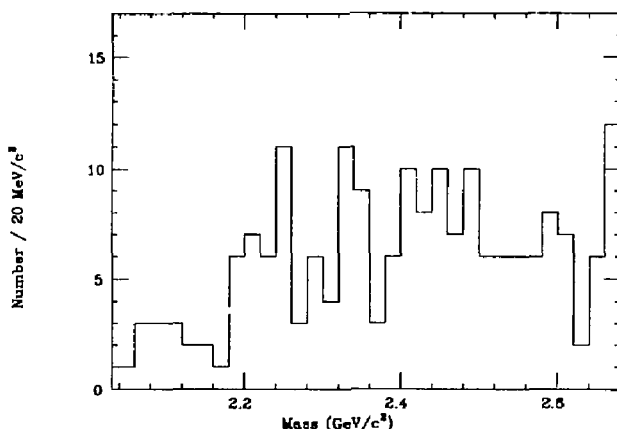
Figure 6.12. Invariant mass of $\Lambda\,\pi\pi\pi$ combinations. No signal is visible.

6.2.3   Decay to $\Lambda\pi$

Although the branching ratio to $\Lambda\pi$ is believed to be low,[81] the low combinatoric background made this an attractive channel to search. The Λ were required to have a momentum of at least 2.0 GeV/c, the pions were required to have at least 1.0 GeV/c momentum, and the combination was required to have at least 5.5 GeV/c momentum. Both particles were required to be in the same hemisphere. This led to the distribution shown in Fig. 6.13. There is a 2–3 event excess around the Λ_c^+ mass, but it is of very limited statistical significance. A

variety of cuts were studied in an attempt to enhance the signal, but with no success.
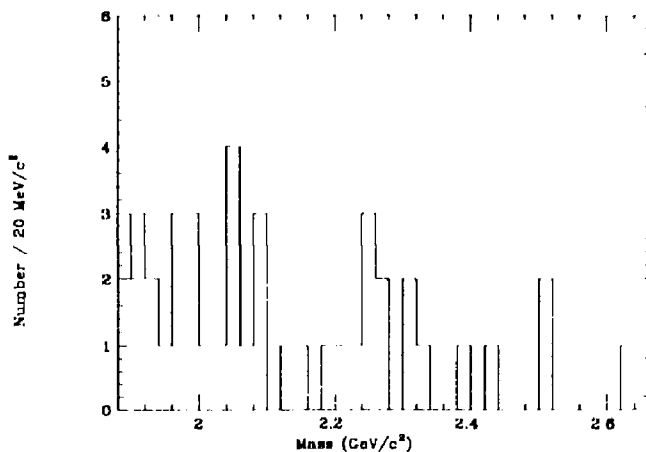
Figure 6.13. $\Lambda \pi^+$ invariant mass combinations.

6.2.4 Decays to pK_s

Λ_c^+ decays to proton K_s have been observed by several experiments. This search followed the pattern developed above; the proton was required to have at least 2.0 GeV/c of momentum. K_s were selected via the cuts listed above, and required to have at least 1.0 GeV/c momentum, and to be in the same hemisphere as the proton. This led to the distribution shown in Fig. 6.14. No signal is visible.

6.3 Σ_c **Production**

One interesting application of this $\Lambda_c \rightarrow \Lambda$ sample is to search for Σ_c^{++} and Σ_c^0 decaying to $\Lambda_c^+ \pi$. Normally, this is done in the same way that D^* decays to D^0 are found, by finding $\Delta m = m(\Sigma_c) - m(\Lambda_c)$. The resolution for Δm is very good, on the order of a few MeV/c^2, allowing the background to be greatly
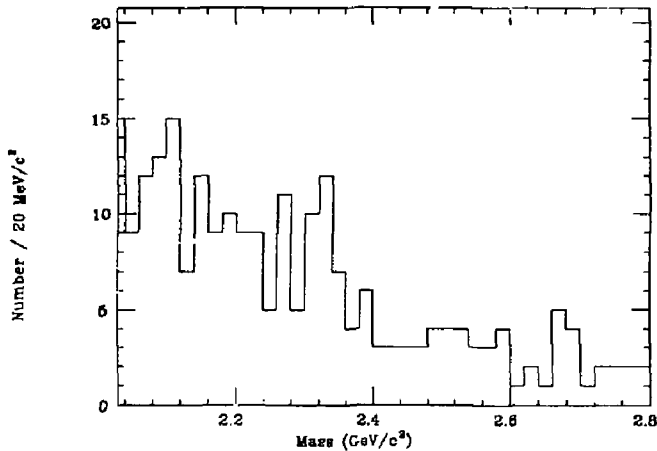
Figure 6.14. proton K_s invariant mass combinations.

reduced. Since, in this analysis, the Λ_c^+ direction is known with limited accuracy, the Δm resolution is much worse.

Figure 6.15 shows the Δm distributions for doubly charged and neutral combinations. The superimposed solid lines are the Monte Carlo predictions made from a tape where each event contains a Σ_c^{++} or Σ_c^0. Based on a study of four-vectors, the Δm signal region extends from roughly 140 MeV/c^2 to 190 MeV/c^2. The tracks used here are required to be in the same hemisphere as the Λ_c^+, and are required to pass the same track cuts described earlier.

There are one doubly charged and two neutral candidates. Because of uncertainties in the shape, no background subtraction was done. These numbers give 90% upper limits of 3.9 and 5.3, respectively. If we divide by the relative efficiency for detecting Σ_c compared with Λ_c^+, determined from the Monte Carlo, and add an appropriate correction for the single track efficiency, the numbers

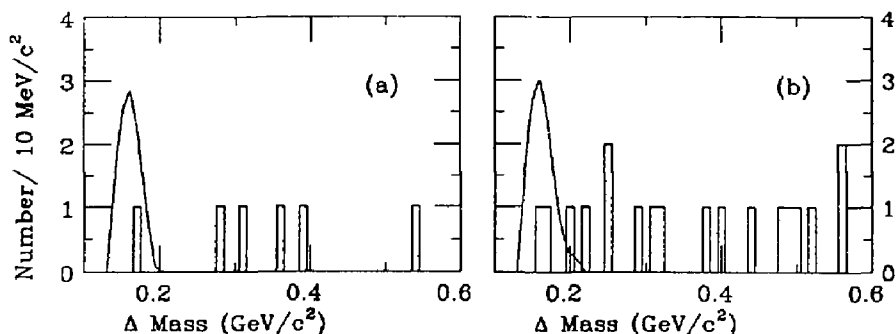**Figure 6.15.** Δm distribution for (a) $++$ and (b) neutral charge combinations.

increase to 6.7 and 7.7 events. Dividing by the observed number of Λ_c^+, $N(\Sigma_c^{++})$ / $N(\Lambda_c^+) < 0.56$ at a 90% confidence level and $N(\Sigma_c^0)$ / $N(\Lambda_c^+) < 0.63$ at a 90% confidence level.

Unfortunately, these numbers are uninteresting, even before systematic errors are added. Even if all Λ_c^+ comes from Σ_c production, it should be divided equally between Σ_c^{++}, Σ_c^+, and Σ_c^0, with 1/3 of the Λ_c^+ coming from each source. With better statistics, though, this could be very interesting, since the Σ_c to Λ_c^+ ratio provides a fairly direct measurement of isospin 1 to isospin 0 diquark, and is a good test of the diquark model.

6.4 Searches for Charmed Strange Baryons

There are many other ways one could imagine to look for charmed baryons. A good variety were tried here.

Semileptonic decays of charmed strange baryons were searched for, decaying to a lepton plus a Ξ^- or an Ω^-. Cuts used were similar to those used for the Λ_c^+ semileptonic decay. One candidate event was found, decaying to Ξ^- plus electron. The partial mass was 1.51 GeV/c^2, and the partial momentum was 2.6 GeV/c. No wrong sign of high mass background events were found in either channel.

A variety of searches were conducted for hadronic decays of charmed strange baryons. Final states were chosen which could take advantage of the particle identification provided by Λ and K_s selection.

A search was made in the final states ΛK, for both charged and neutral kaons. No significant bumps were found.

Searches were made for neutral particles decaying to Ξ^- and Ω^-, plus a charged pion or kaon. The Ξ^- and Ω^- samples described in the previous chapter were used. All other charged tracks were tried as both kaons and pions. The resulting combination was required to have a momentum of at least 1 GeV/c. The $\Xi^- \pi^+$, $\Xi^- K^+$, and $\Omega^- \pi^+$ histograms showed no significant enhancements. However, a potential signal was observed in the channel $\Omega^- K^+$.

The enhancement was narrow, compatible with the experimental resolution, and is shown in Fig. 6.16. The signal is generally consistent with background, except for the region around 2.44 GeV/c^2. This is the region where the Ξ_c is expected to occur. The signal contains 13 events, compared to an estimated background of 3.75. The probability for a random fluctuation of this magnitude to occur is roughly 1 in 2500. On closer examination, however, the signal becomes less impressive. If these were real Ξ_c, they should be randomly distributed in $\cos(\theta)$, where θ is the angle between the Ξ_c and the Ξ^- momenta, projected into the Ξ_c rest frame. The $\cos(\theta)$ distribution is shown in Fig. 6.17. The observed distribution is consistent with being completely background. Unfortunately, there is one further problem with the signal; many of the Ξ_c candidates share an Ω^-. If doubly used Ω^- are eliminated by taking the Ξ_c candidates with $\cos(\theta)$ closest to zero, the signal drops to 5 over an estimated background of 1.375. The probability of a random fluctuation of this magnitude occurring is roughly 1%. Further, if the momentum cut is increased to 2 GeV/c, the signal also drops. If the signal were really Ξ_c, it should have a hard spectrum, similar to that from the Λ_c^+. The various statistical probabilities for various cut choices are given elsewhere[83] So while this

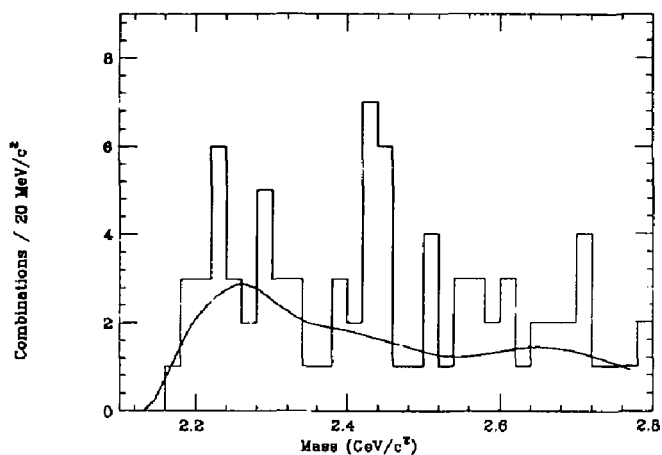**Figure 6.16.** $\Omega^- K^+$ invariant mass plot. The solid line is the predicted background taken from Monte Carlo.
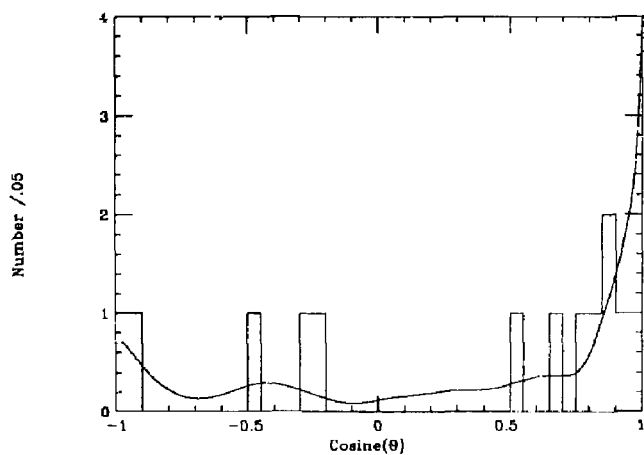

Figure 6.17. $\text{Cos}(\theta^*)$ distribution for the Ξ_c candidates. The solid line is the Monte Carlo prediction for fake Ξ_c.

may be a signal, it could also be a statistical fluctuation. If it is a signal, it could explain the high rate of Ω^- production.

Chapter 7. Conclusions

In the past two chapters, several measurements of baryon production have been presented. While they are interesting individually, to really test models of baryon production, they must be considered in concert.

7.1 Strange Baryons

The production rate of various baryons as a function of strangeness is shown in Fig. 7.1. These predictions are compared with the various Monte Carlo generators in Table 7.1. In considering these predictions, it is important to realize that much of this production is indirect. For example, a Ξ^{*0} will decay to a Ξ^-, which will in turn decay to a Λ. So, the measured Λ rate includes actual Ξ^- rate and the actual Ξ^{*0} rate. In fact, the Lund Monte Carlo predicts that only about 40% of all Λ are produced directly in fragmentation; the rest come from decays of heavier baryons. As baryon strangeness increases, this percentage increases smoothly; roughly 70% of Ω^- are directly produced. While Monte Carlos simulate these decays, there are inaccuracies, especially when considering baryons whose decays are poorly measured or unknown. Fortunately, for the results considered here, this problem is not deadly. Because heavier baryons tend to be rarer, the corrections are manageable. For example, $\Sigma^{*\pm}$ production only accounts for 17% of Λ, the errors in this number are quite manageable.

In general, the rates for spin 3/2 baryons are much lower than the rates for equally strange spin 1/2 baryons. For the spin 1/2 baryons, the production rate decreases as strangeness increases. Although the data for spin 3/2 baryons is very limited, it appears to follow the same trend, except for the Ω^-. The production rate for Ω^- appears closer to the spin 1/2 family than the spin 3/2 baryons. In fact, the Ω^- production rate is roughly what one would expect for a hypothetical spin 1/2 triply strange baryon.

A closer look shows that the Ω^- production rate is probably higher than the Ξ^{*0} production rate. This is very hard to explain in any model. The Ω^- is stranger
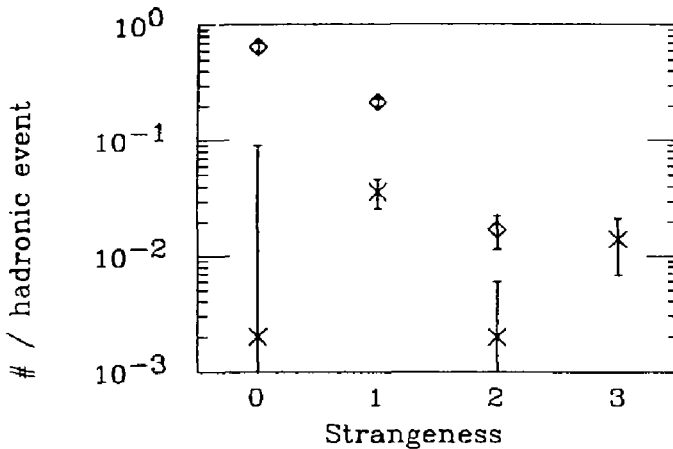
Figure **7.1.** Baryon production rates as a function of strangeness. The diamonds are spin 1/2 baryons, while the crosses represent spin 3/2 baryons. The measurements come from: proton–TPC[84] and TASSO,[18] Λ – Mark II,[61] Ξ^-, Ω^-, and Ξ^{*0} – this work, Δ^{++}–TASSO[85] and $\Sigma^{*\pm}(1385)$ –TPC[67] and HRS.[63] The points for $\Sigma^{*\pm}$ and proton are weighted averages. The $\Sigma^{*\pm}$ is the sum of both charged states. This is the way the results were quoted by the experimentalists, even though the two states are not particle-antiparticle.

than the Ξ^{*0}, so it should be suppressed by some strangeness suppression factor. It is heavier than the Ξ^{*0}, so it will be suppressed in any scheme involving mass based suppression. So, the unexpectedly high rate of Ω^- suppression is somewhat of a puzzle.

I will give four possible resolutions to this puzzle. One possibility is that the Ω^- are produced by some unexpected mechanism. One way to do this would be if the Ω^- were produced in the decay of some heavier baryon at an unexpectedly high rate. While all the Monte Carlo models account for decays of heavier states, they all handle it somewhat crudely. If Ω^- are produced in some special decay, the Monte Carlos would be thrown off.

Particle	Mass	S	Spin	Rate	Lund	UCLA	Webber
proton	.939 GeV/c^2	0	1/2	0.60 ± 0.06	0.57	0.49	0.48
Λ	1.115 GeV/c^2	1	1/2	0.213 ± 0.02	0.19	0.21	0.24
Ξ^-	1.321 GeV/c^2	2	1/2	0.017 + 0.06	0.014	0.02	0.039
Δ^{++}	1.232 GeV/c^2	0	3/2	<0.09	0.055	0.11	0.11
$\Sigma^{*\pm}$	1.385 GeV/c^2	1	3/2	0.036 ± 0.010	0.024	0.07	0.07
Ξ^{*0}	1.532 GeV/c^2	2	3/2	<0.006	0.014	0.012	0.020
Ω^-	1.672 GeV/c^2	3	3/2	0.014 ± 0.07	0.0004	0.002	0.006

Table 7.1. Monte Carlo predictions for baryon production compared with experimental results. S stands for strangeness. The data is from the same sources as Fig. 7.1. The upper limits are at a 90% confidence level.

Second, the Ω^- could be treated specially because they are made of three identical quarks. If one envisioned a non-diquark based model, one could postulate that quark flavors are chosen before baryon spin is determined. Three strange quarks are then forced to be spin 3/2, while two strange quarks plus one light quark can be spin 1/2 or spin 3/2. If, given this choice, the spin 3/2 state is suppressed, then this could explain the data. This scheme would also affect the Δ^{++} and Δ^0 production rates. There is an upper limit on Δ^{++} production, but after one accounts for heavier baryon decays, the limit appears loose enough to accommodate the Δ^{++} to proton ratio. The main objection to this comes from isospin invariance which expects the Δ^{++}, Δ^+, Δ^0, and Δ^- to be produced in equal numbers; in this scheme the Δ^{++} and Δ^- would be enhanced.

The third explanation has to do with feedown from heavier states. The Monte Carlos used all have very simple mechanisms for decaying heavier baryons. If there is a heavier state with an unexpectedly large decay rate to Ω, it could explain the excess. One possibility for this is the Ξ_c decay discussed in the previous chapter.

Finally, the observed Ω^- signal could be a statistical fluctuation. The probability for a background of 7 to fluctuate to a signal plus background of 23 is slightly over 1 in 1,000,000.

One of the main purposes of experiment is to test theory, since there are no solid calculations of baryon production here, we will compare these results with Monte Carlo models.

7.1.1   The Lund Model

Since it has the most generality, and the most free parameters, the Lund model should be able to fit the data well. The Lund model does fit most of the points well. However, it fails miserably for the Ω^-, predicting only 1/35 of what the data indicate. This is because the Lund model has a huge spin 1 diquark suppression factor, and fairly large strangeness suppression factor, coupled with an extra suppression factor for strangeness in diquarks. While it is possible to adjust these factors, the agreement with the other points is then lost. In particular, the way the model is structured, the Ω^- to Ξ^{*0} ratio cannot be larger than P_s, the strangeness suppression factor. P_s has been well measured to be around 0.3 from studies on mesons. So, its inability to handle the Ω^- rate is a significant failing of the Lund model. The reason that a failure on a single particle rate is significant is because the Lund model has so many free parameters; many data points must be used to fix the parameters, leaving fewer points for use as tests. For baryons, the Λ is used to set the overall diquark rate, the Ξ^- can fix the extra suppression factor for strange diquarks, and the $\Sigma^{*\pm}$ can determine the spin 1 suppression rate. This leaves very little to test the model, especially when one considers that the roughly 75% of protons come from decays of heavier objects.

7.1.2   The UCLA Model

The UCLA model bases hadron production solely on hadron (not quark) masses. Because of this, in principle it has essentially no free parameters; it either

works or it does not. In practice, there are a few open areas. In particular, 'popcorn' is not yet implemented so that this is not quite true. However, it has far less freedom than any of the other models considered.

Despite its lack of free parameters, the UCLA model does a surprisingly good job of reproducing the data. It is within one or two experimental σ for all of the baryons. Its main failings are with the Ξ^{*0}, where it predicts twice the upper limit, and the Ω^-, where it is off by a factor of 7. This isn't any worse than the Lund model, though. Considering that the UCLA model is based on a simple ansatz with no real theoretical justification, the UCLA model shows other Monte Carlos how easy it is to approximate the data roughly, with one very simple assumption. If nothing else, the UCLA model should be a warning not too read too much physics into these models.

7.1.3 The Webber Cluster Model

In the Webber model, less attention is given to particle production. There are many fewer free parameters in the model, and they are a little further removed from the outgoing particles. Despite this, the Webber model does an adequate job of fitting the data. It is low for protons, and high for Ξ^-. It does better than either of the other two models at predicting the Ω^- rate.

7.2 Charmed Baryons

This work is the first observation of charmed baryon production at PEP/PETRA energies. It is also only the second observation of semileptonic Λ_c^+ decay. Since Λ_c^+ decays are so poorly measured experimentally, it is difficult to relate these results to a comprehensive theoretical framework. However, as discussed in the previous chapter, this work does hint that the branching ratios for Λ_c^+ semileptonic decay are somewhat larger than the previous SPEAR measurement and bubble chamber upper limit.

Because of the unknown branching ratios, it is difficult to test the various Monte Carlo models. However, the UCLA model predicts a very low rate of Λ_c

production, which leads to implausibly high semileptonic branching ratios. This may indicate that mass based suppression breaks down when one considers leading particle formation.

7.3 Future Work

There is much more that could be done in the areas discussed here. Most of these analyses would benefit from a larger data set; none of the studies described here are anywhere close to systematics limited. With ten times the data, all of the numbers given here could be measured much more accurately. More importantly, several new questions could be addressed. Strange baryon correlations could be studied. Correlation studies with baryons with differing strangeness is the only way to really measure the amount of 'popcorn' present.

The Λ_c^+ study would also benefit from much more data. If a reasonable Λ_c^+ sample could be accumulated, some of the problems associated with an uncertain final state could be reduced by studying some of the reconstructed mass and momentum distributions.

With more data, the search could be extended to look for Ξ_c and Ω_c semileptonic decays. The signal-to-noise ratio for these studies should make them feasible; the problem is that the signal is so small.

The search for exclusive semileptonic decays does not need to be limited to baryons. A look at associated K_s lepton pairs, perhaps with a pion to make a K^*, could signal semileptonic D decays, and semileptonic F decays might be visible via a decay to a ϕ plus a lepton.

7.4 Recapitulation

We have measured the production rates of Ξ^- and Ω^- in 29 GeV e^+e^- annihilation, and found an upper limit to Ξ^{*0} production. We measure 0.017 $\pm$ 0.004 $\pm$ 0.004 Ξ^- per hadronic event, 0.014 $\pm$ 0.006 $\pm$ 0.004 Ω^- per hadronic event, and less than 0.006 Ξ^{*0} per hadronic event, at a 90% confidence level.

We have also observed semileptonic Λ_c^+ decays in 29 GeV e^+e^- annihilation. We find $\sigma(e^+e^- \rightarrow \Lambda_c X) * Br(\Lambda_c \rightarrow e\Lambda X) = 0.0031 \pm 0.0012 \pm 0.0010$ per hadronic event, and $\sigma(e^+e^- \rightarrow \Lambda_c X) * Br(\Lambda_c \rightarrow \mu\Lambda X) = 0.0024 \pm 0.0024 \pm 0.0007$ per hadronic event. When combined with the Lund model predictions for Λ_c^+ production, this leads to semileptonic branching ratios of about 5%. With the Webber model, the predicted branching ratios are about 10%, and with the UCLA models, the branching ratios are about 15%. The last figure is somewhat higher than theoretical predictions and other experimental results.

These results demonstrate the power of two experimental techniques: separated vertices and lepton tagging. Both are powerful methods for particle identification, and both allow small signals to be separated from large backgrounds. By selecting separated vertices, small Ξ^- and Ω^- were separated from a huge random background contained in 100,000 hadronic events.

Lepton tagging is also very powerful. High momentum leptons are a good signal for heavy quark jets. By combining a lepton tag and a Λ tag, we obtain a clean sample of charmed baryons.

REFERENCES

1. For a good introduction to the standard model, see, for example, F. Halzen and A. Martin, *Quarks and Leptons: An Introductory Course in Modern Particle Physics*, John Wiley and Sons, 1984, or E. Leader and E. Predazzi, *An Introduction to Gauge Theories and the 'New Physics',* Cambridge University Press, 1982.

2. The top quark, needed to complete the third generation is still undiscovered, as is the τ neutrino.

3. The masses listed here are those used in the Webber Monte Carlo.

4. However, everything we know indicates that it must exist.

5. Although there has been some evidence for free quarks (see G. S. LaRue, J. D. Phillips, and W. M. Fairbank, Phys. Rev. Lett. **46**, 967 (1981) and references therein), it has not been confirmed by later work. See P. F. Smith *et al.*, Phys. Lett. **B181**, 407 (1986) for some more recent results.

6. S. Weinberg, Phys. Rev. Lett. **19**, 1264 (1967); A. Salaam, in *Elementary Particle Theory*, edited by N. Svartholm, Almqvist and Wiksell, Stockholm, 1978.

7. J. E. Augustin *et al.*, Phys. Rev. Lett. **33**, 1406 (1974). This discovery was simultaneous with its discovery by J. J. Aubert *et al.*, [Phys. Rev. Lett. **33**, 1404 (1974)] in a fixed target experiment.

8. G. Goldhaber *et al.*, Phys. Rev. Lett. **37**, 255 (1976).

9. M. L. Perl *et al.*, Phys. Rev. Lett. **35**, 1489 (1975); M. L. Perl *et al.*, Phys. Lett. **63B**, 466 (1976).

10. Neglecting (generally small) threshold factors.

11. This figure is redrawn from J. W. Gary, Ph.D. thesis, Lawrence Berkeley Laboratory Report LBL-20638, November 1985.

12. R. D. Field and R. P. Feynman, Nucl. Phys. **B136**, 1 (1978).

13. From very early e^+e^- hadronization data.

14. Heavy mesons are those containing a charmed, bottom, or top quark.

15. C. Petersen *et al.*, Phys. Rev. **D27**, 105 (1983).

16. T. Sjöstrand, private communication.

17. A multi-parameter fit has been done by H. Aihara *et al.*, preprint UCLA-85-0515.

18. For a good review of this, and other e^+e^- hadronization experimental results, see D. H. Saxon, Rutherford Appleton Laboratory preprint RAL-86-057, July 1986.

19. P. Hoyer *et al.*, Nucl. Phys. **B161**, 349 (1979).

20. A. Ali *et al.*, Phys. Lett. **93B**, 155 (1980).

21. G. Altarelli and G. Parisi, Nucl. Phys. **B126**, 298 (1977).

22. X. Artru and G. Mennessier, Nucl. Phys. **B70**, 93 (1974).

23. B. Andersson, G. Gustafson, and C. Peterson, Z. Phys. **C1**, 105 (1979). For a newer, general overview of the Lund model, see B. Andersson *et al.*, Phys. Rep. **97**, 33 (1983).

24. B. Andersson *et al.*, Z. Phys. **C20**, 317 (1983).

25. A. Petersen *et al.*, Phys. Rev. **D37**, 1 (1988).

26. S. Behrends *et al.*, Phys. Rev. **D31**, 2161 (1985).

27. B. R. Webber, Nucl. Phys. **B238**, 1 (1984); G. Marchesini and B. R. Webber, Nucl. Phys. **B238**, 492 (1984).

28. C. D. Buchanan and S. B. Chun, Phys. Rev. Lett. **59**, 1997 (1987).

29. T. F. Hoang and B. Cork, preprint LBL-23910, August 1987.

30. M. Gell-Mann, Phys. Lett. **8**, 214 (1963).

31. M. Ida and K. Kobayashi, Prog. Theor. Phys. **36**, 846 (1966).

32. D. B. Lichtenberg and L. J. Tassie, Phys. Rev. **155**, 1601 (1967).

33. L. F. Abbot *et al.*, Phys. Lett. **88B**, 157 (1979).

34. D. B. Lichtenberg, *Unitary Symmetry and Elementary Particles, 2nd Edition*, Academic Press, 1978, p. 251.

35. S. Ekelin, S. Fredriksson, M. Jändel, and T. Larsson, Phys. Rev. **D28**, 257 (1983).

36. A. Casher, H. Neuberger, and S. Nussinov, Phys. Rev. **D20**, 179 (1979).

37. T. Meyer, Z. Phys. **C12**, 77 (1982).

38. B. Andersson *et al.*, Nucl. Phys. **B197**, 45 (1982).

39. B. Andersson, G. Gustafson, and T. Sjöstrand, Physica Scripta **32**, 574 (1985).

40. There are numerous articles on PEP. For an early description of the ring design; see J. Rees *et al.*, in Particle Accelerator Conference, Chicago, 1977, p. 1836.

41. M. Alam *et al.*, SLAC-Proposal-PEP-005, December 1976.

42. W. Davies-White *et al.*, Nucl. Instr. and Meth. **160**, 227 (1979).

43. J. A. Jaros, in *Proceedings of the International Conference on Instrumentation for Colliding Beam Physics*, SLAC Report-250, edited by W. Ash, 1982.

44. R. Ong, Ph.D. thesis, SLAC-Report-320, September 1987.

45. R. Ong, internal Mark II memorandum of January 2, 1986.

46. G. S. Abrams *et al.*, IEEE Trans. Nucl. Sci. **27**, 59 (1980), G. S. Abrams *et al.*, IEEE Trans. Nucl. Sci. **25**, 309 (1978).

47. V. Lüth, internal Mark II memorandum of May 18, 1979.

48. J. D. Fox and M. E. B. Franklin, SLAC-PUB-2691, February 1981.

49. H. Brafman *et al.*, IEEE Trans. Nucl. Sci. **NS-25**, 692 (1978).

50. D. J. Nelson *et al.*, IEEE Trans. Nucl. Sci. **NS-28**, 336 (1981).

51. M. Breidenbach *et al.*, IEEE Trans. Nucl. Sci. **NS-25**, 7C3 (1978).

52. R. H. Schindler, Ph.D. thesis, SLAC-Report-219, May 1979.

53. M. E. Nelson, Ph.D. thesis, Lawrence Berkeley Laboratory Report LBL-16724, October 1983.

54. Recently, some generalized detector simulation packages have become available.

55. T. Sjöstrand, Preprint LU TP 85/10, University of Lund, October 1985.

56. I am grateful to Paul Dauncey for clarifying these points.

57. R. L. Ford and W. R. Nelson, SLAC-Report 210, June 1978.

58. T. W. Arniston, in *Proceedings of the 2nd International School of Radiation Damage and Protection: Computer Techniques in Radiation Transport and Dosimetry*, edited by W. R. Nelson and T. M. Jenkins, Plenum Press, 1980.

59. Nigel Lockeyer, internal Mark II memorandum of June 21, 1984.

60. D. Karlen, internal Mark II memorandum of October 13, 1987.

61. C. de la Vaissiere *et al.*, Phys. Rev. Lett. **54**, 2071 (1985).

62. M. Althoff *et al.*, Phys. Lett. **130B**, 340 (1983).

63. S. Abachi *et al.*, Phys. Rev. Lett. **58**, 2627 (1987).

64. Drew Baden, personal communication.

65. H. M. Schellman, Ph.D. thesis, Lawrence Berkeley Laboratory Report LBL-18699, November 1984; H. Schellman, TG Technical Note 247, August 30, 1983.

66. P. C. Rowson, Ph.D. Thesis, Lawrence Berkeley Laboratory report LBL-20463, October 1985.

67. H. Yamamoto in *QCD and Beyond: Proceedings of the Hadronic Session of the Twentieth Rencontre de Moriond*, edited by J. Tran Thanh Van, Editions Frontieres, France, 1985.

68. M. Dittmar, Ph.D. Thesis, print DESY F1-85-01, April 1985.

69. R. W. Thompson *et al.*, Phys. Rev. **90**, 329 (1953).

70. Some Monte Carlo branching ratios and parameters were changed to save computer time.

71. H. Albrecht *et al.*, in *Proceedings of the XXIIIrd International Conference on High Energy Physics*, ed. S. Loken, World Scientific, 1987.

72. Many groups have searched for charmed baryons; this thesis represents the first positive results.

73. The thrust axis was determined by a subroutine in the package VECSUB, developed by Alfred Petersen.

74. While the latter are real muons, previous Mark II analyses[53] treated all leptons from sources other than heavy quark decays as background. This analysis will continue this practice.

75. M. S. Alam *et al.*, Phys. Rev. Lett. **59**, 22 (1987).

76. K. Riles and J. Dorfan, internal Mark II/PEP5 memorandum of October 21, 1986.

77. R. Morrison, in *Proceedings of the XXIIIrd Moriond Conference Session on Hadronic Interactions, March 13–19, 1988*, to be published.

78. E. N. Vella *et al.*, Phys. Rev. Lett. **48**, 1515 (1982).

79. H. C. Ballagh *et al.*, Phys. Rev. **D24**, 7 (1981).

80. A. Garcia *et al.*, Phys. Rev. Lett. **59**, 864 (1987).

81. This estimate is a weighted mean of the 1986 Particle Data Group average (Phys. Lett. **170B**, p. 17) and a recent high statistics ARGUS measurement taken from H. J. Seeward, Ph.D. Dissertation, print RX-1192, University of Toronto, 1987.

82. G. Abrams *et al.*, Phys. Rev. Lett. **44**, 10 (1980).

83. S. Klein, internal Mark II memorandum of May 8, 1987.

84. H. Aihara *et al.*, Phys. Rev. Lett. **52**, 577 (1984).

85. M. Althoff *et al.*, Z. Phys. **26**, 181 (1984).